

# THE EVOLUTION OF THE STELLAR MASS FUNCTION OF GALAXIES FROM $z = 4.0$ AND THE FIRST COMPREHENSIVE ANALYSIS OF ITS UNCERTAINTIES: EVIDENCE FOR MASS-DEPENDENT EVOLUTION<sup>1</sup>

DANILO MARCHESINI<sup>2</sup>, PIETER G. VAN DOKKUM<sup>2</sup>, NATASCHA M. FÖRSTER SCHREIBER<sup>3</sup>, MARIJN FRANX<sup>4</sup>, IVO LABBÉ<sup>5,6</sup>,  
STIJN WUYTS<sup>7,8</sup>

*Accepted by the Astrophysical Journal*

## ABSTRACT

We present the evolution of the stellar mass function (SMF) of galaxies from  $z = 4.0$  to  $z = 1.3$  measured from a sample constructed from the deep NIR MUSYC, the FIRES, and the GOODS-CDFS surveys, all having very high-quality optical to mid-infrared data. This sample, unique in that it combines data from surveys with a large range of depths and areas in a self-consistent way, allowed us to 1) minimize the uncertainty due to cosmic variance and empirically quantify its contribution to the total error budget; 2) simultaneously probe the high-mass end and the low-mass end (down to  $\sim 0.05$  times the characteristic stellar mass) of the SMF with good statistics; and 3) empirically derive the redshift-dependent completeness limits in stellar mass. We provide, for the first time, a comprehensive analysis of random and systematic uncertainties affecting the derived SMFs, including the effect of metallicity, extinction law, stellar population synthesis model, and initial mass function. We find that the mass density evolves by a factor of  $17^{+7}_{-10}$  since  $z = 4.0$ , mostly driven by a change in the normalization<sup>2</sup>. If only random errors are taken into account, we find evidence for mass-dependent evolution, with the low-mass end evolving more rapidly than the high-mass end. However, we show that this result is no longer robust when systematic uncertainties due to the SED-modeling assumptions are taken into account. Another significant uncertainty is the contribution to the overall stellar mass density of galaxies below our mass limit; future studies with WFC3 will provide better constraints on the SMF at masses below  $10^{10} M_{\odot}$  at  $z > 2$ . Taking our results at face value, we find that they are in conflict with semi-analytic models of galaxy formation. The models predict SMFs that are in general too steep, with too many low-mass galaxies and too few high-mass galaxies. The discrepancy at the high-mass end is susceptible to uncertainties in the models and the data, but the discrepancy at the low-mass end may be more difficult to explain.

*Subject headings:* galaxies: distances and redshifts — galaxies: evolution — galaxies: formation — galaxies: fundamental parameters — galaxies: high-redshift — galaxies: luminosity function, mass function — galaxies: stellar content — infrared: galaxies

## 1. INTRODUCTION

Understanding the formation mechanisms and evolution with cosmic time of galaxies is one of the major goals of observational cosmology. In the current picture of structure formation, dark matter halos build up in a hierarchical fashion through the dissipationless mechanism of gravitational instability controlled by the nature of the dark matter, the power spectrum of density fluctuations, and the parameters of the cosmological model. The assembly of the stellar content of

galaxies is governed by much more complicated physics, such as the mechanisms of star formation, gaseous dissipation, the feedback of stellar and central super-massive black hole energetic output on the baryonic material of the galaxies, and mergers (see Baugh 2006, and references therein for a primer on hierarchical galaxy formation).

A powerful approach to understand these physical processes (including their relative importance as function of cosmic time) is to directly witness the growth of the stellar content in galaxies. Galaxies can grow their stellar mass both from in-situ star formation and/or merger events. Determining the growth of their stellar content as a function of both redshift and stellar mass provides insights into the physical processes governing the assembly and the evolution of galaxies. The stellar mass function (SMF) of galaxies and its evolution with cosmic time represents therefore a powerful tool to directly measure the build-up of the stellar mass content of galaxies.

In the past decade, significant observational progress has been made in the measurement of the SMF of galaxies and its evolution with redshift. Locally, the SMF has been measured from the 2dF Galaxy Redshift Survey (Cole et al. 2001) and the Sloan Digital Sky Survey (SDSS; Bell et al. 2003), providing the  $z = 0$  benchmark. At intermediate redshifts ( $z \sim 1.4$ ), the SMF has also been measured to a satisfactory degree from the VIMOS VLT Deep Survey (VVDS; Pozzetti et al. 2007; Vergani et al. 2008), the DEEP-2 Galaxy Redshift Survey (Bundy et al. 2006), and the COMBO-17 survey (Borch et al. 2006). The SMF appears to evolve slowly at

<sup>1</sup> Based on observations with the *Spitzer Space Telescope*, which is operated by the Jet Propulsion Laboratory (JPL), California Institute of Technology under NASA contract 1407. Based on observations with the NASA/ESA *Hubble Space Telescope*, obtained at the Space Telescope Science Institute, which is operated by AURA, Inc., under NASA contract NAS5-26555. Based on observations collected at the European Southern Observatories, Chile (ESO Programme LP164.O-0612, 168.A-0485, 170.A-0788, 074.A-0709, 275.A-5060, and 171.A-3045). Based on observations obtained at the Cerro Tololo Inter-American Observatory, a division of the National Optical Astronomy Observatories, which is operated by the Association of Universities for Research in Astronomy, Inc. under cooperative agreement with the National Science Foundation.

<sup>2</sup> Department of Astronomy, Yale University, New Haven, CT, PO Box 208101, New Haven, CT 06520, USA

Electronic address: danilom@astro.yale.edu

<sup>3</sup> MPE, Giessenbackstrasse, D-85748, Garching, Germany

<sup>4</sup> Leiden Observatory, Leiden University, P.O. Box 9513, NL-2300 RA Leiden, Netherlands

<sup>5</sup> Carnegie Observatories, 813 Santa Barbara Street, Pasadena, CA 91101

<sup>6</sup> Hubble Fellow

<sup>7</sup> Harvard-Smithsonian Center for Astrophysics, 60 Garden Street, Cambridge, MA 02138

<sup>8</sup> W. M. Keck postdoctoral fellow

$z \sim 1$ , with about half of the total stellar mass density at  $z \sim 0$  already in place at  $z \sim 1$ .

The SMF has also been measured at higher redshifts, up to  $z \sim 5$ , using photometric redshifts derived from multi-waveband imaging surveys (e.g., Dickinson et al. 2003; Fontana et al. 2003; Drory et al. 2004; Fontana et al. 2004; Conselice et al. 2005; Drory et al. 2005; Fontana et al. 2006; Elsner et al. 2008; Pérez-González et al. 2008). The general consensus is that at  $z > 1$  the stellar mass assembly proceeds much more quickly than at lower redshifts. The density of massive galaxies appears to have strongly evolved in the redshift range  $1.5 < z < 3$  (e.g., Fontana et al. 2006), with roughly 40% of the local stellar mass density assembled between  $z = 4$  and  $z = 1$  (e.g., Drory et al. 2005; Pérez-González et al. 2008).

However, at redshift  $z \sim 2$ , the derived SMFs are not in very good agreement (e.g., Elsner et al. 2008), possibly caused by differences in modeling techniques, field-to-field variations, and/or systematic differences in photometric redshift estimate errors. The cause of these differences is difficult to isolate, partly because most existing studies are characterized by either wide but very shallow data (e.g., Drory et al. 2004), or by deep data over relatively small areas (e.g., Dickinson et al. 2003; Fontana et al. 2003; Conselice et al. 2005; Drory et al. 2005; Fontana et al. 2006; Elsner et al. 2008). Therefore, they either only probe the high-mass end of the high- $z$  SMF, or they survey volumes of the universe small enough that cosmic variance constitutes a significant, if not dominant, source of uncertainties. Only the IRAC-selected sample constructed by Pérez-González et al. (2008) provides relatively deep data over three fields for a total of  $\sim 660$  arcmin<sup>2</sup>. Furthermore, a comprehensive analysis of the errors affecting the derived SMFs at high redshift is still missing in the literature. Often, only Poisson errors are considered. Uncertainties from photometric redshift errors are seldomly included, and cosmic variance is never included (which, as we will show, is a very large, if not dominant, component of random errors even with relatively large surveyed area of  $\sim 600$  arcmin<sup>2</sup>). Perhaps even more important is the missing analysis of systematic uncertainties in the derived SMF caused by the assumptions in the SED modeling to estimate the stellar masses. For example, a satisfactory agreement between different stellar population synthesis models has yet to be achieved, and there is evidence for evolution with redshift of some of the relevant parameters, such as the IMF (e.g., Davé 2008; van Dokkum 2008; Wilkins et al. 2008).

In this paper we take advantage of the very high-quality data from the optical to the mid-infrared (MIR) available over the deep NIR MUSYC, the GOODS-CDFS, and the FIRES surveys to measure the evolution of the SMF of galaxies from  $z = 4.0$  to  $z = 1.3$  and to provide the first comprehensive analysis of its random and systematics uncertainties. The composite  $K$ -selected sample, constructed from a total surveyed area of  $\sim 600$  arcmin<sup>2</sup> and probing as deep as  $K_s^{\text{tot}}(5\sigma) = 25.6$ , is unique in that it combines data from surveys with a large range of depths and areas in a self-consistent way. Crucially, the data handling, creation of catalogs, and determination of photometric redshifts and masses were all done with the same methods and techniques. The composite sample therefore self-consistently combines the advantages of deep, pencil beam surveys with those of shallow, wide surveys, allowing us to: 1) minimize the uncertainties due to cosmic variance, and empirically quantify its contribution to the total error budget by exploiting the large number of independent field of views; 2) simultaneously probe the high-mass end and the low-mass

end of the SMF with good statistics; and 3) empirically derive the redshift-dependent completeness limits by exploiting the different depths of the three surveys.

This paper is structured as follows. In § 2 we present the composite  $K$ -selected sample used to measure the SMF of galaxies at  $1.3 < z < 4.0$ ; in § 3 we describe the approach adopted to estimate stellar masses and the default set of SED-modeling assumptions. The methods used to derive the SMF (the  $1/V_{\text{max}}$  and the maximum-likelihood methods) and the approach used to estimate the completeness limits in stellar mass are presented in § 4, as well as the SMFs of galaxies at  $1.3 < z < 2.0$ ,  $2.0 < z < 3.0$ , and  $3.0 < z < 4.0$ . A detailed and comprehensive analysis of the random and systematic uncertainties of the derived SMFs is presented in § 5, while the evolution of the stellar mass densities is presented in § 6. A comparison with the predictions from the latest generation of galaxy formation models is presented in § 7. Our results are summarized in § 8. We assume  $\Omega_M = 0.3$ ,  $\Omega_b = 0.07$ , and  $H_0 = 70$  km s<sup>-1</sup> Mpc<sup>-1</sup> throughout the paper. All magnitudes are on the AB system.

## 2. THE $K$ -SELECTED SAMPLE

### 2.1. Data

The data set we have used to estimate the SMF consists of a composite  $K$ -selected sample of galaxies built from three deep multi-wavelength surveys, all having very high-quality optical to mid-IR photometry: the “ultra-deep” Faint InfraRed Extragalactic Survey (FIRES; Franx et al. 2003), the Great Observatories Origins Deep Survey (GOODS; Giavalisco et al. 2004; Chandra Deep Field South [CDFS]), and the Multi-wavelength Survey by Yale-Chile (MUSYC; Gawiser et al. 2006). Photometric catalogs were created for all fields in the same way, following the procedures of Labbé et al. (2003).

#### 2.1.1. MUSYC

The deep NIR MUSYC survey consists of four  $10^0 - 10^0$  fields, namely, Hubble Deep Field-South 1 and 2 (HDFS-1, HDFS-2, hereafter), the SDSS-1030 field, and the CW-1255 field, observed with the ISPI camera at the Cerro Tololo Inter-American Observatory (CTIO) Blanco 4 m telescope, for a total surveyed area of  $\sim 430$  arcmin<sup>2</sup> ( $\sim 416$  arcmin<sup>2</sup> not overlapping). A complete description of the deep NIR MUSYC observations, reduction procedures, and the construction of the  $K$ -selected catalog with  $U$ -to- $K$  photometry is presented in Quadri et al. (2007).

We added deep *Spitzer*-IRAC 3.6-8.0  $\mu$ m imaging to the NIR MUSYC survey. The IRAC data over the HDFS-1 are part of the GTO-214 program (P.I.: Fazio), while the IRAC data over the other three fields come from the GO-30873 program (P.I.: Labbé). The average total limiting magnitudes of the IRAC images are 24.5, 24.2, 22.4, and 22.3 (3 $\sigma$ , AB magnitude) in the 3.6, 4.5, 5.8, and 8.0  $\mu$ m bands, respectively.<sup>9</sup> The IRAC data, reduction, and photometry are described in detail in Appendix A.

The  $K$ -selected catalogs with IRAC photometry included is publicly available at <http://www.astro.yale.edu/musyc>. The SDSS-1030, CW-1255, HDFS-1, and HDFS-2 catalogs are  $K_s$  band-limited multicolor source catalogs down to  $K_s^{\text{tot}} = 23.6, 23.4, 23.7$ , and  $23.2$ , for a total of 3273, 2445, 2996, and 2118

<sup>9</sup> For the MUSYC survey, less than 4% of the  $K$ -selected sources have IRAC  $S=N < 3$  in the 3.6  $\mu$ m band; for the FIRES and FIREWORKS samples, which are significantly deeper than the MUSYC sample,  $\sim 8\%$  of the galaxies have IRAC  $S=N < 3$ .

sources, over fields of 109, 105, 109, 106 arcmin<sup>2</sup>, respectively. All four fields were exposed in 14 different bands, *U*, *B*, *V*, *R*, *I*, *z*, *J*, *H*, *K*, and the four IRAC channels. The SDSS-1030, CW-1255, HDFS-1, and HDFS-2 *K*-selected catalogs have 90% completeness levels at  $K_S^{\text{tot}} = 23.2$ , 22.8, 23.0 and 22.7, respectively. The final catalogs used in the construction of the composite sample have 2825, 2197, 2266, and 1749 objects brighter than the 90% completeness in the *K*<sub>S</sub> band, over an effective area of 98.2, 91.0, 97.6, and 85.9 arcmin<sup>2</sup>, respectively, for a total of 9037 sources over 372.7 arcmin<sup>2</sup>.

### 2.1.2. FIRES

FIRES consists of two fields, namely, the Hubble Deep Field-South proper (HDF-S) and the field around MS 1054-03, a foreground cluster at  $z = 0.83$ . A complete description of the FIRES observations, reduction procedures, and the construction of photometric catalogs is presented in detail in Labbé et al. (2003) and Förster Schreiber et al. (2006) for HDF-S and MS 1054-03 (hereafter HDFS and MS-1054, respectively). Both *K*<sub>S</sub>-selected catalogs were later augmented with *Spitzer*-IRAC data (Wuyts et al. 2007; Toft et al. 2007). The HDFS catalog has 833 sources down to  $K_S^{\text{tot}} = 26.0$  over an area of  $2.5^\circ \times 2.5^\circ$ . The MS-1054 catalog has 1858 sources down to  $K_S^{\text{tot}} = 25.0$  over an area of  $5.5^\circ \times 5.3^\circ$ . The HDFS field was exposed in the WFPC2 *U*<sub>300</sub>, *B*<sub>450</sub>, *V*<sub>606</sub>, *I*<sub>814</sub> pass-bands, the ISAAC *J*<sub>S</sub>, *H*, and *K*<sub>S</sub> bands, and the four IRAC channels. The MS-1054 *K*<sub>S</sub>-selected catalog comprises FORS1 *U*, *B*, *V*, WFPC2 *V*<sub>606</sub> and *I*<sub>814</sub>, ISAAC *J*, *H*, and *K*<sub>S</sub>, and IRAC 3.6  $\mu$ m - 8.0  $\mu$ m photometry. The HDFS and MS-1054 catalogs have 90% completeness levels at  $K_S^{\text{tot}} = 25.5$  and 24.1, respectively. The final HDFS and MS-1054 catalogs used in the construction of the composite sample have 715 and 1547 objects brighter than the 90% completeness in the *K*<sub>S</sub> band, over an effective area of 4.5 and 21.0 arcmin<sup>2</sup>, respectively.

### 2.1.3. FIREWORKS-CDFS

In this work, we adopted the *K*<sub>S</sub>-selected catalog (dubbed FIREWORKS) of the CDFS field constructed based on the publicly available GOODS-CDFS data by Wuyts et al. (2008). The photometry was performed in an identical way to that of the FIRES fields, and the included passbands are the ACS *B*<sub>435</sub>, *V*<sub>606</sub>, *i*<sub>775</sub>, and *z*<sub>850</sub> bands, the WFI *U*<sub>38</sub>, *B*, *V*, *R*, and *I* bands, the ISAAC *J*, *H*, and *K*<sub>S</sub> bands, and the 4 IRAC channels. The *K*<sub>S</sub>-selected catalog comprises 6308 objects down to  $K_S^{\text{tot}} = 24.6$  over a total surveyed area of 138 arcmin<sup>2</sup>; the variation in exposure time and observing conditions between the different ISAAC pointings lead to an in-homogeneous depth over the whole GOODS-CDFS field (hereafter, CDFS). The final CDFS catalog used in the construction of the composite sample comprises 3559 objects brighter than the 90% completeness level ( $K_S^{\text{tot}} = 23.7$ ), over an effective area of 113 arcmin<sup>2</sup> with coverage in all bands.

### 2.2. Photometric redshifts

The fraction of *K*-selected galaxies with spectroscopic redshifts is 10% (6%) with  $z_{\text{spec}} > 0$  ( $z_{\text{spec}} > 1.3$ ) in the composite *K*-selected sample. Consequently, we must rely primarily on photometric redshift estimates. Photometric redshifts  $z_{\text{phot}}$  for all galaxies were derived using the EAZY photometric redshift code (Brammer et al. 2008). EAZY fits the observed SED of each galaxy with a non-negative linear combination of galaxy templates. The template set used in this

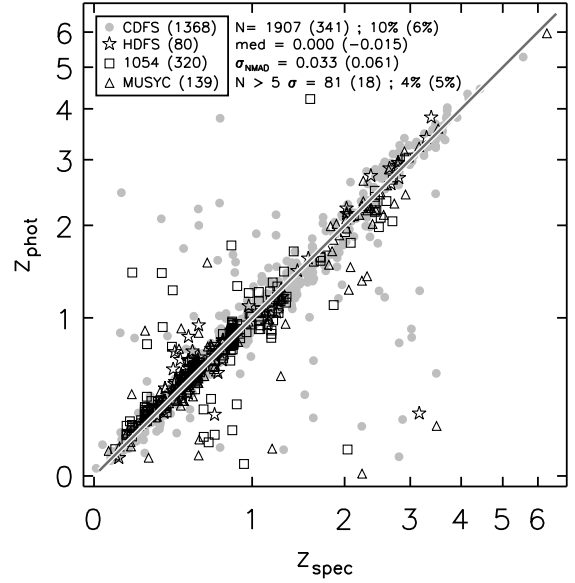


FIG. 1.— Spectroscopic vs. photometric redshifts for the deep NIR MUSYC (open triangles), the CDFS FIREWORKS (gray filled circles), the MS-1054 (open squares) and the HDFS (open stars) FIRES surveys, shown on a “pseudo-log” scale. The total number  $N$  of  $z_{\text{spec}}$ , the median in  $z=(1+z_{\text{spec}})$ , the  $\text{NMAD}$ , and the number of catastrophic outliers is specified (values in parenthesis refer to galaxies with  $z_{\text{spec}} > 1.3$ ). The comparison between  $z_{\text{spec}}$  and  $z_{\text{phot}}$  is extremely good, both at low and at high redshifts.

work is the default EAZY template set *easy\_v1.0*.<sup>10</sup> This template set was constructed from a large number of PÉGAISE models (Fioc & Rocca-Volmerange 1997). It consists of 5 principal component templates that span the colors of galaxies in the semi-analytic model by De Lucia & Blaizot (2007), plus an additional template representing a young (50 Myr) and heavily obscured ( $A_V=2.75$ ) stellar population to account for the existence of dustier galaxies than present in the semi-analytic model. The default template error function (*TEMPLATE\_ERROR.easy\_v1.0*) was applied to down-weight the rest-frame UV and rest-frame NIR during the fitting procedure. The *K*-band magnitude was used as a prior in constructing the redshift probability distribution for each galaxy, and the value  $z_{\text{pm}}$  (the redshift marginalized over the total probability distribution) was adopted as the best estimate of the galaxy redshift.

Figure 1 shows the comparison of  $z_{\text{phot}}$  versus  $z_{\text{spec}}$  for the *K*-selected samples. For the full sample, the median in  $z=(1+z_{\text{spec}})$ , with  $z = z_{\text{phot}} - z_{\text{spec}}$  is 0.000, with the normalized median absolute deviation  $\text{NMAD}^{11} = 0.033$ . The fraction of catastrophic outliers, here defined as galaxies with  $z=(1+z_{\text{spec}}) > 5 \text{ NMAD}$ , is 4%. For galaxies with  $z_{\text{spec}} > 1.3$ , the median in  $z=(1+z_{\text{spec}})$  is -0.015, with  $\text{NMAD} = 0.061$ , and the fraction of catastrophic outliers is 5% (9% if  $\text{NMAD} = 0.033$  corresponding to the entire sample is used in the definition of catastrophic outliers).

Restricting the comparison between  $z_{\text{phot}}$  and  $z_{\text{spec}}$  for the

<sup>10</sup> The template set needs to be large enough that it spans the broad range of multi-band galaxy colors and small enough that the color and redshift degeneracies are kept to a minimum (e.g., Benitez 2000). The default template set used in this work to estimate photometric redshifts was carefully constructed and tested in Brammer et al. (2008). It has been shown to satisfy the requirements for a satisfactory template sets, providing significantly reduced systematic effects and smaller scatter in the  $z_{\text{phot}}$  vs  $z_{\text{spec}}$  at all redshifts.

<sup>11</sup> The normalized median absolute deviation  $\text{NMAD}$ , defined as  $1.48 \text{ median}[|z - \text{median}(z)|] = 1.48 \text{ median}[|z - \text{median}(z)|]$ , is equal to the standard deviation for a Gaussian distribution, and it is less sensitive to outliers than the usual definition of the standard deviation (e.g. Ilbert et al. 2006).

MUSYC sample alone gives similarly good results. We note that the estimate of the photometric redshifts in MUSYC has improved with respect to previously published works, due to the use of EAZY and the inclusion of the IRAC data.

The effects of photometric redshift errors (both random and systematic) on the derived SMFs and stellar mass densities are quantified and discussed in § 5.1. Specifically, the sensitivity of the derived SMFs to the choice of template set is tested in § 5.1.2, and its contribution included in the total error budget.

### 2.3. The composite *K*-selected sample

Stars in all *K*-selected catalogs were identified by spectroscopy, by fitting the object SEDs with stellar templates from Hauschildt, Allard, & Baron (1999) and/or inspecting their morphologies, as in Rudnick et al. (2003). On average, approximately 12% of all objects were classified as stars.

We constructed a composite *K*-selected sample of high-redshift ( $1.3 < z < 4.0$ ) galaxies to be used in the derivation of SMFs of galaxies in § 4. The large surveyed area of the deep NIR MUSYC and FIREWORKS-CDFS surveys allows us to probe the high-mass end of the SMF with good statistics, as well as empirically quantify uncertainties due to field-to-field variations. The very deep FIRES survey is critical in allowing us to constrain the low-mass end of the SMF. Finally, the FIREWORKS-CDFS survey bridges the two slightly overlapping regimes probed by the MUSYC and the FIRES surveys. The final composite sample includes 2014, 830, and 213 *K*-selected galaxies in the three targeted redshift intervals  $1.3 < z < 2.0$ ,  $2.0 < z < 3.0$ , and  $3.0 < z < 4.0$ , respectively, for a total of 3057 galaxies over an effective area of 511.2 arcmin<sup>2</sup> with  $K_S^{\text{tot}} < 25.5$  at  $1.3 < z < 4.0$ . Of these, 6% have spectroscopic redshifts.

### 3. SED MODELING: DEFAULT ASSUMPTIONS

Stellar masses for the HDFS, the MS-1054, and the CDFS fields were derived in Förster Schreiber et al. (in prep.), following the procedure described in Wuyts et al. (2007). We adopted the same procedure to derive the stellar masses of the galaxies in the MUSYC HDFS-1, HDFS-2, SDSS-1030, and CW-1255 fields. In the following we describe our default assumptions, (*BC03*, *Z*, *Kroupa*, *Calzetti*), to perform SED modeling.

We have generated stellar population synthesis models with the evolutionary synthesis code developed by Bruzual & Charlot (2003) (*BC03*). We selected the “Padova 1994” evolutionary tracks (Fagotto et al. 1994), which are preferred by Bruzual & Charlot over the more recent “Padova 2000” tracks because the latter may be less reliable and predict a hotter red giant branch leading to worse agreement with observed galaxy colors. The solar metallicity set of tracks was used. We fitted the *BC03* templates to the observed optical-to-8  $\mu$ m SED with the HYPERZ stellar population fitting code, version 1.1 (Bolzonella et al. 2000). We allowed the following star formation histories: a single stellar population (SSP) without dust, a constant star formation history (CSF) with dust, and an exponentially declining star formation history with an e-folding timescale of 300 Myr ( $\tau_{300}$ ) with dust. The allowed  $A_V$  values ranged from 0 to 4 in step of 0.2 mag, and we used the attenuation law of Calzetti et al. (2000), derived empirically from observations of local UV-bright starburst galaxies under the formalism of a foreground screen of obscuring dust. We constrained the time since the onset of star formation to lie between 50 Myr and the age of the universe at the respective redshift. Finally, we scaled from a Salpeter

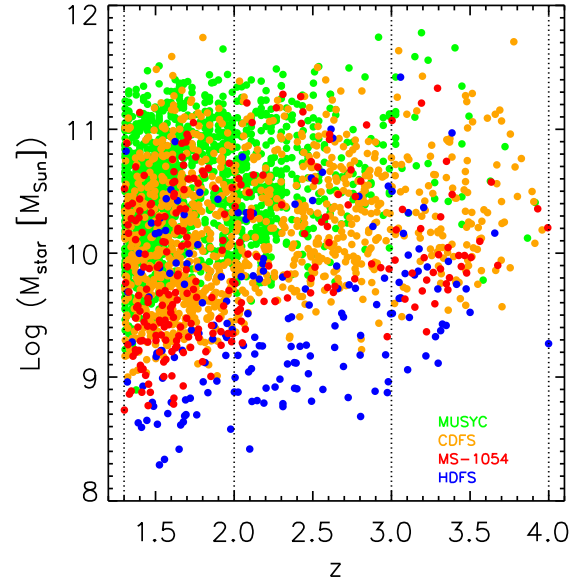


FIG. 2.— Stellar mass versus redshift for FIRES HDFS (red filled circles), FIRES MS-1054 (blue open squares), FIREWORKS CDFS (orange open triangles), and MUSYC (green filled circles).

(1955) IMF with lower and upper mass cutoffs of 0.1  $M_{\odot}$  and 100  $M_{\odot}$  to a pseudo-Kroupa (2001) IMF by dividing the stellar masses by a factor of 1.6. Therefore, the adopted default SED-modeling assumptions can be summarized with the combination (*BC03*, *Z*, *Kroupa*, *Calzetti*), where the first, second, third, and fourth elements are the adopted stellar population synthesis model, the metallicity, the IMF, and the extinction law, respectively. Note that we have used the mass of living stars plus stellar remnants,  $M_{\text{star}}$ , instead of the total mass of stars formed,  $M_{\text{tot}}$ .  $M_{\text{tot}}$  is the integral of the SFR and corresponds to the total gas mass consumed since the onset of star formation, whereas  $M_{\text{star}}$  is computed by subtracting from  $M_{\text{tot}}$  the mass returned to the ISM by evolved stars via stellar winds and supernova explosions (for details see Bruzual & Charlot 2003).

In Figure 2 we show the stellar mass  $M_{\text{star}}$  versus the redshift for the *K*-selected composite sample in the targeted redshift range  $1.3 < z < 4.0$ .

Whereas (*BC03*, *Z*, *Kroupa*, *Calzetti*) represents our default SED-modeling assumptions, we have considered different stellar population synthesis models, metallicities, IMFs, and extinction curves to derive stellar masses. These perturbations on the default set of SED-modeling assumptions are described in detail in § 5.3, together with the resulting systematics effects on the derived SMFs. This has generally not been addressed in previous studies.

One possible limitation of our approach to derive stellar masses in our sample is contamination by obscured AGNs, as they could contribute to the emission in the rest-frame NIR (rest-frame wavelengths longer than 2  $\mu$ m). Several recent studies (e.g., Papovich et al. 2006; Kriek et al. 2007; Daddi et al. 2007) have suggested that the fraction of obscured AGNs increases with redshift and stellar mass. According to Kriek et al. (2007), the fraction is about 20% for massive galaxies at  $2 < z < 2.7$ . To estimate the robustness of our estimated stellar masses in potential obscured AGNs, we have re-estimated the stellar masses of the galaxies with 8  $\mu$ m excess (with respect to the best fit stellar population model) without including the two reddest IRAC channels in the SED-modeling (which probe the rest-frame NIR at  $z > 1.3$ ). The median dif-

ference of the stellar masses estimated with and without the 5.8 and 8.0  $\mu$ m IRAC bands for 8  $\mu$ m excess sources is  $\sim 0\%$ , while the mean difference is  $\sim 6\%$ , negligible with respect to the typical random error ( $\sim 30\%$ ; e.g., Wuyts et al. 2007; Muzzin et al. 2009). We therefore conclude that our stellar mass estimates are robust even for galaxies which likely harbor an AGNs.

#### 4. THE STELLAR MASS FUNCTION

In this section we describe a new technique used to properly quantify the completeness in stellar mass of the  $K$ -selected sample used in the derivation of the SMFs (§ 4.1), and we discuss the two independent methods adopted to derive the SMFs of galaxies, namely an extended version of the  $1=V_{\max}$  method (§ 4.2) and the maximum-likelihood method (§ 4.3).

The uncertainties on the derived SMFs due to photometric redshifts errors, cosmic variance, and different SED-modeling assumptions are quantified and discussed in § 5.1, § 5.2, and § 5.3, respectively.

##### 4.1. Completeness in stellar mass

One of the most critical steps in properly deriving the SMF of galaxies is to understand the completeness in stellar mass as function of redshift of the sample. Determining the completeness for a flux-limited sample is particularly challenging, since there is not a sharp limit in stellar mass corresponding to the sharp limit in flux. This is a direct consequence of the fact that, at any given luminosity, galaxies exhibit a range in mass-to-light ratios ( $M=L$ ). Because of this, galaxies that are not selected because their observed flux is below the detection limit can still have stellar masses well within the range of interest if their  $M=L$  ratios are large enough. For the same reason, galaxies with small stellar masses are observed in even relatively shallow surveys if they have small  $M=L$  ratios.

This is obvious from the left panel of Figure 3, where the stellar mass  $M_{\text{star}}$  is plotted versus the observed  $K$ -band magnitude for the  $K$ -selected galaxies in the narrow redshift range  $1.5 < z < 1.7$  (because of the narrow redshift range, the observed  $K$ -band magnitude is approximately equivalent to the rest-frame luminosity). At a given luminosity, there is a range of stellar masses. The observed range in  $M=L$  ratios at  $1.5 < z < 1.7$  is largest for galaxies with intermediate luminosities and narrower for bright and for faint galaxies. For bright galaxies, the range in  $M=L$  ratio is smaller due to the fact that the bright end of the luminosity function is dominated by red galaxies with generally high  $M=L$  ratios. At the faint end, most galaxies are blue (e.g., Giallongo et al. 2005; Zucca et al. 2006; Marchesini et al. 2007) and have low  $M=L$  ratios, resulting in a narrow range in  $M=L$  ratios. The average  $M=L$  ratio for galaxies in the redshift range  $1.5 < z < 1.7$  at the faint end is a factor of  $\sim 5$  smaller than those at the bright end.

The distribution of galaxies in the left panel of Figure 3 is a function of redshift. First, as higher redshifts are probed, faint galaxies are progressively missed due to the limiting flux of the sample. Consequently, at higher redshifts the sample becomes progressively dominated by galaxies with larger  $M=L$  ratios. Second, the galaxy properties will evolve with redshift, as well as their relative contributions in different luminosity ranges. For example, the bright end of the luminosity function is shown to be dominated by red galaxies at  $z \sim 2.2$ , whereas at  $z \sim 3$  the contribution of red and blue galaxies to the observed number densities appears to be similar (Marchesini et al. 2007). Consequently, the observed range of  $M=L$  ratios at

the bright end would increase going to higher redshifts.

Most of the previous works deriving the SMFs of galaxies (e.g., Drory et al. 2005; Fontana et al. 2006; Pérez-González et al. 2008; see also Appendix C for a detailed discussion of previously published works and their assumed completeness limits in stellar mass) have estimated their completeness in stellar mass based on the maximal stellar mass allowed for a galaxy at the flux limit of the sample. This maximal mass is typically taken to be the stellar mass of a passively evolving population with no dust extinction formed in a single burst at very high ( $z \sim 10$ ) redshift, scaled to match the limiting flux (SSP-derived completeness limit, hereafter). This approach, although easy to implement, is conceptually wrong, and potentially affected by several caveats.

For example, the faint-end of the galaxy luminosity function is dominated by intrinsically blue galaxies (e.g., Zucca et al. 2006; Marchesini et al. 2007), characterized by small  $M=L$  ratios (see also left panel of Figure 3). If an SSP-derived completeness limit (shown by the dashed curves in the right panel of Figure 3) were to be used in deriving the completeness in stellar mass of a deep survey, the sample would be cut at conservatively too high stellar masses. More importantly, the derived number density at the low-mass end would be significantly affected due to miscalculation of  $V_{\max}$  in the  $1=V_{\max}$  method. Another complication is caused by the ubiquitous presence of dust in real galaxies. Dust extinction can reduce the completeness derived from no-extinction SSPs since, to first order, it moves the dashed curves in the right panel of Figure 3 upwards. While at low redshift massive galaxies are usually characterized by passively evolving populations with no or little dust extinction, this does not seem to be the case at high redshifts, where significant amount of extinction ( $A_V \sim 1-2$ ) can be present even in massive galaxies (e.g., Blain et al. 1999b; Muzzin et al. 2009).

In order to avoid these problems, we have used a different approach to estimate the redshift-dependent completeness limit in stellar mass. Our approach exploits the availability of several samples with different depths, and the completeness of a sample is estimated empirically from the available deeper samples. To estimate the redshift-dependent stellar mass completeness limit of one of the considered samples, we first selected galaxies belonging to the available deeper samples. Then, we scaled their fluxes and stellar masses to match the  $K$ -band completeness limit of the sample we want to derive the completeness limit in stellar mass for. The upper envelope of points in the ( $M_{\text{star, scaled}} - z$ ) space, encompassing 95% of the points, represents the most massive galaxies at the considered flux limit, and so provides a redshift-dependent stellar mass completeness limit for the considered sample. This method is illustrated in detail for the SDSS-1030 sample in Appendix B. By repeating this procedure, we derived the redshift-dependent completeness limits in stellar mass for all samples. These limits are shown in the right panel of Figure 3, along with SSP-derived completeness limits.

Interestingly, the empirically-derived completeness limit is similar to the SSP-derived completeness only for the CDFS sample. For shallower samples (e.g., SDSS-1030), the sample is actually less complete than what would be estimated with the SSP-derived completeness over the redshift range  $2.5 < z < 4$ . Conversely, the SSP-derived completeness is too conservative (by  $\sim 0.3$  dex) for deeper samples, such as the FIRES MS-1054 sample.

For the MS-1054 sample, the empirically-derived completeness at  $3.0 < z < 4.0$  is poorly derived due to the small



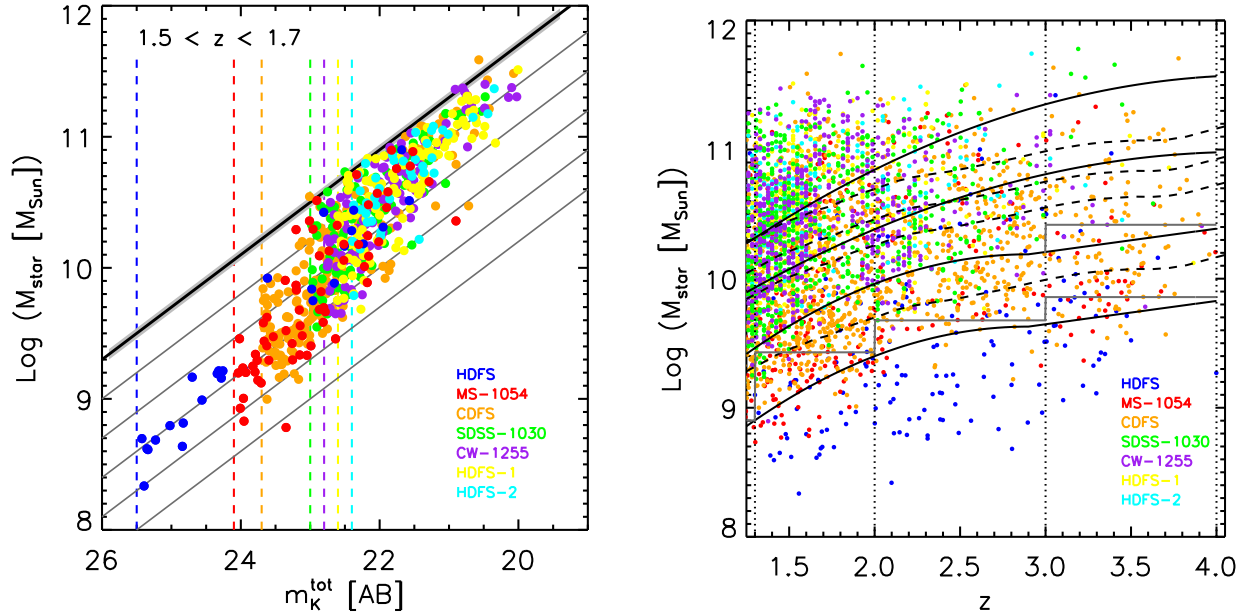


FIG. 3.— *Left panel:* Stellar mass  $M_{\text{star}}$  versus observed total  $K$ -band magnitude for the galaxies at redshift  $1.5 < z < 1.7$  in the  $K$ -selected sample. The thick black line represents the stellar mass of a single stellar population formed at  $z = 10$  and with no dust as a function of the observed  $K$ -band magnitude; the gray shaded region around it represents the scatter due to the width of the considered redshift interval. The gray curves represent  $M=L$  ratios 2, 4, 8, 16, and 32 times smaller than that of the single stellar population formed at  $z = 10$ . The vertical dashed lines represent the  $K$ -band completeness limits, from left to right, of the HDFS, MS-1054, CDFS, SDSS-1030, CW-1255, HDFS-1, and HDFS-2 samples. The largest range in  $M=L$  ratios is observed at intermediate luminosities, while the range in  $M=L$  is much narrower both at bright and faint luminosities. *Right panel:* Empirically-derived completeness limits in stellar mass as a function of redshift for our  $K$ -selected samples (the HDFS-1, HDFS-2, and CW-1255 samples are omitted for clarity), plotted as solid black curves (from top to bottom, SDSS-1030, CDFS, MS-1054, and HDFS). For comparison, the dashed curves represent the SSP-derived completeness limits. The gray solid lines represent the adopted conservative completeness limit at  $3.0 < z < 4.0$  for the MS-1054 sample, and at all redshifts for the HDFS sample to ensure robust derivation of the SMFs. Note the differences, as function of redshift and stellar mass, between the empirically- and SSP-derived completeness limits.

number of galaxies in the HDFS sample in this redshift range. Therefore, we have conservatively assumed its largest value throughout the entire redshift range  $3.0 < z < 4.0$ . For the HDFS sample, there is no deeper survey that can be used to empirically derive its completeness in stellar mass. The completeness of HDFS was therefore estimated by scaling the empirically-derived completeness limit of the MS-1054 sample to match the  $K$ -band 90% completeness flux limit of the HDFS sample, and by taking the largest value of the scaled completeness within each individual redshift interval (shown as gray solid lines in the right panel of Figure 3). Although this is a very conservative approach, it ensures correct determination of the SMF at the low-mass end.

#### 4.2. The $1=V_{\text{max}}$ method

To estimate the observed SMF for our composite sample, we have applied an extended version of the  $1=V_{\text{max}}$  algorithm (Schmidt 1968) as defined in Avni & Bahcall (1980) so that several samples with different depths can be combined in one calculation. This method is described in detail in Marchesini et al. (2007), where it was used to derive the rest-frame optical luminosity functions of galaxies at redshift  $2.0 < z < 3.5$  from a similar  $K$ -selected sample. The empirically-derived redshift-dependent completeness limits in stellar mass as derived in § 4.1 for the individual  $K$ -selected samples was used in the calculation of  $V_{\text{max}}$ . The Poisson error in each stellar mass bin was computed adopting the recipe of Gehrels (1986).

The  $1=V_{\text{max}}$  estimator has the advantages of simplicity and no a priori assumption of a functional form for the stellar mass distribution; it also yields a fully normalized solution. However, it can be affected by the presence of clustering in the sample, leading to a poor estimate of the faint-end slope of the SMF. Field-to-field variation represents a significant source of uncertainty in deep surveys, since they are characterized

by small areas and hence small probed volumes. The contribution due to sample variance to the total error budget is quantified in § 5.2.

#### 4.3. The maximum likelihood method

We also measured the observed SMF using the STY method (Sandage, Tammann & Yahil 1979), which is a parametric maximum-likelihood estimator. The STY method has been shown to be unbiased with respect to density inhomogeneities (e.g., Efstathiou, Ellis & Peterson 1988), it has well-defined asymptotic error properties (e.g. Kendall & Stuart 1961) and does not require to select bin widths.

We have assumed that the number density ( $M$ ) of galaxies is described by a Schechter (1976) function,

$$(M) = (\ln 10)^{-2} 10^{(M-M^?) (1+\alpha)} \exp[-10^{(M-M^?)}] ; \quad (1)$$

where  $M = \log(M_{\text{star}}/M_{\odot})$ ,  $\alpha$  is the low mass-end slope,  $M^? = \log(M_{\text{star}}^?/M_{\odot})$  is the characteristic stellar mass at which the SMF exhibits a rapid change in the slope, and  $?$  is the normalization.

The implementation of the STY method and the method of estimating errors is described in detail in Marchesini et al. (2007). The best-fit solution is obtained by maximizing the likelihood with respect to the parameters  $\alpha$  and  $M^?$ . The value of  $?$  is then obtained by imposing a normalization on the best-fit SMF such that the total number of observed galaxies in the composite sample is reproduced. The 1 and 2 errors on  $?$  are estimated from the minimum and maximum values of  $?$  allowed by the 1 and 2 confidence contours in the  $(-M_{\text{star}}^?)$  parameter space, respectively.

#### 4.4. Stellar Mass Functions

Figure 4 (top panel) shows the SMFs of galaxies at redshift  $1.3 < z < 2.0$ ,  $2.0 < z < 3.0$ , and  $3.0 < z < 4.0$ . Points with

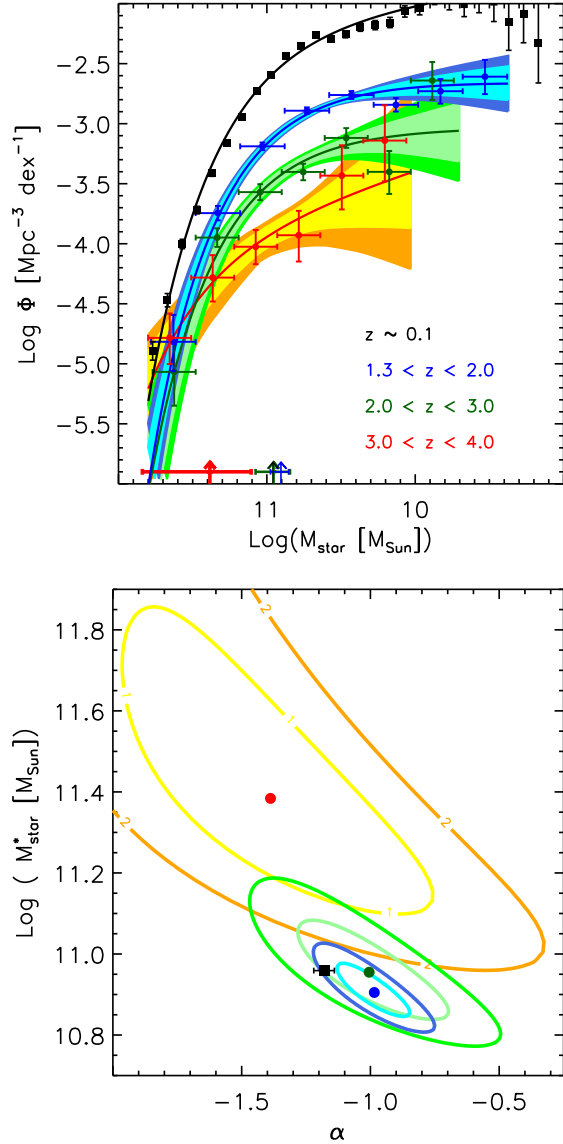


FIG. 4.— *Top panel:* SMFs of galaxies at redshift  $1.3 < z < 2.0$  (blue),  $2.0 < z < 3.0$  (green), and  $3.0 < z < 4.0$  (red). The filled symbols represent the SMFs derived with the  $1=V_{\max}$  method, with error bars including only Poisson errors. The solid curves represent the SMFs derived with the maximum-likelihood analysis, with shaded regions representing the  $1\sigma$  and  $2\sigma$  uncertainties. The arrows show the best estimates of  $M_{\text{star}}^?$  and the corresponding  $1\sigma$  errors derived with the maximum-likelihood analysis. The black solid curve and points represent the local ( $z = 0.1$ ) SMF from Cole et al. (2001). *Bottom panel:* ( $\alpha - M_{\text{star}}^?$ ) parameter space derived from the maximum-likelihood analysis. Filled circles are the best-fit values of  $\alpha$  and  $M_{\text{star}}^?$ , while the curves represent their  $1\sigma$  and  $2\sigma$  contour levels; the colors are the same as in the top panel. The black filled square represent the redshift  $z = 0.1$  value from Cole et al. (2001). Very little evolution of the shape of the SMF is observed from  $z = 3.0$  to  $z = 1.3$ , and most of the evolution is in the characteristic density  $\rho^?$ . The shape of the SMF at  $z = 3.5$  is different, characterized by a much steeper low-mass end slope. The characteristic stellar mass  $M_{\text{star}}^?$  seems to have evolved little, if any, from  $z = 2.5$  to  $z = 0.1$ .

error bars show the SMFs derived using the  $1=V_{\max}$  method. The solid curves show the SMFs derived with the maximum-likelihood analysis, while the shaded regions represent their  $1\sigma$  and  $2\sigma$  uncertainties. The bottom panel of Figure 4 shows the best-fit value and the  $1\sigma$  and  $2\sigma$  confidence contour levels of the two Schechter function parameters  $\alpha$  and  $M_{\text{star}}^?$  in the three targeted redshift intervals. The local SMF derived by Cole et al. (2001) is also shown in Figure 4. The plotted uncertainties include Poisson errors only. The uncertain-

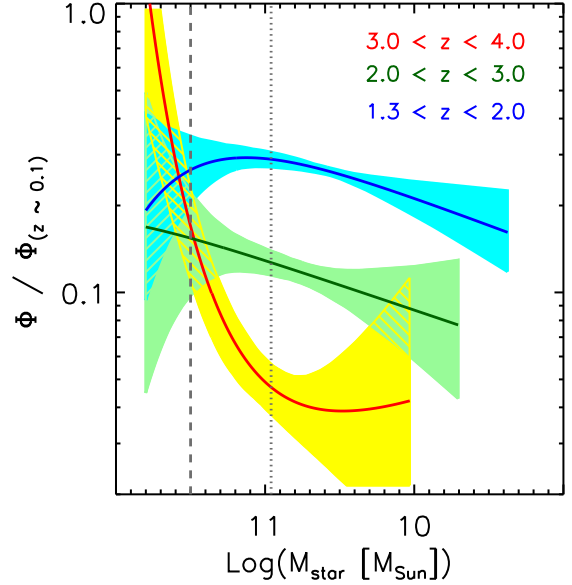


FIG. 5.— Ratio of the high- $z$  SMFs ( $\phi$ ) and the local SMF ( $\phi(z = 0.1)$ ) plotted as function of the stellar mass as measured from the maximum-likelihood analysis. The shaded regions represent the  $1\sigma$  uncertainties. Colors are as in Fig. 4. The vertical dashed and dotted lines represent the value of  $3 \times 10^{11} M_{\odot}$  and the  $z = 0.1$  characteristic stellar mass,  $M_{\text{star}}^? = 10^{11} M_{\odot}$ , respectively. Evidence for mass-dependent evolution is present, with the evolution to  $z = 0.1$  being larger at the low-mass end and smallest for the most massive galaxies.

ties on the derived SMFs due to cosmic variance, photometric redshift errors, and different SED-modeling assumptions are quantified and discussed in § 5.

The large surveyed area allows for the determination of the high-mass end with unprecedented accuracy, while the depth of the FIRES survey allows us to constrain also the low-mass end. This is particularly important because of the well-known correlation between the two parameters  $\alpha$  and  $M_{\text{star}}^?$ .

Figure 4 clearly shows dramatic evolution of the SMF, qualitatively consistent with other studies (e.g., Fontana et al. 2006; Pérez-González et al. 2008). The main trend is a gradual decrease with redshift of the characteristic density  $\rho^?$ , rather than a change in the slope  $\alpha$  or the characteristic stellar mass  $M_{\text{star}}^?$ . The density at  $M_{\text{star}} = 10^{11}$  has evolved by a factor of  $\sim 20$  since  $z = 3.5$ , a factor of  $\sim 8$  since  $z = 2.5$ , and a factor of  $\sim 3.5$  since  $z = 1.65$ . The data points shown in Figure 4, along with the best-fitting Schechter function parameters, are listed in Table 1 and Table 2.

We also find evidence for mass-dependent evolution. In particular, the data suggest a remarkable lack of evolution for the most massive galaxies, with  $M_{\text{star}} > 3 \times 10^{11}$ , over the redshift range  $1.3 < z < 4.0$ . The average density of these galaxies is  $1.3 \times 10^{-5} \text{ Mpc}^{-3}$ . The differential evolution of galaxies with different masses is shown more clearly in Figure 5, where the high-redshift SMFs divided by the local SMF have been plotted as function of stellar mass. If the form of the mass function does not evolve with redshift, the curves in Figure 5 would be constant lines as function of stellar mass. On the contrary, the observed evolution of the number densities is larger for less massive galaxies and smallest for the most massive galaxies.

## 5. UNCERTAINTIES

The results found in the previous sections are very intriguing. However, only Poisson errors have been considered, and, as previously noted, uncertainties due to photometric redshift

TABLE 1  
SMFs DERIVED WITH THE  $1=V_{\max}$  METHOD

$\log M_{\text{star}}$ ( $M_{\odot}$ )	$\log$ ( $\text{Mpc}^{-3} \text{ dex}^{-1}$ )	Poi	$z_{\text{ran}}$	cv	$z_{\text{sys}}$	sed <sub>sys</sub>
<b>1.3 <math>z &lt; 2.0</math>:</b>						
11.63	-4.817	+0.283 -0.300	+0.224 -0.245	0.111	0.132	+0.000 -0.398 +0.699
11.33	-3.745	0.168	0.060	0.029	0.155	+0.068 -0.442 +0.470
11.03	-3.189	0.067	0.032	0.020	0.056	+0.000 -0.083 +0.083
10.73	-2.892	0.110	0.028	0.020	0.105	+0.041 -0.000 +0.052
10.43	-2.761	0.076	0.033	0.024	0.065	+0.108 -0.045 +0.166
10.13	-2.843	0.106	0.056	0.039	0.082	+0.031 -0.068 +0.077
9.83	-2.730	0.245	0.102	0.061	0.214	+0.014 -0.156 +0.189
9.53	-2.608	+0.289 -0.292	+0.140 -0.145	0.135	0.214	+0.050 -0.050 +0.164
<b>2.0 <math>z &lt; 3.0</math>:</b>						
11.63	-5.067	+0.333 -0.356	+0.253 -0.282	0.152	0.156	+0.139 -0.000 +0.139
11.34	-3.949	0.113	0.078	0.059	0.056	+0.001 -0.287 +0.149
11.05	-3.570	0.103	0.067	0.045	0.064	+0.331 -0.068 +0.093
10.76	-3.402	0.118	0.069	0.049	0.083	+0.107 -0.000 +0.107
10.47	-3.119	0.215	0.082	0.070	0.186	+0.000 -0.159 +0.159
10.18	-3.401	+0.291 -0.298	+0.174 -0.184	0.115	0.204	+0.100 -0.125 +0.125
9.89	-2.640	+0.298 -0.302	+0.154 -0.161	0.154	0.204	+0.142 -0.062 +0.142
<b>3.0 <math>z &lt; 4.0</math>:</b>						
11.66	-4.784	+0.446 -0.453	+0.203 -0.219	0.239	0.316	+0.000 -0.526 +0.526
11.37	-4.282	+0.322 -0.329	+0.157 -0.199	0.126	0.229	+0.000 -0.428 +0.428
11.08	-4.025	+0.217 -0.221	+0.140 -0.145	0.095	0.136	+0.146 -0.107 +0.107
10.79	-3.929	+0.424 -0.431	+0.203 -0.219	0.195	0.316	+0.037 -0.000 +0.037
10.50	-3.433	+0.433 -0.470	+0.253 -0.282	0.203	0.316	+0.000 -0.458 +0.458
10.21	-3.141	+0.496 -0.524	+0.294 -0.340	0.244	0.316	+0.125 -0.000 +0.125

$= (\frac{2}{\text{Poi}} + \frac{2}{\text{cv}} + \frac{2}{z_{\text{ran}}})^{1/2}$  is the total 1- $\sigma$  random error, including the Poisson errors ( $\text{Poi}$ ), the errors due to photometric redshift random uncertainties ( $z_{\text{ran}}$ ; see § 5.1), and the error due to cosmic variance ( $\text{cv}$ ; see § 5.2);  $z_{\text{sys}}$  is the systematic uncertainty due to different template sets in the photometric redshift estimate, while  $\text{sed}_{\text{sys}}$  is the systematic uncertainty due to different SED-modeling assumptions (see § 5.1 and 5.3).

TABLE 2  
BEST-FIT SCHECHTER FUNCTION PARAMETERS FOR THE SMFs

Redshift Range	$\log M_{\text{star}}^?$ ( $M_{\odot}$ )	$?$ ( $10^{-4} \text{ Mpc}^{-3} \text{ dex}^{-1}$ )	$z_{\text{sys}}$	sed <sub>sys</sub>	$(\log M_{\text{star}}^?)_{z_{\text{sys}}}$	$(\log M_{\text{star}}^?)_{\text{sed}_{\text{sys}}}$	$?$ $z_{\text{sys}}$	$?$ sed <sub>sys</sub>
$z = 0.1$	-1.18 ± 0.03	10.96 ± 0.01	30.87 ± 4.80					
1.3 $z < 2.0$	-0.99 <sup>+0.13</sup> <sub>-0.23</sub>	10.91 <sup>+0.07</sup> <sub>-0.09</sub>	10.17 <sup>+1.71</sup> <sub>-3.19</sub>	+0.08 -0.10	+0.16 -0.31	+0.05 -0.06	+0.41 -0.17	+0.60 -1.71
2.0 $z < 3.0$	-1.01 <sup>+0.30</sup> <sub>-0.27</sub>	10.96 <sup>+0.12</sup> <sub>-0.11</sub>	3.95 <sup>+1.44</sup> <sub>-2.43</sub>	+0.03 -0.12	+0.16 -0.35	+0.03 -0.01	+0.22 -0.33	+0.85 -1.03
3.0 $z < 4.0$	-1.39 <sup>+0.63</sup> <sub>-0.55</sub>	11.38 <sup>+0.46</sup> <sub>-0.28</sub>	0.53 <sup>+1.32</sup> <sub>-0.45</sub>	+0.30 -0.20	+0.42 -0.53	+0.08 -0.25	+0.25 -0.30	+0.37 -0.16

The quoted errors correspond to the 1 and 2- $\sigma$  errors estimated from the maximum-likelihood analysis as described in § 4.3. Also listed are the systematic uncertainties on the Schechter function parameters due to different SED-modeling assumptions and different template sets in the photometric redshift estimate (see § 5.1 and 5.3). The local ( $z = 0.1$ ) values are taken from Cole et al. (2001).

errors (both random and systematic), cosmic variance, and different SED-modeling assumptions also affect the measurement of the high-redshift SMF.<sup>12</sup> In this section we quantify the uncertainties on the measured SMFs due to these sources of errors, providing the first comprehensive analysis of random and systematic uncertainties affecting the high- $z$  SMFs.

### 5.1. Uncertainties due to photometric redshift errors

Studies of high-redshift galaxies largely rely on photometric redshift estimates. It is therefore important to understand how the photometric redshift uncertainties affect the derived SMFs and densities.

<sup>12</sup> We note that the results from the maximum-likelihood analysis are unbiased with respect to density inhomogeneities, hence not affected by cosmic variance.

#### 5.1.1. Photometric redshift random errors

To quantify the uncertainties on the SMFs due to photometric redshift random errors we have proceeded as follows. First, for each galaxy in the  $K$ -selected sample, a set of 100 mock SEDs was created by perturbing each flux point according to its formal error bar. Second, we estimated photometric redshift  $z_{\text{phot}}$  in the same way as described in § 2.2. Third, we fitted the mock SEDs to estimate stellar masses as described in § 3, using the default set of SED-modeling assumptions. Finally, we have derived completeness limits in stellar mass and SMFs of galaxies with the  $1=V_{\max}$  and the maximum-likelihood analysis for each of the 100 Monte Carlo realizations of the composite  $K$ -selected sample. This approach naturally addresses the fact that fainter sources tend to be characterized by less accurate  $z_{\text{phot}}$  estimates due to the



larger errors in their photometry, as well as sources characterized by power-law SEDs and consequently by very poorly-constrained  $z_{\text{phot}}$  estimates and very broad  $z_{\text{phot}}$  distributions derived from the Monte Carlo realizations. Moreover, the adopted Monte Carlo approach to estimate the uncertainties on the SMF due to the photometric redshift random error is to be preferred to the approach using the comparison of  $z_{\text{phot}}$  with  $z_{\text{spec}}$ , as this comparison is strongly affected by the very biased and incomplete sub-sample of galaxies at  $z \sim 1.5$  with available spectroscopic redshifts (see, e.g., Brammer et al. 2008).

The contribution to the total error budget of the SMFs derived using the  $1=V_{\text{max}}$  method due to photometric redshift random errors ( $\sigma_{z_{\text{ran}}}$ ) was estimated by taking, for each stellar mass bin, the lower and upper errors on  $\log(M)$  comprising the central 68% of the Monte Carlo distribution. The values of  $\sigma_{z_{\text{ran}}}$  for each stellar mass bin in the three targeted redshift intervals are listed in Table 1. The contribution of photometric redshift random uncertainties to the total error budget of the SMFs derived with the  $1=V_{\text{max}}$  method is generally smaller (although non-negligible) than  $\sigma_{\text{Poi}}$  and  $\sigma_{\text{cv}}$  (the error due to cosmic variance; see § 5.2), the latter dominating the random error budget. This is true at all redshifts. The contribution of  $\sigma_{z_{\text{ran}}}$  is largest (although still relatively small) for the largest stellar mass bin ( $M \sim 11 \times 10^{11} M_{\odot}$ ), which is usually populated only by a handful of sources, and for the SMF at redshift  $3.0 < z < 4.0$ .

The uncertainties on the SMFs derived using the maximum-likelihood analysis due to photometric redshift random errors appears to be negligible. This is due to the fact that, when the maximum-likelihood analysis is used to derive the SMFs, the whole stellar mass range contributes to the determination of the Schechter function parameters, significantly reducing the impact of photometric redshift random errors. The derived  $1\sigma$  contour level from the maximum-likelihood analysis contains 95% of the Monte Carlo realizations.<sup>13</sup> Therefore, the errors on the Schechter function parameters due to photometric redshift random errors can be neglected. This is true for all three targeted redshift intervals.

### 5.1.2. Photometric redshift systematic errors

In addition to random errors, systematic errors can be caused by the specific choice of the templates or the template error function used in the estimate of the photometric redshifts. To quantify these systematic errors, we have repeated the  $z_{\text{phot}}$  estimates using the following different combination of template set and template error function: 1) *eazy\_v1.0\_nodust* and *TE.eazy\_v1.0\_nodust*, with *eazy\_v1.0\_nodust* equal to the default set *eazy\_v1.0* without the dusty template, and *TE.eazy\_v1.0\_nodust* the template error function specifically constructed for the *eazy\_v1.0\_nodust* template set; 2) *eazy\_v1.0* and *TE.eazy\_v1.0\_nodust*; 3) *br07\_default* and *TE.eazy\_v1.0*, with *br07\_default* the default template set of Blanton & Roweis (2007). These three combinations were chosen because they resulted in  $z_{\text{phot}} - z_{\text{spec}}$  comparisons of similar quality (or only slightly worse) as that derived in § 2.2 using the default EAZY template set and template error function. We decided not to use the *cww+kin*<sup>14</sup> and the *pegase13*<sup>15</sup> template sets (also distributed with the EAZY

code), due to the significantly worse resulting  $z_{\text{phot}} - z_{\text{spec}}$  comparisons. Modeling of the observed SEDs was then performed using the new sets of  $z_{\text{phot}}$  to derived stellar masses, and the completeness limits in stellar mass were then re-estimated and the SMFs re-derived with both the  $1=V_{\text{max}}$  and the maximum-likelihood methods. The last three columns of Table 4 list the SMFs of galaxies at  $1.3 < z < 2.0$ ,  $2.0 < z < 3.0$ , and  $3.0 < z < 4.0$  derived using the  $1=V_{\text{max}}$  method for each combination of template set and template error function. Table 5 lists the best-fit Schechter function parameters  $\log(M_{\text{star}}^*)$ , and  $\alpha$  of the SMFs of galaxies at  $1.3 < z < 2.0$ ,  $2.0 < z < 3.0$ , and  $3.0 < z < 4.0$  derived using the maximum-likelihood analysis for each combination of template set and template error function.

Systematic errors were then quantified by comparing the resulting SMFs with the SMFs derived using the preferred default EAZY template set and template error function, following the same approach (described in § 5.3) used to quantify the systematic uncertainties due to different SED modeling assumptions. These systematic uncertainties,  $\sigma_{z_{\text{sys}}}$  for the SMFs derived with the  $1=V_{\text{max}}$  method, and  $\sigma_{z_{\text{sys}}}$ ,  $(\log M_{\text{star}}^*)_{z_{\text{sys}}}$ , and  $\alpha_{z_{\text{sys}}}$  for the Schechter function parameters derived with the maximum-likelihood analysis, are listed in Table 1 and 2, respectively. The values of  $\sigma_{z_{\text{sys}}}$  are generally asymmetric and larger than  $\sigma_{z_{\text{ran}}}$ , and larger than the total  $1\sigma$  random error for 1/3 of the considered stellar mass bins. On the contrary, the systematic uncertainties on the Schechter function parameters due to different template sets or template error functions are always smaller than the  $1\sigma$  error estimated from the maximum-likelihood analysis. We note that our results may be influenced by unknown systematic effects in the redshifts, particularly at the high-mass end. Spectroscopic redshifts, or photometric redshifts with very small errors and systematics (e.g., van Dokkum et al. 2009), are needed to confirm the shape of the mass function in the highest mass bins.

### 5.2. Uncertainties due to cosmic variance

As already pointed out, cosmic variance represents a significant source of uncertainty in deep surveys, since they are characterized by small areas and hence small probed volumes. Our composite sample is made of several independent fields with a large total effective area of  $\sim 511 \text{ arcmin}^2$ , which significantly reduces the uncertainties due to cosmic variance. Also, the large number of fields considered in this work with their large individual areas allows us to empirically quantify the field-to-field variations from one field to the other in the estimate of the SMF with the  $1=V_{\text{max}}$  method, especially at the high-mass end, and to properly account for it in the error budget.

In order to quantify the uncertainties due to field-to-field variations in the determination of the SMF, we proceeded as in Marchesini et al. (2007). Briefly, using the  $1=V_{\text{max}}$  method, we measured  $\bar{j}$ , where  $j$  is the galaxy number density in the stellar mass bin  $M$  for the  $j$ th field. For each stellar mass bin with  $n > 3$ , we estimated the contribution to the error budget

<sup>13</sup> These results are fully consistent with the Monte Carlo simulations performed in Marchesini et al. (2007) to address the systematic uncertainties on the Schechter function parameters of the high-redshift rest-frame optical luminosity functions due to photometric redshift random uncertainties.

<sup>14</sup> The *cww+kin* template set comprises the empirical templates from Coleman, Wu, & Weedman (1980) plus the “SB1” starburst spectrum from Kin-

ney et al. (1996); these templates have been extended in the UV and IR by Arnouts et al. (1999) ([http://www.oamp.fr/people/arnouts/LE\\_PHASE.html](http://www.oamp.fr/people/arnouts/LE_PHASE.html))

<sup>15</sup> The *pegase13* template set contains the set of constant star formation rate models with additional dust reddening applied using the extinction curve of Calzetti et al. (2000) (see Brammer et al. 2008 for details).

of from cosmic variance using:

$$\sigma_{cv} = \frac{rms(\sigma)}{\sqrt{n}}; \quad (2)$$

with  $n$  the number of individual fields used. For the stellar mass bins with  $n \leq 2$ , we adopted the mean of the  $rms(\sigma)$  with  $n > 3$ . The final 1- $\sigma$  random error associated to  $\langle M \rangle$  is then  $\sigma = (\sigma_{Poi}^2 + \sigma_{cv}^2 + \sigma_{z,ran}^2)^{1/2}$ , with  $\sigma_{Poi}$  the Poisson error in each magnitude bin, and  $\sigma_{z,ran}$  the error due to photometric redshift random uncertainties as derived in § 5.1.<sup>16</sup>

The values of  $\sigma_{cv}$  for each stellar mass bin in the three targeted redshift intervals are listed in Table 1. In the redshift range  $1.3 < z < 2.0$ , cosmic variance is the dominant source of random errors over almost the entire probed stellar mass range, with the exception of the most massive bin which is populated only by a handful of sources. At  $z \sim 2.0$ , cosmic variance is generally comparable, or slightly smaller than, Poisson errors, due to the larger probed volumes and to the smaller number of galaxies with respect to the  $1.3 < z < 2.0$  redshift interval. We stress that the results from the maximum-likelihood analysis are not affected by cosmic variance, since the adopted STY method is unbiased with respect to density inhomogeneities (e.g. Efstathiou, Ellis & Peterson 1988).

### 5.3. Systematic effects due to different SED modeling assumptions

As described in § 3, the default set of SED-modeling assumptions is represented by (BC03,  $Z_{\odot}$ , Kroupa, Calzetti), i.e. BC03 stellar population synthesis models with a pseudo-Kroupa (2001) IMF and solar metallicity have been used in combination with the Calzetti et al. (2000) extinction law to derived stellar masses. With broad-band photometry alone, it is not possible to constrain the metallicity, the IMF, the extinction law, or the stellar population synthesis model. Even with high-quality optical-to-MIR photometry and NIR spectroscopy, it is not possible to statistically constrain any of the above, as shown by Muzzin et al. (2009) for a sample of  $z \sim 2$  galaxies. Therefore, we have chosen (BC03,  $Z_{\odot}$ , Kroupa, Calzetti) as our default set of SED-modeling assumptions, instead of having the metallicity, the IMF, the extinction curve, and the stellar models as free parameters.

In the following we describe the adopted approach to quantify the systematic effects on the derived SMFs of galaxies due to the different choices of SED-modeling settings.

#### 5.3.1. Variations on the default SED-modeling assumptions

We have derived stellar masses by fitting the observed SEDs with different sets of SED-modeling assumptions, by changing the stellar population synthesis models, the IMF, the metallicity, and the extinction law.

For the additional metallicities, we have used super-solar ( $Z = 2.5 \times Z_{\odot}$ ) and sub-solar ( $Z = 0.2 \times Z_{\odot}$ ) metallicities.

To explore the systematic effects due to different attenuation laws, the Milky Way (MW) extinction curve by Allen (1976) and the Small Magellanic Cloud (SMC) extinction curve (Prévot et al. 1984; Bouchet et al. 1985) were also used.

<sup>16</sup> We note that uncertainties related to field-to-field variations could be potentially correlated with photometric redshift uncertainties. However, spectroscopic complete high-mass samples at high redshift ( $z > 1$ ) do not yet exist, resulting in very little knowledge about an existing covariance between density estimates and photometric redshift systematics.

The main differences between the Calzetti et al. (2000) and the MW extinction laws lie in the ratio of total-to-selective absorption  $R_V = A_V/E(B-V)$  (4.05 versus 3.1, respectively) and in the Calzetti et al. (2000) law lacking the 2175 Å bump characteristic of MW dust mixtures. Otherwise, their wavelength dependence are fairly similar. The SMC law with  $R_V = 2.72$  also lacks the 2175 Å bump. In addition, it rises more steeply with decreasing wavelengths in the near-UV than the other two laws; in other words, the Calzetti et al. (2000) and the MW laws are much “grayer” at near-UV wavelengths. For (self-)consistency, the MW extinction law was used in combination with solar and super-solar metallicities, whereas the SMC curve was used with the sub-solar metallicity.

In addition to the pseudo-Kroupa (2001) IMF (discussed in § 3), we have used three additional IMFs, namely the Chabrier (2003) and two bottom-light IMFs.<sup>17</sup> Theoretical arguments and indirect observational evidence suggest that the stellar IMF may evolve with cosmic time, such that it is more weighted toward high-mass stars at higher redshift (see, e.g., Davé 2008; van Dokkum 2008; Wilkins et al. 2008). Recently, van Dokkum (2008) provided new constraints on the IMF at high redshift by comparing the evolution of the  $M=L$  ratios of early-type galaxies to their color evolution, finding a logarithmic slope of the IMF around  $1 M_{\odot}$  ( $\alpha = -0.3$ ) significantly flatter than the present-day value ( $\alpha = 1.3$ ). Moreover, assuming a Chabrier (2003)-like parameterization of the IMF with an evolving characteristic mass  $m_c$ , the analysis in van Dokkum (2008) implies a characteristic mass  $m_c = 1.9 M_{\odot}$  at  $z = 3-6$  (for solar metallicity). This IMF is best described as “bottom-light” rather than top-heavy, since it does not have a larger number of massive stars than a standard Chabrier (2003) IMF, but has a deficit of low-mass stars. For the bottom-light IMF, we adopted the parameterization defined in eq. 18 of van Dokkum (2008), with  $m_c = 1.9 M_{\odot}$ . We also used a second bottom-light IMF by adopting a smaller value for the characteristic mass,  $m_c = 0.3 M_{\odot}$ . This is the characteristic mass required to reproduced the top-heavy IMF with a simple cutoff at  $1 M_{\odot}$  invoked by Blain et al. (1999a) for sub-millimeter galaxies. The Chabrier (2003) IMF is recovered by using  $m_c = 0.079 M_{\odot}$ . Note that the bottom-light IMFs have been used in combination with the Maraston (2005) stellar population synthesis models.

Different stellar population synthesis models do not paint a consistent picture of evolution in the rest-frame NIR (probed by the IRAC bands). Therefore, we have explored systematic effects due to different stellar population synthesis models by performing SED modeling with the Maraston (2005) (MA05) and the Charlot & Bruzual (2008) (CB08) stellar population models. The BC03 and the MA05 models differ in several aspects: the stellar evolutionary tracks adopted to construct the isochrones, the synthesis technique and the treatment of the thermally pulsating asymptotic giant branch (TP-AGB) phase. The Padova stellar tracks used in BC03 include a certain amount of convective-core overshooting, whereas the Frascati tracks (Cassisi et al. 1997) used in MA05 do not. The two stellar evolutionary models also differ for the temperature distribution of the red giant branch phase. The differences in the rest-frame NIR originates mainly from a different implementation of the TP-AGB phase (Maraston et al. 2006). Following the fuel consumption approach, Maraston (2005) finds

<sup>17</sup> We note that (because of our fitting procedure) the shape of the SMF is identical for a Salpeter (1955) IMF, with a simple systematic shift of a factor of  $\sim 1.6$  to larger stellar masses.

TABLE 3  
CONSIDERED SETS OF SED-MODELING  
ASSUMPTIONS

<i>(model, Z, IMF, dust)</i>
<i>(BC03, Z<sub>⊙</sub>, Kroupa, Calzetti)</i>
<i>(BC03, 2.5 Z<sub>⊙</sub>, Kroupa, Calzetti)</i>
<i>(BC03, 0.2 Z<sub>⊙</sub>, Kroupa, Calzetti)</i>
<i>(BC03, Z<sub>⊙</sub>, Kroupa, MW)</i>
<i>(BC03, 2.5 Z<sub>⊙</sub>, Kroupa, MW)</i>
<i>(BC03, 0.2 Z<sub>⊙</sub>, Kroupa, SMC)</i>
<i>(BC03, Z<sub>⊙</sub>, Chabrier, Calzetti)</i>
<i>(CB08, Z<sub>⊙</sub>, Kroupa, Calzetti)</i>
<i>(MA05, Z<sub>⊙</sub>, Kroupa, Calzetti)</i>
<i>(MA05, Z<sub>⊙</sub>, Bottom-light <math>m_c = 0.3</math>, Calzetti)</i>
<i>(MA05, Z<sub>⊙</sub>, Bottom-light <math>m_c = 1.9</math>, Calzetti)</i>

The first element of the table is the default set of SED-modeling assumptions.

that this phase in stellar evolution has a substantial impact on the NIR luminosity for ages between 0.2 and 2 Gyr. Bruzual & Charlot (2003) follow the isochrone synthesis approach, characterizing properties of the stellar population per mass bin. The latter method leads to smaller luminosity contributions by TP-AGB stars. The CB08 stellar population synthesis models are generated with a recent version of the Bruzual & Charlot (2003) stellar population synthesis code which incorporates a new prescription by Marigo & Girardi (2007) for the TP-AGB evolution of low- and intermediate-mass stars. Whereas the Marigo & Girardi (2007) tracks used in CB08 account for 9 evolutionary stages in the TP-AGB (three in the O-rich phase, three in the C-rich phase, and three in the superwind phase), the BC03 models include only 1 evolutionary stage on each of these phases. The main effect of this added prescription is to improve the predicted NIR colors of intermediate-age stellar populations (Bruzual 2007; see also Charlot & Bruzual 2008).

We note that the star formation history is also a significant source of uncertainty. We have treated this implicitly in our Monte Carlo simulations, as we chose the best-fitting star formation history (out of three models) for each realization (see § 3). However, it is well known that masses can be altered significantly by adding "maximally old" components in the fits and generally by allowing more complex forms of the star formation history than simple exponentially declining models (e.g., Papovich et al. 2001; Wuyts et al. 2007). Fitting such complex star formation history models is beyond the scope of the present paper, but we note that multiple component fits tend to increase the masses, particularly for galaxies whose light is dominated by star bursts (see Wuyts et al. 2007; Pozzetti et al. 2007).

The considered sets of SED-modeling assumptions are summarized in Table 3.

### 5.3.2. Derivation of the SMFs

For each new combination of SED-modeling assumptions, we have derived the completeness limits in stellar mass and the SMFs with both the  $1=V_{\max}$  method and the maximum-likelihood analysis. Table 4 lists the SMFs of galaxies at  $1.3 < z < 2.0$ ,  $2.0 < z < 3.0$ , and  $3.0 < z < 4.0$  derived using the  $1=V_{\max}$  method for each combination of SED-modeling settings. Table 5 lists the best-fit Schechter function parameters  $\phi$ ,  $M_{\text{star}}^?$ , and  $?$  of the SMFs of galaxies at  $1.3 < z < 2.0$ ,  $2.0 < z < 3.0$ , and  $3.0 < z < 4.0$  derived using the maximum-likelihood analysis for each combination of SED-modeling

settings. In the left panel of Figures 6, the SMF of galaxies at  $1.3 < z < 2.0$  derived with the  $1=V_{\max}$  method for the default set (BC03, Z<sub>⊙</sub>, Kroupa, Calzetti) is compared to the SMFs derived for the other considered sets of SED-modeling assumptions. Similarly, the left panel of Figure 7 shows the different SMFs at  $1.3 < z < 2.0$  corresponding to the various sets of SED-modeling assumptions used in the maximum-likelihood analysis.

### 5.3.3. The effects of different SED-modeling assumptions

In this section we discuss in details the effects on the derived SMFs when changing the SED-modeling assumptions. A detailed analysis of the effects of the different SED-modeling assumptions on the estimated stellar masses is presented in Muzzin et al. (2009) for a sample of 34 *K*-selected galaxies at  $z \sim 2$ .

*Stellar population synthesis models* — With respect to the default SED-modeling assumptions, using the Maraston (2005) models results in derived SMFs with generally steeper low-mass end slopes  $\alpha$ , slightly smaller characteristic stellar masses  $M_{\text{star}}^?$  (by  $< 0.1$  dex), and smaller normalizations  $\phi$  (by 40%-50%). If the Charlot & Bruzual (2008) models are instead used, the derived SMFs have similar  $\alpha$ , significantly smaller  $M_{\text{star}}^?$  (by 0.1-0.2 dex), but similar  $\phi$ . However, due to the correlation between the Schechter function parameters  $\alpha$  and  $M_{\text{star}}^?$ , the SMFs derived using the Maraston (2005) and the Charlot & Bruzual (2008) models are in general very similar, resulting in a general decrease of the number densities of galaxies. This decrease is larger at the high-mass end, and smaller at the low-mass end.

*Metallicities* — Changing the metallicity from solar to sub-solar results in smaller characteristic densities  $\phi$  by 20%-30%, but no significant effect on  $\alpha$  and  $M_{\text{star}}^?$ . Conversely, using super-solar metallicity results in shallower  $\alpha$ , smaller  $M_{\text{star}}^?$  (by 0.1-0.2 dex), and larger  $\phi$  (by 30%-40%). The SMFs derived with sub-solar metallicities are similar to those derived using the default SED-modeling assumptions at the high-mass end, but with generally smaller number densities at the low-mass end. The SMFs derived with super-solar metallicities are instead characterized by a smaller number densities with respect to the SMFs derived with the default SED-modeling assumptions. This decrease is larger at the high-mass end, and much smaller at the low-mass end.

*Extinction laws* — Changing the adopted extinction law from Calzetti et al. (2000) to the MW law results in steeper  $\alpha$ , similar or slightly larger  $M_{\text{star}}^?$ , and significantly smaller  $\phi$  (by 20%-50%). The net results on the derived SMFs is a decrease in the number densities with respect to the SMFs derived with the Calzetti et al. (2000) extinction law. This decrease is small at the high-mass end and much larger at the low-mass end.

Using the SMC extinction curve in combination with sub-solar metallicity results in slightly shallower  $\alpha$ , smaller  $M_{\text{star}}^?$  (by 0.1-0.15 dex), and larger  $\phi$  (by 40%-60%) compared to the SMFs derived with Calzetti et al. (2000) extinction law and sub-solar metallicity. The net result is a decrease of the number densities at the high-mass end, and an increase of the number densities at the low-mass end. With respect to the default SED-modeling assumptions, using a SMC extinction curve in combination with sub-solar metallicity results in smaller number densities at the high-mass end and similar number densities at the low-mass end. The latter is due to

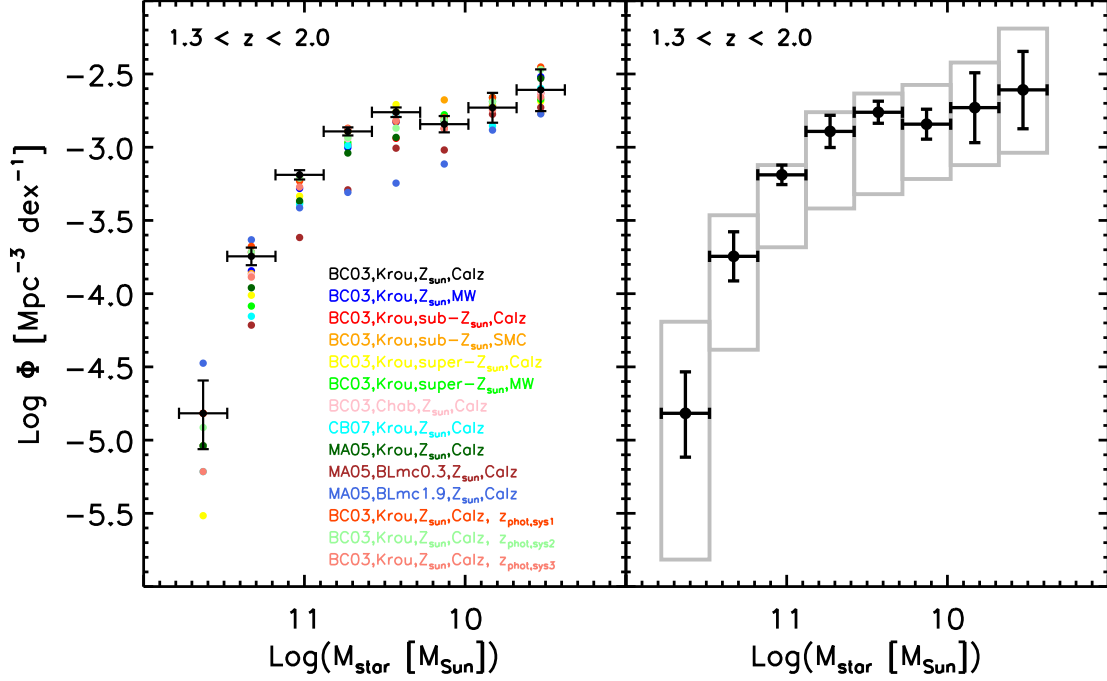


FIG. 6.— *Left panel:* SMF of galaxies at  $1.3 < z < 2.0$  derived with the  $1=V_{\max}$  method. The SMF corresponding to the default set of SED-modeling assumptions is plotted with black filled circles and  $1\sigma$  Poisson errors; the SMFs corresponding to different sets of SED-modeling settings and different combinations of template sets and template error functions are plotted with different colors (no errors plotted for clarity). *Right panel:* SMF of galaxies at  $1.3 < z < 2.0$  derived with the  $1=V_{\max}$  method and assuming the default set of SED-modeling settings; the black error bars now include the Poisson error, the error due to field-to-field variations, and the error due to photometric redshift random uncertainties. The gray boxes represent the total  $1\sigma$  errors, with the systematic uncertainties added linearly to the  $1\sigma$  random errors  $= (\frac{2}{P_{\text{Poi}}} + \frac{2}{\text{cv}} + \frac{2}{z_{\text{ran}}})^{1/2}$ .

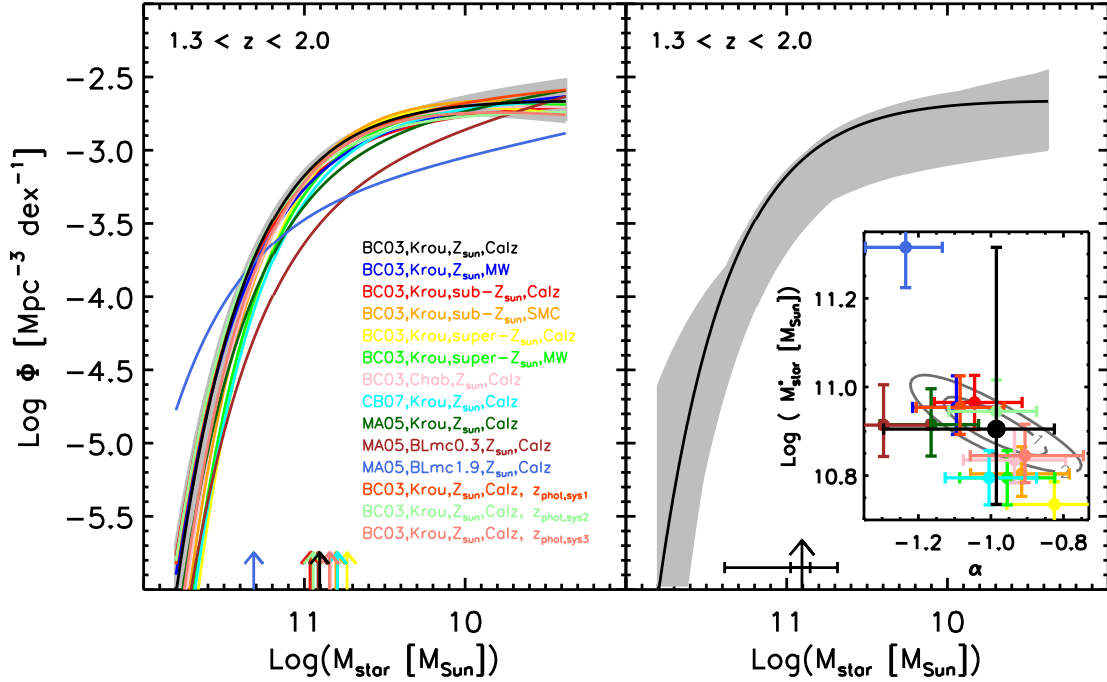


FIG. 7.— *Left panel:* SMF of galaxies at  $1.3 < z < 2.0$  derived with the maximum-likelihood analysis. The SMF and its  $1\sigma$  error corresponding to the default set of SED-modeling assumptions is plotted with black line and gray shaded region; the SMFs corresponding to different sets of SED-modeling settings and different combinations of template sets and template error functions are plotted with different colors (no errors plotted for clarity); the arrows represent the characteristic stellar masses  $M_{\text{star}}^{\text{char}}$ . *Right panel:* SMF of galaxies at  $1.3 < z < 2.0$  derived with the maximum-likelihood analysis and assuming the default set of SED-modeling settings (black solid curve); the gray shaded region represent the total  $1\sigma$  uncertainty, included the systematic uncertainties. The arrow represents  $M_{\text{star}}^{\text{char}}$ ; the smaller error bars represent the  $1\sigma$  error derived from the maximum-likelihood analysis; the larger error bars represent the total  $1\sigma$  error, with the systematic uncertainties added linearly. The insert shows the parameter space  $(-\log(M_{\text{star}}^{\text{char}}))$ , with the best-fit values corresponding to the default set of SED-modeling settings (black filled circle) and its corresponding  $1\sigma$  and  $2\sigma$  contour levels (solid gray ellipsoids), and the best-fit values corresponding to the other SED-modeling assumption sets and different combinations of template sets and template error functions (colored filled circles). If the bottom-light IMFs are not considered, the largest systematic effects on the derived SMFs are caused by the changes in the stellar population synthesis models and the combination of super-solar metallicity with the MW extinction law. Much larger systematic effects are found when the bottom-light IMFs are adopted (brown and light-blue symbols), both at the high- and low-mass ends.

TABLE 4  
SMFs FROM THE  $1=V_{\max}$  METHOD FOR THE DIFFERENT SED-MODELING ASSUMPTIONS

$\log(M_{\text{star}}=M_{\odot})$	Set 1	Set 2	Set 3	Set 4	Set 5	Set 6	Set 7	Set 8	Set 9	Set 10	Set 11	Set 12	Set 13	Set 14
	$\log([Mpc^{-3} \text{ dex}^{-1}])$													
<b>1.3 <math>z &lt; 2.0</math>:</b>														
11.63	-4.817	-5.516	-4.817	-5.039	-5.039	-5.039	-5.039	-5.215	-5.039	< -5.3	-4.475	-4.817	-4.914	-5.215
11.33	-3.745	-4.011	-3.717	-3.844	-4.085	-3.863	-3.873	-4.154	-3.960	-4.215	-3.632	-3.677	-3.718	-3.887
11.03	-3.189	-3.334	-3.194	-3.281	-3.378	-3.217	-3.211	-3.390	-3.367	-3.617	-3.414	-3.231	-3.211	-3.272
10.73	-2.892	-2.891	-2.985	-3.003	-2.968	-2.891	-2.942	-2.988	-3.040	-3.291	-3.308	-2.870	-2.933	-2.874
10.43	-2.761	-2.709	-2.939	-2.828	-2.762	-2.757	-2.768	-2.782	-2.933	-3.006	-3.245	-2.824	-2.870	-2.818
10.13	-2.843	-2.795	-2.872	-2.785	-2.778	-2.677	-2.817	-2.839	-2.823	-3.019	-3.115	-2.798	-2.813	-2.873
9.83	-2.730	-2.719	-2.730	-2.716	-2.688	-2.722	-2.749	-2.855	-2.660	-2.775	-2.883	-2.662	-2.690	-2.743
9.53	-2.608	-2.686	-2.631	-2.519	-2.673	-2.768	-2.630	-2.599	-2.530	-2.729	-2.772	-2.452	-2.469	-2.658
<b>2.0 <math>z &lt; 3.0</math>:</b>														
11.63	-5.067	-5.590	-4.988	-5.389	-5.590	-5.385	-5.383	-5.389	-5.389	< -5.6	-5.213	-5.066	-4.991	-4.929
11.34	-3.949	-4.133	-3.908	-4.455	-4.331	-4.078	-3.981	-4.500	-4.201	-5.098	-4.439	-3.955	-3.947	-4.235
11.05	-3.570	-3.641	-3.685	-3.701	-3.800	-3.619	-3.700	-3.711	-3.770	-3.999	-4.063	-3.638	-3.439	-3.630
10.76	-3.402	-3.309	-3.424	-3.451	-3.331	-3.354	-3.357	-3.417	-3.462	-3.741	-3.787	-3.368	-3.295	-3.309
10.47	-3.119	-3.292	-3.360	-3.353	-3.346	-3.148	-3.168	-3.259	-3.334	-3.479	-3.600	-3.218	-3.080	-3.203
10.18	-3.401	-3.208	-3.188	-3.175	-3.210	-3.235	-3.229	-3.281	-3.131	-3.258	-3.534	-3.265	-3.435	-3.526
9.89	-2.640	-2.911	-3.078	-2.813	-2.934	-2.938	-2.794	-2.963	-3.024	-3.311	-3.089	-2.703	-2.698	-2.499
<b>3.0 <math>z &lt; 4.0</math>:</b>														
11.66	-4.784	-5.191	-4.831	-4.978	-5.337	-4.688	-4.924	-5.468	-5.342	< -5.5	-5.179	-4.820	-4.969	-5.340
11.37	-4.282	-4.767	-4.438	-4.540	-4.676	-4.426	-4.417	-4.522	-4.577	-4.794	-4.809	-4.218	-4.273	-4.710
11.08	-4.025	-3.964	-4.131	-4.109	-4.078	-4.068	-3.996	-4.160	-4.068	-4.509	-4.508	-4.043	-3.879	-4.132
10.79	-3.929	-3.886	-4.099	-3.778	-3.973	-3.814	-3.964	-4.012	-3.983	-4.073	-4.210	-3.903	-3.920	-3.892
10.50	-3.433	-3.892	-3.788	-3.892	-3.892	-3.670	-4.068	-4.069	-4.068	-4.169	-3.968	-3.486	-3.486	-3.591
10.21	-3.141	-3.280	-3.092	-2.997	-3.070	-3.317	-3.214	-3.280	-3.070	-4.019	-3.547	-3.141	-3.141	-3.016

Set 1 = (BC03,Z ,Kroupa,Calzetti), default set of SED-modeling assumptions; Set 2 = (BC03,2.5 Z ,Kroupa,Calzetti); Set 3 = (BC03,0.2 Z ,Kroupa,Calzetti); Set 4 = (BC03,Z ,Kroupa,MW); Set 5 = (BC03,2.5 Z ,Kroupa,MW); Set 6 = (BC03,0.2 Z ,Kroupa,SMC); Set 7 = (BC03,Z ,Chabrier,Calzetti); Set 8 = (CB08,Z ,Kroupa,Calzetti); Set 9 = (MA05,Z ,Kroupa,Calzetti); Set 10 = (MA05,Z ,Bottom-light  $m_c = 0.3$ ,Calzetti); Set 11 = (MA05,Z ,Bottom-light  $m_c = 1.9$ ,Calzetti); Set 12 = (BC03,Z ,Z ,Kroupa,Calzetti), with *eazy\_v1.0\_nodust* and *TE.eazy\_v1.0\_nodust*; Set 13 = (BC03,Z ,Z ,Kroupa,Calzetti), with *eazy\_v1.0* and *TE.eazy\_v1.0\_nodust*; Set 14 = (BC03,Z ,Z ,Kroupa,Calzetti), with *br07\_default* and *TE.eazy\_v1.0*.

TABLE 5  
BEST-FIT SCHECHTER PARAMETERS FOR THE DIFFERENT SED-MODELING ASSUMPTIONS

Parameter	Set 1	Set 2	Set 3	Set 4	Set 5	Set 6	Set 7	Set 8	Set 9	Set 10	Set 11	Set 12	Set 13	Set 14
<b>1.3 <math>z &lt; 2.0</math>:</b>														
$\log(M_{\text{star}}^2=M_{\odot})$	-0.99	-0.83	-1.05	-1.10	-0.96	-0.92	-0.94	-1.01	-1.17	-1.30	-1.24	-1.09	-0.99	-0.91
$^2 [10^{-4} Mpc^{-3} \text{ dex}^{-1}]$	10.91	10.73	10.97	10.95	10.80	10.80	10.84	10.80	10.92	10.91	11.32	10.95	10.95	10.85
	10.17	13.78	7.49	7.35	10.65	12.72	11.01	9.62	6.38	3.64	2.01	8.46	8.54	10.77
<b>2.0 <math>z &lt; 3.0</math>:</b>														
$\log(M_{\text{star}}^2=M_{\odot})$	-1.01	-0.85	-1.03	-1.24	-0.89	-1.03	-1.03	-0.97	-1.21	-0.94	-1.36	-1.09	-0.98	-1.13
$^2 [10^{-4} Mpc^{-3} \text{ dex}^{-1}]$	10.96	10.83	10.99	10.94	10.80	10.88	10.90	10.83	10.93	10.62	11.17	10.96	10.94	10.98
	3.95	5.02	3.14	2.59	4.33	4.41	4.10	3.75	2.78	3.45	0.75	3.70	4.80	2.92
<b>3.0 <math>z &lt; 4.0</math>:</b>														
$\log(M_{\text{star}}^2=M_{\odot})$	-1.39	-1.39	-1.31	-1.92	-1.74	-1.61	-1.49	-0.96	-1.44	-1.06	-1.69	-1.44	-1.09	-1.59
$^2 [10^{-4} Mpc^{-3} \text{ dex}^{-1}]$	11.38	11.36	11.36	11.64	11.44	11.43	11.41	11.13	11.26	11.09	11.41	11.46	11.24	11.13
	0.53	0.42	0.44	0.11	0.22	0.34	0.40	0.65	0.49	0.42	0.13	0.37	0.90	0.65

SED-modeling assumption sets as in Tab. 4.



the fact that the effects at the low-mass end of changing the extinction curve and the metallicity are broadly similar, but opposite in sign.

*IMFs* — Using the Chabrier (2003) IMF in place of the pseudo-Kroupa (2001) IMF does not have a significant effect on the derived shape of the SMFs, with only a small decrease in the characteristic stellar mass  $M_{\text{star}}^2$  by 0.05 dex.

A more complex behavior is however found when the two bottom-light IMFs are considered. As shown in the left panel of Figures 7, the shapes of the SMFs derived using the bottom-light IMFs are significantly different from that of the SMF derived with the default SED-modeling assumptions. This is especially true for the bottom-light IMF with  $m_c = 1.9 M_\odot$ , characterized by a steeper low-mass end and a characteristic stellar mass larger by a factor of 2.5. This result is particularly important since it is commonly assumed that changing IMF in the SED-modeling results in a systematic shift of the derived SMF, leaving the shape of the SMF unchanged. This is clearly not the case for bottom-light IMFs: the more the IMF is skewed toward high-mass stars (i.e., the more deficient in low-mass stars the IMF is), the larger is the effect on the shape of the derived SMF.

Another very interesting result is the resulting higher number density of massive galaxies when using the bottom-light IMF with  $m_c = 1.9 M_\odot$  with respect to the SMFs derived with the other IMFs. This result might come unexpectedly at first. Naively, one would expect that, by making the IMF more deficient in low-mass stars, which dominate the stellar mass of a galaxy but contribute little to the integrated light, the derived stellar masses would be smaller compared to those derived from the other considered IMFs, as a consequence of a lowering of the  $M=L$  ratio. However, as already pointed out by van Dokkum (2008), the number of turn-off stars is also reduced for  $m_c \approx 0.4 M_\odot$ , and these stars dominate the light at rest-frame optical wavelengths. Moreover, the turn-off mass can be similar to  $m_c$ , meaning that the effect on the  $M=L$  ratio is not a constant, but depends on the age of the population. A final complication is the mass in stellar remnants, which is a larger fraction of the total stellar mass for more top-heavy IMFs. Using simple stellar evolutionary tracks but not full stellar population synthesis modeling, van Dokkum (2008) calculated the effects of changing characteristic mass on the  $M=L_V$  ratio for stellar populations of different ages, from 0.1 to 10 Gyr. They found that for young ages the  $M=L$  ratio steadily declines with increasing  $m_c$ , but the behavior is more complex when  $m_c$  becomes similar to the turn-off mass. Specifically, they found that for  $m_c \approx 1 M_\odot$  and old ages the mass function becomes remnant dominated, and the  $M=L$  ratios approach, or even exceed, those implied by a Salpeter (1955) IMF. We can directly test their conclusions by correctly treating the above issues with the available stellar population synthesis models constructed with the bottom-light IMFs. The effect of changing characteristic mass on the  $M=L_V$  ratio for different population ages is shown in Figure 8.

These results are consistent with those obtained by van Dokkum (2008), confirming that the  $M=L_V$  ratios for old stellar populations and high characteristic mass can approach, and even exceed, the  $M=L_V$  ratios implied by Chabrier (2003) and Salpeter (1955) IMFs, due to the stellar population becoming remnant-dominated.

The SMFs derived with the bottom-light IMFs in the SED-modeling assumptions can be now easily explained with the shown behavior of the  $M=L_V$  ratio in mind. When an IMF

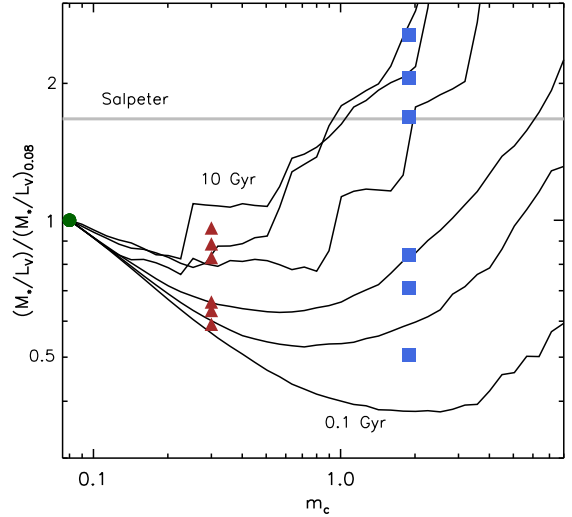


FIG. 8.— Effect of changing characteristic mass on the  $M=L_V$  ratio for stellar populations of ages 0.1, 0.3, 0.5, 3, 5, and 10 Gyr (from bottom to top) using stellar population synthesis models (filled symbols), following van Dokkum (2008). The solid curves, derived using simple stellar evolutionary tracks, were taken from van Dokkum (2008). Three different characteristic masses have been considered:  $m_c = 0.08$  (i.e., Chabrier 2003 IMF; dark green circle),  $m_c = 0.3$  (brown triangles), and  $m_c = 1.9 M_\odot$  (blue squares). For  $m_c = 1.9 M_\odot$  and old ages, the mass function becomes remnant dominated, and the  $M=L$  ratios approach, and even exceed, those implied by a Salpeter (1955) IMF (gray solid line).

with  $m_c = 0.3$  is adopted, the  $M=L$  ratios are always smaller, or at most comparable, to the  $M=L$  ratios derived with a Chabrier-like IMFs. Therefore, the derived stellar masses are always smaller, and the derived SMF is, broadly speaking, shifted to smaller masses. Note, however, that the dependence of the  $M=L$  ratio on age will affect the specific shape of the SMF. When an IMF with  $m_c = 1.9$  is adopted, the  $M=L$  ratios are larger than those derived with a Chabrier (2003) IMF when the age of the population is larger than 0.9 Gyr. Consequently, those galaxies which are fitted by ages older than 0.9 Gyr will have much larger stellar masses than those derived assuming a Chabrier (2003) IMF. On the contrary, those galaxies fitted by ages younger than 0.9 Gyr will have smaller stellar masses compared to those derived assuming a Chabrier (2003) IMF. The net effect on the derived SMF is a significant increase of the number densities of massive galaxies, which are usually characterized by old stellar population, and a decrease of the number densities of low-mass galaxies, which are usually characterized by young stellar population.

Note that the net effect on the derived SMF caused by assuming a bottom-light IMF is also a function of redshift, since the maximal age of the stellar population is limited by the age of the universe at that redshift. As the age of the stellar populations get younger going to higher redshifts, the effect on the SMF due to a bottom-light IMF will be closer to a systematic shift to smaller stellar masses without changing the shape significantly.

*Summary* — Broadly speaking, the different combinations of SED-modeling assumptions result in smaller estimates of the stellar masses with respect to the stellar masses derived using the default set. Consequently, the systematic effects on the SMFs are largest at the high-mass end of the SMFs, due to its steep slope and rapid changes in number density as function of stellar mass. The net effect on the derived SMFs is an average decrease of the number densities of galaxies at the high-mass end, while the systematic effects are generally smaller at the

low-mass end. If the bottom-light IMFs are not considered, the largest systematic effects are caused by the changes in the stellar population synthesis models and the combination of super-solar metallicity with the MW extinction law. The largest systematic effects are caused by the use of the bottom-light IMFs.

#### 5.3.4. The systematic uncertainties in the SMF due to different SED-modeling assumptions

The systematic effects on the SMFs due to different SED-modeling assumptions have been quantified by comparing the resulting SMFs with those derived using the default set of settings (*BC03, Z<sub>⊙</sub>, Kroupa, Calzetti*). Note that we implicitly assume that changes in the derived SMFs are the result of the changes we made to the model parameters. We cannot exclude subtle second-order effects that may influence the fitting procedure, but given the excellent agreement between the maximum-likelihood and the  $1=V_{\text{max}}$  estimators these are likely much smaller than the effects that we are measuring here.

For the  $1=V_{\text{max}}$  method, the systematic uncertainties of  $\Phi(M)$  have been estimated by taking, for each stellar mass bin, the difference between the maximum (and minimum) value of  $\Phi(M)$  allowed by all the considered combinations of SED-modeling settings and the value of  $\Phi(M)$  derived with the default set. These systematic uncertainties ( $\sigma_{\text{sys}}$ ) are listed in Table 1 and were then added linearly to the  $1\sigma$  errors ( $\sigma_{\text{tot}} = (\sigma_{\text{Poi}}^2 + \sigma_{\text{cv}}^2 + \sigma_{\text{z,ran}}^2)^{1/2}$  (which include the Poisson error, the error due to field-to-field variations, and the error due to photometric redshift random uncertainties) to obtain the total  $1\sigma$  errors. In the right panel of Figure 6, we show the SMF of galaxies at  $1.3 < z < 2.0$ , plotting the  $1\sigma$  errors with and without the contribution of the systematic effects due to different SED-modeling assumptions and different combinations of template sets and template error functions.

For the maximum-likelihood analysis, the systematic uncertainties on the Schechter function parameters have been estimated by taking the difference between the maximum and minimum values derived when using all the considered combinations of SED-modeling settings and the value corresponding to the default set. These systematic uncertainties ( $\sigma_{\text{sys}}$ ,  $M_{\text{sys}}^?$ , and  $\alpha_{\text{sys}}^?$ ), are listed in Table 2. The right panel of Figure 7 shows the SMF of galaxies at  $1.3 < z < 2.0$  derived with the default set of SED-modeling settings and the total  $1\sigma$  uncertainties after including the systematic uncertainties due to different SED-modeling assumptions and different combinations of template sets and template error functions; also plotted is the parameter space ( $-M_{\text{star}}^?$ ).

#### 5.4. Stellar Mass Functions with all uncertainties

Figure 9 shows the evolution of the SMF of galaxies from  $z = 4.0$  to  $z = 1.3$  including the contribution of random and systematic uncertainties in the error budget, i.e., the Poisson errors, the uncertainties due to cosmic variance and photometric redshift random errors, and the systematic uncertainties due to different SED-modeling assumptions and different combinations of template sets and template error functions. These errors are also listed in Table 1 and 2. Most of the systematic effects are in the same direction, with a resulting net effect of decreasing the observed number densities, especially at the high-mass end and in the highest targeted redshift interval. The  $(M_{\text{star}}^? - \alpha)$  plane is also plotted in Figure 10 showing the effect of systematic uncertainties on the Schechter function parameters.

The systematics uncertainties are a dominant contribution to the overall error budget. The largest contribution to the systematic uncertainties due to different SED-modeling assumptions are due to changes in the adopted IMF, specifically when a bottom-light IMF is used. The systematic uncertainties due to different combinations of template sets and template error functions in the estimate of the photometric redshifts are always smaller than the systematic uncertainties due to different SED-modeling assumptions, especially when the maximum-likelihood analysis is used. The maximum-likelihood analysis is indeed quite robust against photometric redshift errors, both random and systematic, and the dominant source of uncertainties are the systematic errors due to different SED-modeling assumptions. This is true at all redshifts but the highest redshift range, where Poisson errors represent a significant contribution to the error budget. As shown in the insert of Figure 7 for the redshift range  $1.3 < z < 2.0$ , the changes in the Schechter function parameters when using different SED-modeling assumptions, in comparison with the random errors, are very significant ( $> 2\sigma$ ). At  $2.0 < z < 3.0$ , the changes are slightly less significant, but still at the  $2\sigma$  level, while at  $3.0 < z < 4.0$ , where Poisson uncertainties are very large, the changes are mostly at the  $1\sigma$  level. When the  $1=V_{\text{max}}$  method is used, cosmic variance is the dominant source of random errors at  $1.3 < z < 2.0$  in all stellar mass bins, but it becomes comparable to the Poisson errors at  $2.0 < z < 3.0$ . The contribution of photometric redshift random uncertainties to the total error budget is generally smaller than Poisson errors, and increases going to higher redshifts. The relative contribution of systematic uncertainties is smallest at the highest targeted redshift interval,  $3.0 < z < 4.0$ , where random errors contribute significantly to the total error budget.

If the systematic uncertainties are included, the results highlighted in § 4.4 are no longer robust. In particular, we cannot exclude a strong evolution (by as much as a factor of  $\sim 50$ ) in the number density of the most massive ( $M_{\text{star}} > 10^{11.5}$ ) galaxies from  $z = 4.0$  to  $z = 1.3$ . We note that the effects of systematic uncertainties due to different SED-modeling assumptions are likely smaller when the redshift evolution is considered, as some errors would cancel out when comparing the SMFs at two different epochs. However, as the metallicity, IMF, and appropriate extinction law may all evolve with redshift, it is unclear to what extent this cancellation of errors actually occurs.

#### 5.5. Comparison with previous works

Figure 11 shows the comparison of the SMFs derived in this study with other works from the literature (see Appendix C for a detailed discussion of the individual works). As discussed above, cosmic variance and systematic uncertainties dominate the errors. However, most literature studies do not give estimates for these errors. Therefore, we show the comparison twice in Figure 11: the panels in the top two rows include only Poisson errors and uncertainties due to photometric redshift random errors, while the panels in the bottom two rows include all sources of error (with the exclusion of the systematic effects due to the bottom-light IMFs). To highlight similarities and differences between our SMFs and those derived in other works, we also plot  $\Delta = \log \Phi_{\text{others}} - \log \Phi_{\text{ours}}$  as function of stellar mass in the second- and fourth-row panels. We note that the error bars of the different surveys cannot be compared directly, as they were not derived in a uniform way.

From the top panels of Figure 11, it is obvious that our

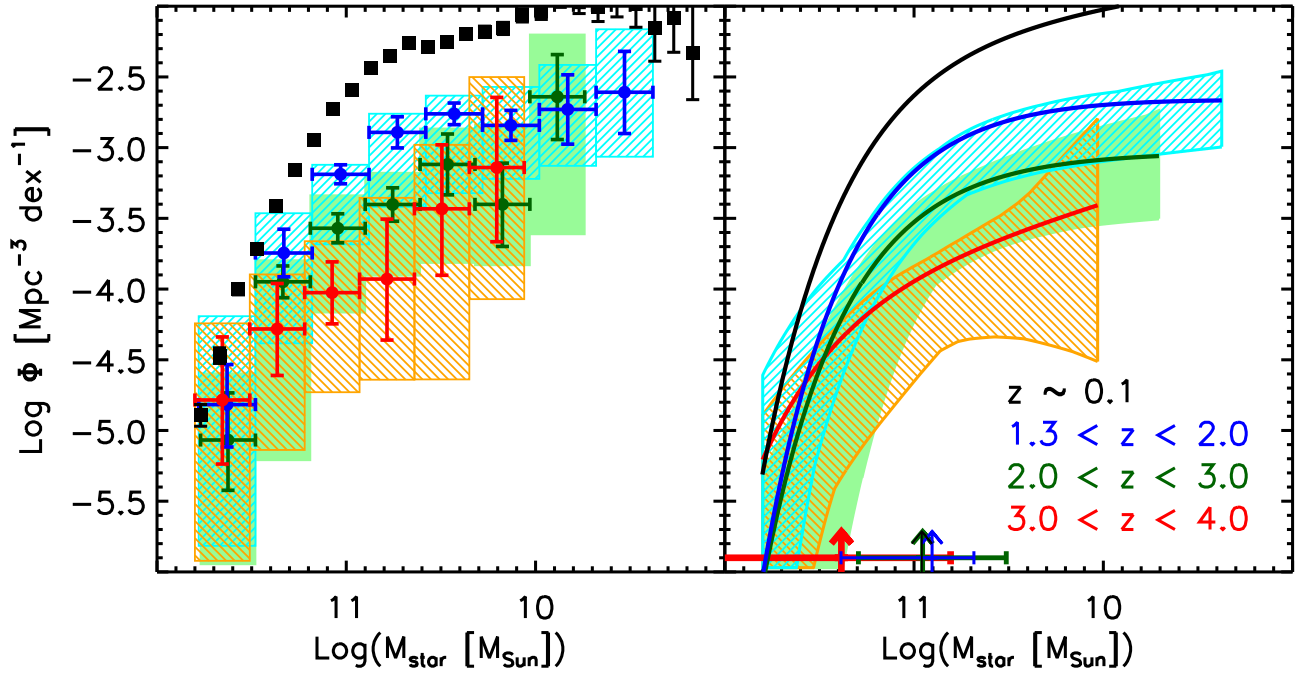


FIG. 9.— SMFs of galaxies at redshift  $1.3 < z < 2.0$  (blue),  $2.0 < z < 3.0$  (green), and  $3.0 < z < 4.0$  (red). *Left panel*: SMFs of galaxies derived using the  $1=V_{\max}$  method (filled circles); the error bars include Poisson errors, photometric redshift uncertainties, and errors due to cosmic variance. The shaded boxes (orange, green, and cyan, corresponding to the redshift intervals  $3.0 < z < 4.0$ ,  $2.0 < z < 3.0$ , and  $1.3 < z < 2.0$ , respectively) represent the total  $1-\sigma$  uncertainties in the measurements of the SMFs as described in § 5, with systematic errors added linearly to the plotted error bars. *Right panel*: SMFs of galaxies derived using the maximum-likelihood analysis (solid curves); the shaded regions represent the total  $1-\sigma$  uncertainties as described in § 5, including the systematic uncertainties. The arrows show the best estimates of  $M_{\text{star}}^2$  with their error bars including also systematic uncertainties.

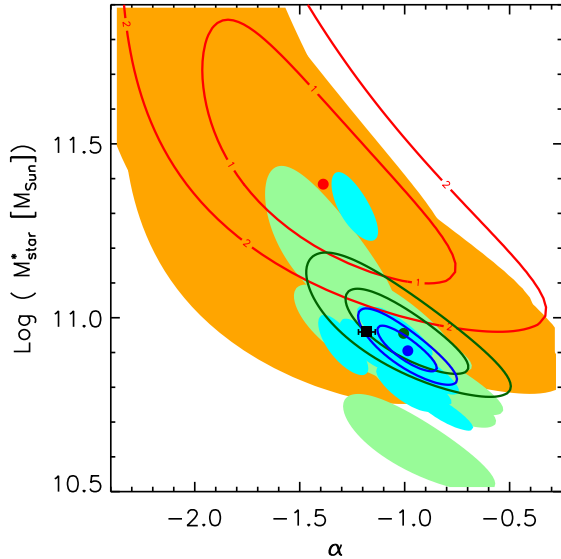


FIG. 10.— Parameter space ( $\alpha$  vs  $M_{\text{star}}^2$ ) derived from the maximum-likelihood analysis. The red, dark green, and blue filled circles are the best-fit values of  $\alpha$  and  $M_{\text{star}}^2$  at redshift  $3.0 < z < 4.0$ ,  $2.0 < z < 3.0$ , and  $1.3 < z < 2.0$ , respectively. The red, dark green, and blue curves represent their  $1$  and  $2$  contour levels, respectively. The filled regions show the  $1$  allowed values of  $\alpha$  and  $M_{\text{star}}^2$  after inclusion of the systematic uncertainties in the error analysis. The black filled square represents the redshift  $z = 0.1$  value from Cole et al. (2001).

SMFs agree with those from the literature for some redshift and stellar mass ranges, but disagree for others. Our SMFs are generally in good agreement with those from Elsner et al. (2008), Pérez-González et al. (2008), and Pozzetti et al. (2007). Broad agreement is also found with the SMFs at  $z < 3$  from Fontana et al. (2006), and with the high-mass end of the SMFs at  $z < 3$  from Drory et al. (2005). However, there is also significant disagreement between our SMFs and those

from the literature, and also between the works in the literature themselves, for some redshift and stellar mass ranges. The disagreements between the different SMFs increase with increasing redshift. Our SMFs fall somewhere in the middle of the SMFs from the literature. The largest disagreement is with the SMFs from Drory et al. (2005) at the low-mass end at all redshifts. At the high-mass end, the largest disagreement is with the SMFs from Fontana et al. (2006) at  $z = 3.5$ , from Pérez-González et al. (2008) at  $z = 2.5$ , and from Elsner et al. (2008) at  $z = 1.6$ . The large differences between the SMFs from Fontana et al. (2006) and Elsner et al. (2008) are interesting, since both were derived from the GOODS-MUSIC catalog. The former was derived from a  $K$ -selected catalog, while the latter from a  $z$ -selected catalog. We note, however, that Fontana et al. (2006) claim that their  $z$ -selected SMF is very similar to their  $K$ -selected one.

Once the systematic uncertainties are taken into account, as shown in the bottom panels of Figure 11, the SMFs derived in this work become consistent with most of the SMFs from the literature. The low-mass end of the SMFs at  $z = 2.5$  and  $z = 1.6$  from Drory et al. (2005) is still significantly steeper with respect to both our SMFs and the other SMFs from the literature. A possible explanation is the different way the completeness limits in stellar mass has been derived by Drory et al. (2005) (SSP-derived completeness), as this potentially over-corrects densities at the low-mass end.

We stress that most of the disagreements between the different measurements of the SMFs stem from an incomplete analysis of the errors. The errors on the SMFs from the literature include only Poisson errors (e.g., Drory et al. 2005), or Poisson errors and errors from photometric redshift uncertainties (but not cosmic variance, e.g. Fontana et al. 2006; Pérez-González et al. 2008; Elsner et al. 2008). Field-to-field variations is a significant source of errors when the SMF is derived using the  $1=V_{\max}$  method. This is true at all redshifts,

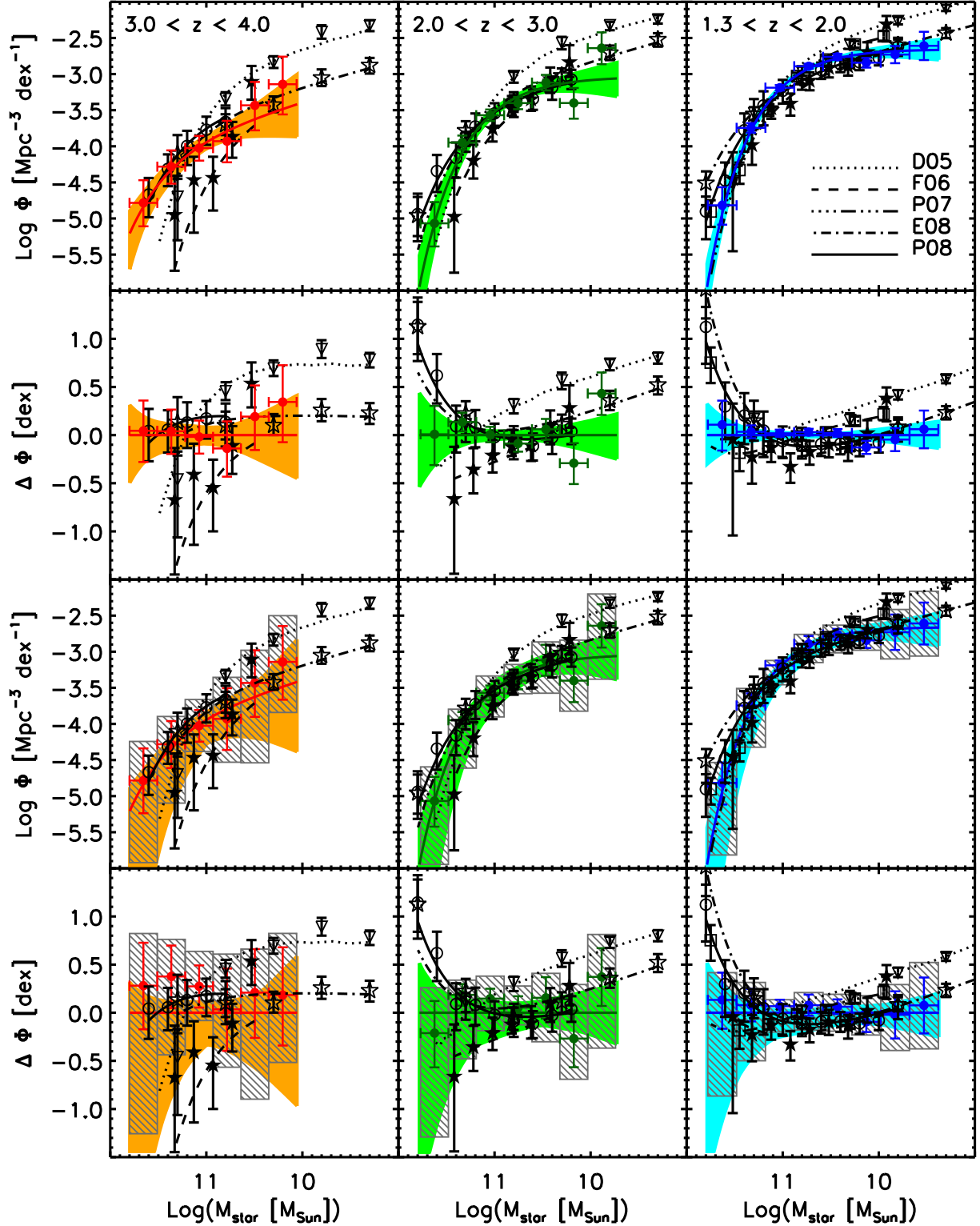


FIG. 11.— Comparison between the SMFs derived from this work and previous measurements from the literature. *First row:* The SMFs derived from this work are shown as filled red, dark green, and blue circles ( $1=V_{\max}$  method) and solid curves (maximum-likelihood analysis). The  $1\sigma$  error bars of the  $1=V_{\max}$  measurements include Poisson errors and uncertainties from photometric redshift random uncertainties, but not cosmic variance and systematic uncertainties. Similarly, the  $1\sigma$  error of the maximum-likelihood measurements (orange, green, and cyan shaded regions) do not include systematic uncertainties. Previous works are plotted as filled stars and dashed curves (Fontana et al. 2006; F06); open circles and solid curves (Pérez-González et al. 2008; P08); open stars and dot-dashed curves (Elsner et al. 2008; E08); open triangles and dotted curves (Drory et al. 2005; D05); open squares and long dot-dashed curves (Pozzetti et al. 2007; P07). *Second row:* Symbols as in the first row panels, but now the differences between the SMFs from the literature and those derived in this work,  $\Delta \phi = \log \phi_{\text{others}} - \log \phi_{\text{ours}}$ , are plotted as a function of stellar mass. *Third and fourth row panels:* Symbols as in first and second row panels, respectively, with cosmic variance added in quadrature to the error bars, and systematic uncertainties now included in the total error budget represented by the shaded gray boxes (for the  $1=V_{\max}$  points) and shaded orange, green, and cyan regions (for the maximum-likelihood measurements). The systematic effects due to the bottom-light IMFs are not included. Most of the disagreements between the different measurements of the SMFs stem from an incomplete analysis of the errors. A comprehensive analysis of random and systematic uncertainties is necessary to reconcile the different measurements of the high- $z$  SMFs.



especially at the high-mass end, but cosmic variance dominates the error budget at  $z \gtrsim 1.5$ . The maximum-likelihood estimator, unbiased with respect to density inhomogeneities, has been applied only by Fontana et al. (2006) and Pozzetti et al. (2007), while the other works have simply fitted the SMFs derived with the  $1=V_{\max}$  with a Schechter function. Finally, it is extremely important to include the systematic uncertainties due to different SED-modeling assumptions, which dominate the total error budget and are necessary to reconcile the different measurements of the high- $z$  SMFs.

## 6. DENSITIES

In this section we present estimates of the stellar mass density  $\rho_{\text{star}}$  derived by integrating the best-fit Schechter function obtained from the maximum-likelihood analysis (no use of the  $1=V_{\max}$  results has been done in the estimate of the stellar mass densities). The stellar mass density (obtained by integrating the SMF derived from the maximum-likelihood analysis) is a more robust measurement than the Schechter function parameters  $M_{\text{star}}^*$ ,  $\phi$ , and  $\alpha$ , because the errors in these parameters are highly correlated. Stellar mass densities have been estimated adopting three different integration intervals:  $8 < M < 13$ , where the integration was performed for stellar masses  $10^8 < M_{\text{star}} = M < 10^{13}$ ;  $10 < M < 11$ , where the integration was performed for stellar masses  $10^{10} < M_{\text{star}} = M < 10^{11}$ ; and  $11 < M < 12$ , where the integration was performed for stellar masses  $10^{11} < M_{\text{star}} = M < 10^{12}$ , i.e. massive galaxies. These estimates are listed in Table 6, along with the  $1\sigma$  errors and the values of the stellar mass density at  $z = 0.1$  estimated from the SMF of Cole et al. (2001). Note that the contribution of galaxies less massive than  $M_{\text{star}} = 10^8 M_{\odot}$  to the global stellar mass density is negligible if the Schechter parameterization of the SMF is a good approximation and valid also at stellar masses smaller than probed by our composite sample.

The  $1\sigma$  errors on the stellar mass densities have been estimated by deriving the distribution of all of the values of  $\rho_{\text{star}}$  allowed within the  $1\sigma$  solutions of the Schechter function parameters from the maximum-likelihood analysis. The contribution to the total error budget from photometric redshift random uncertainties (derived from the 100 Monte Carlo realizations described in § 5.1) was added in quadrature. The  $1\sigma$  errors including the systematic uncertainties were estimated in the same way by deriving the distribution of all of the values of  $\rho_{\text{star}}$  allowed within the  $1\sigma$  solutions obtained using different SED-modeling assumptions and different combinations of template sets and template error functions to estimate the photometric redshifts.

In Figure 12 we show the evolution of the total stellar mass density as a function of redshift, together with a compilation of results from the literature. The values from the literature, derived assuming a Salpeter (1955) IMF, have been scaled to a pseudo-Kroupa (2001) IMF by dividing the stellar mass densities by a factor of 1.6. The values from the literature of the stellar mass density converted to our IMF are listed in Table 7. The measured evolution of the total stellar mass density from  $z = 4.0$  to  $z = 1.3$  is broadly consistent with most previous measurements in the literature. Our measurements are among the currently most accurate measurements of the total stellar mass density at these redshifts. This is due to the large surveyed area, the large number of independent fields, and the high-quality of the optical-to-MIR data. Only the value at  $z = 3.5$  is characterized by a large random error, due to the large uncertainties on the low-mass end slope of the derived SMF. Moreover, our measurements are the first to include a

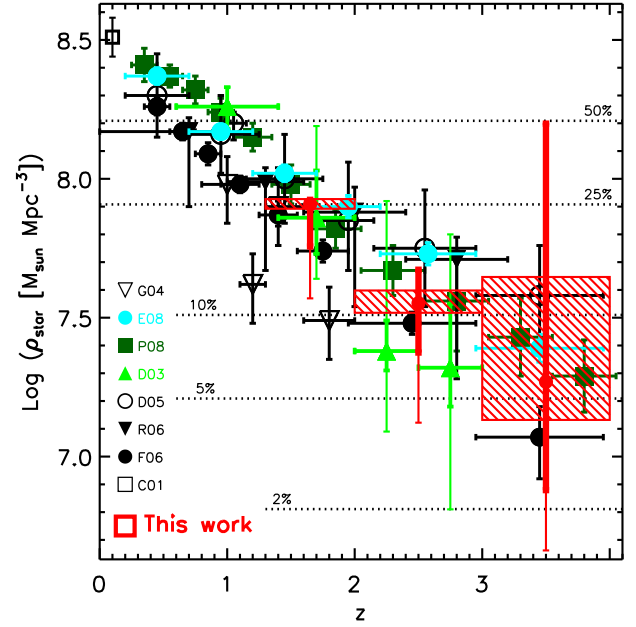


FIG. 12.— Evolution as a function of redshift of the global stellar mass density estimated by integrating the SMFs over the stellar mass range  $10^8 < M_{\text{star}} = M < 10^{13}$  (the contribution to the total stellar mass density of galaxies with  $M_{\text{star}} < 10^8 M_{\odot}$  is negligible if the Schechter parameterization of the SMF is valid also at stellar masses smaller than probed by our sample). Red symbols represent the total stellar mass densities estimated in this work (shaded boxes do not include the systematic uncertainties while error bars do; the thick error bars do not include the systematic effect of the two bottom-light IMFs, while the thin error bars do). The estimates of the total stellar mass densities from the literature were taken from Cole et al. (2001) (open square); Dickinson et al. (2003) (filled green triangles; thick error bars include random errors and cosmic variance alone, while the thin error bars include the systematic uncertainties due to different SED-modeling assumptions); Glazebrook et al. (2004) (open upside-down triangles; error bars including Poisson errors only); Drory et al. (2005) (open circles); Elsner et al. (2008) (filled cyan circles); Fontana et al. (2006) (filled circles); Pérez-González et al. (2008) (filled dark green squares); and Rudnick et al. (2006) (filled upside-down triangles; error bars including random errors and uncertainties due to cosmic variance). For the measurements from the literature, only Poisson errors and errors due to photometric redshift uncertainties (as derived in the corresponding work), are plotted without uncertainties due to cosmic variance and systematic errors, unless stated otherwise. The horizontal dotted lines represent 50%, 25%, 10%, 5%, and 2% (from top to bottom, respectively) of the total stellar mass density at  $z = 0.1$ . The stellar mass density has increased by a factor  $17^{+7}_{-10}$ ,  $9 \pm 1$ , and  $4 \pm 0.2$  from  $z = 3.5$ ,  $z = 2.5$ , and  $z = 1.65$ , respectively, down to  $z = 0.1$ . A much stronger evolution with redshift of the stellar mass density is however allowed once the systematic uncertainties are taken into account.

comprehensive analysis of random and systematic uncertainties in the error budget. Note that the mass density at  $z > 3$  is very poorly constrained when systematic uncertainties are included. We stress that this arises despite the fact that our sample is arguably the best suited for studying the total stellar mass density (as it samples both the low-mass and high-mass end in a homogeneous way). All previous studies in the literature suffer from similar, or larger, uncertainties.

The total stellar mass density has increased by a factor of  $17^{+7}_{-10}$ ,  $9 \pm 1$ , and  $4 \pm 0.2$ , from redshift  $z = 3.5$ ,  $z = 2.5$ , and  $z = 1.65$ , respectively, down to redshift  $z = 0.1$ . Due to the systematic uncertainties on the derived stellar mass densities (represented with thin error bars in Figure 12), a much stronger evolution with redshift of the total stellar mass density than previously measured is actually allowed. Systematic uncertainties still allow for an increase as large as a factor of 70, 25, and 9 of the global stellar mass density (44, 14, and 6, if the effects of the bottom-light IMFs are excluded) from redshift  $z = 3.5$ ,  $z = 2.5$ , and  $z = 1.65$ , respec-



TABLE 6  
STELLAR MASS DENSITIES

Redshift Range	$\log \frac{8 < M < 13}{\text{star}} \text{ Mpc}^{-3}$	$\log \frac{10 < M < 11}{\text{star}} \text{ Mpc}^{-3}$	$\log \frac{11 < M < 12}{\text{star}} \text{ Mpc}^{-3}$
$z = 0.1$	8.51 0.07	8.27 0.07	7.92 0.07
$1.3 < z < 2.0$	$7.91^{+0.02(0.02)(0.02)}_{-0.02(0.03)(0.06)}$	$7.68^{+0.02(0.04)(0.04)}_{-0.02(0.04)(0.06)}$	$7.38^{+0.07(0.09)(0.08)}_{-0.06(0.02)(0.08)}$
$2.0 < z < 3.0$	$7.55^{+0.05(0.12)(0.12)}_{-0.04(0.03)(0.08)}$	$7.31^{+0.05(0.11)(0.11)}_{-0.05(0.08)(0.14)}$	$7.07^{+0.08(0.13)(0.13)}_{-0.09(0.10)(0.09)}$
$3.0 < z < 4.0$	$7.27^{+0.37(0.93)(0.93)}_{-0.13(0.61)(0.39)}$	$6.88^{+0.19(0.49)(0.49)}_{-0.22(0.67)(0.50)}$	$6.91^{+0.13(0.13)(0.13)}_{-0.16(0.94)(0.73)}$

Stellar mass density estimated by integrating the best-fit Schechter SMF over the specified stellar mass range. The quoted  $1\sigma$  errors include Poisson errors and errors due to photometric redshift uncertainties; the numbers in parenthesis are the  $1\sigma$  errors including the systematic uncertainties due to different SED-modeling assumptions and different combination of template set and template error function used in the estimate of the photometric redshifts; in the second number in parenthesis, the effect of the bottom-light IMFs is excluded.

TABLE 7  
STELLAR MASS DENSITIES FROM THE LITERATURE

Redshift Range	$\log \frac{8 < M < 13}{\text{star}} \text{ Mpc}^{-3}$	Redshift Range	$\log \frac{8 < M < 13}{\text{star}} \text{ Mpc}^{-3}$
Dickinson et al. (2003)		Glazebrook et al. (2004)	
$0.6 < z < 1.4$	8.26 0.08	$0.8 < z < 1.1$	$7.98^{+0.10}_{-0.14}$
$1.4 < z < 2.0$	$7.86^{+0.17(0.33)}_{-0.13(0.22)}$	$1.1 < z < 1.3$	$7.62^{+0.11}_{-0.14}$
$2.0 < z < 2.5$	$7.58^{+0.11(0.54)}_{-0.07(0.29)}$	$1.3 < z < 1.6$	$7.90^{+0.14}_{-0.14}$
$2.5 < z < 3.0$	$7.52^{+0.23(0.48)}_{-0.14(0.51)}$	$1.6 < z < 2.0$	$7.49^{+0.12}_{-0.14}$
Drory et al. (2005)		Fontana et al. (2006)	
$0.25 < z < 0.75$	8.30 0.15	$0.4 < z < 0.6$	8.26 0.03
$0.75 < z < 1.25$	8.16 0.15	$0.6 < z < 0.8$	8.17 0.02
$1.25 < z < 1.75$	8.00 0.16	$0.8 < z < 1.0$	8.09 0.03
$1.75 < z < 2.25$	7.85 0.20	$1.0 < z < 1.3$	7.98 0.02
$2.25 < z < 3.00$	7.75 0.20	$1.3 < z < 1.6$	7.87 0.05
$3.00 < z < 4.00$	7.58 0.20	$1.6 < z < 2.0$	7.74 0.04
Pérez-González et al. (2008)		$2.0 < z < 3.0$	7.48 0.04
$0.2 < z < 0.4$	8.41 0.06	$3.0 < z < 4.0$	$7.07^{+0.11}_{-0.15}$
$0.4 < z < 0.6$	8.37 0.04	Rudnick et al. (2006)	
$0.6 < z < 0.8$	8.32 0.05	$0.0 < z < 1.0$	$8.17^{+0.05}_{-0.27}$
$0.8 < z < 1.0$	8.24 0.05	$1.0 < z < 1.6$	$7.99^{+0.05}_{-0.32}$
$1.0 < z < 1.3$	8.15 0.05	$1.6 < z < 2.4$	$7.88^{+0.09}_{-0.34}$
$1.3 < z < 1.6$	7.95 0.07	$2.4 < z < 3.2$	$7.71^{+0.08}_{-0.43}$
$1.6 < z < 2.0$	7.82 0.07	Elsner et al. (2008)	
$2.0 < z < 2.5$	7.67 0.08	$0.25 < z < 0.75$	8.37 0.03
$2.5 < z < 3.0$	7.56 0.18	$0.75 < z < 1.25$	8.17 0.02
$3.0 < z < 3.5$	7.43 0.14	$1.25 < z < 1.75$	8.02 0.03
$3.5 < z < 4.0$	7.29 0.13	$1.75 < z < 2.25$	7.90 0.04
		$2.25 < z < 3.00$	7.73 0.04
		$3.00 < z < 4.00$	7.39 0.05

All the values from the literature have been divided by 1.6 to convert to the pseudo-Kroupa (2001) IMF used in this work. The quoted errors include only Poisson errors and errors due to photometric redshift uncertainties, without uncertainties due to cosmic variance and systematic errors, unless stated otherwise. The quoted errors of Dickinson et al. (2003) include random errors and cosmic variance, with the numbers in parenthesis including the systematic uncertainties due to different SED-modeling assumptions; The quoted errors of Rudnick et al. (2006) include random errors and uncertainties due to cosmic variance.

tively, to  $z = 0.1$ . However, the effects of systematic uncertainties due to different SED-modeling assumptions are likely smaller when the redshift evolution is considered, as some errors would cancel out when comparing the stellar mass densities at two different epochs.

If only random errors are taken into account, there are a few measurements from the literature that are in significant disagreement with ours. The stellar mass density in Elsner et al. (2008) at  $z = 2.5$  is significantly larger than our measurement by about 60%. We note however that the error bars of the measurements from Elsner et al. (2008) only include random errors, but not uncertainties from cosmic variance and systematic errors. Because the analysis of Elsner et al. (2008) is based on the single, relatively small, field of GOODS-CDFS, field-to-field variance is a particular important source of errors. We stress the importance of a comprehensive analysis of the errors, including systematic uncertainties. Excluded our works, the only measurements of the stellar mass density including a complete analysis of all the errors, including systematic uncertainties, come from the work of Dickinson et al. (2003). Because Dickinson et al. (2003) include both cosmic variance and systematic uncertainties in their error budget, they are consistent with ours, despite their estimates of the stellar mass densities lying systematically below ours. Our measurements are characterized by much smaller errors due to our much larger surveyed area (by a factor of  $\sim 80$ ).

We finally note that at  $z > 2$ , we cannot constrain the low-mass end of the SMFs very well, becoming incomplete at  $10^{10} \text{ M}_{\odot}$ . If the SMF is much steeper at the low-mass end than indicated by our maximum-likelihood analysis, we could be missing a significant fraction of the integrated stellar mass. Very recently, Reddy & Steidel (2009) suggested that up to 50% of the total stellar mass at  $1.9 < z < 3.4$  is in faint-UV galaxies with masses smaller than  $10^{10} \text{ M}_{\odot}$  (compared to 10%-20% from an extrapolation of our Schechter fits). However, Reddy & Steidel (2009) do not measure stellar masses directly, but convert UV luminosity to stellar mass. Significantly deeper NIR observations are required to directly probe and constrain the low-mass end of the high- $z$  SMF.

## 7. COMPARISON WITH MODEL PREDICTIONS

In this section we compared the derived SMFs of galaxies at  $1.3 < z < 4.0$  with those predicted by the latest generation of galaxy formation models. Specifically, we have included the predictions from the semi-analytic models of Monaco et al. (2007), Somerville et al. (2008), and Wang et al. (2008), which include active galactic nuclei (AGN) feedback. We refer to those papers for detailed descriptions of their models, and to Fontanot et al. (2009) for a detailed comparison of these models. A Chabrier (2003) IMF has been assumed in all

models. We have therefore scaled their predictions to match our pseudo-Kroupa IMF by multiplying their stellar masses by 1.12. The model-predicted SMFs have been convolved with a normal distribution of standard deviation 0.25 dex, intended to represent measurement errors in  $\log M_{\text{star}}$ .

The semi-analytic model of Monaco et al. (2007), MORGANA, attempts, through modeling of cooling, star formation, feedback, galactic winds and superwinds, AGN activity and AGN feedback, to move from a phenomenological description of galaxy formation to a fully physically motivated one. We refer to Monaco et al. (2007) for a detailed description of all physical processes included in MORGANA. The predicted SMFs and stellar mass densities from the MORGANA model adopted in this work were derived assuming a WMAP-3 cosmology (Spergel et al. 2007) and including some minor improvements with respect to Monaco et al. (2007) (Lo Faro et al., in prep.).

The model predictions from Wang et al. (2008) were derived using the Garching semi-analytic model implemented on the Millennium dark matter simulation described in Springel et al. (2005). Specifically, the semi-analytic model described in De Lucia & Blaizot (2007) was used, which built on previous works by the “Munich” galaxy formation group (see Kauffmann & Heahnel 2000; Springel et al. 2001; and De Lucia et al. 2004 for detailed descriptions of the scheme for building the merger tree and the prescriptions adopted to model the baryonic physics, most notably those associated with the growth of and the feedback from black holes in galaxy nuclei and the cooling model). Here, we specifically consider the “C” model in Wang et al. (2008), which assumes a WMAP-3 cosmology. This change in cosmology results in a significant delay of structure formation in comparison with WMAP-1 results. Therefore, to compensate for the delay in structure formation, model “C” has twice as much the star formation efficiency with respect to the efficiency assumed by De Lucia & Blaizot (2007). This increase in efficiency has to be compensated by much higher feedback efficiencies (both from supernovae and from AGN) to prevent the overproduction of stars at late times.

The semi-analytic model of Somerville et al. (2008), built on the previous models described in Somerville & Primack (1999) and Somerville et al. (2001), presents several improvements, including, but not limited to, tracking of a diffuse stellar halo component built up of tidally destroyed satellites and stars scattered in mergers, galaxy-scale AGN-driven winds, fueling of black holes with hot gas via Bondi accretion, and heating by radio jets. The prediction from the Somerville et al. (2008) semi-analytic model are taken from their fiducial model WMAP-3 model, which adopts a fraction  $f_{\text{scatter}} = 0.4$  of the stars in merged satellite galaxies added to a diffuse component distributed in a very extended halo or envelope.

Figures 13 and 14 show the comparison between the SMFs measured in this work (with the exclusion of the systematic effects due to the bottom-light IMFs) and those predicted by the models. Figure 13 shows the comparison for the model-predicted SMFs without convolution with a normal distribution, while Figure 14 shows the comparison for the model-predicted SMFs convolved with a normal distribution of standard deviation 0.25 dex. To highlight similarities and differences between our SMFs and the model-predicted SMFs, we also plot  $\Delta \log M_{\text{star}} = \log M_{\text{models}} - \log M_{\text{ours}}$  as function of stellar mass in the bottom panels of Figures 13 and 14. Broadly speaking, the predicted SMFs are too steep with respect to the observed SMFs. If the comparison is done with the not-

convolved model-predicted SMFs (see Figure 13), in the redshift range  $1.3 < z < 2.0$ , where the high-mass end is reasonably well reproduced by all but the model of Wang et al. (2008), all models significantly over-predict the number density of galaxies below the characteristic stellar mass. This is true also in the redshift range  $2.0 < z < 3.0$ , but now all models also significantly under-predicting the number densities of the massive galaxies. The disagreement at the high-mass end is even more pronounced in the redshift range  $3.0 < z < 4.0$ , where all models show a significant deficiency of massive galaxies with respect to observations. If the comparison between the observed and the model-predicted SMFs is instead performed using the convolved model-predicted SMFs, intended to represent measurement errors in  $\log M_{\text{star}}$  (see Figure 14), the disagreements at the high-mass end are significantly reduced, although the model of Somerville et al. (2008) now tends to over-predict the number density of galaxies in the redshift range  $1.3 < z < 2.0$  at all stellar masses, while the model of Monaco et al. (2007) still significantly under-predicts the number density of massive galaxies at  $3.0 < z < 4.0$ . Convolution of the model-predicted SMFs does not instead help at all to solve the discrepancies below the characteristic stellar mass. These results are in qualitative agreement with the comparison of observed and predicted rest-frame optical luminosity functions performed at  $2.0 < z < 3.3$  by Marchesini & van Dokkum (2007), who found that all models significantly over-predict the observed number density of galaxies at the faint-end.

As already pointed out in Somerville et al. (2008), potentially serious discrepancies, common to all of the CDM-based semi-analytic models, are connected with low-mass galaxies. This is indeed what we find, although the presence of a significant population of very massive galaxies out to redshift  $z = 3-4$  and the little observed evolution in its number densities from  $z = 4.0$  to  $z = 1.3$  highlight other potential problems within the theoretical models.

The different comparison between observed and predicted SMFs in the two stellar mass regimes (below and above  $M_{\text{star}} = 10^{11} M_{\odot}$ ) is also shown in Figures 15 and 16, where the evolution of  $\frac{10 < M < 11}{\text{star}}$  and  $\frac{11 < M < 12}{\text{star}}$  as function of redshift are compared to the predictions from the semi-analytic models before and after convolution of the model-predicted SMFs with a normal distribution of standard deviation 0.25 dex, respectively.

If no convolution with a normal distribution of standard deviation 0.25 dex is applied to the model-predicted SMFs (Figure 15), all models severely under-predict the stellar mass density of the massive galaxies at all redshifts. Only the model of Somerville et al. (2008) well match the stellar mass density of massive galaxies at  $1.3 < z < 2.0$ , although it suffers from the same deficit of massive galaxies at  $z > 2.0$ . As in the comparison with the SMFs, if the convolved model-predicted SMFs are adopted (Figure 16), the disagreements for the stellar mass densities of massive galaxies is significantly reduced, especially for the model of Wang et al. (2008) which now reasonably well reproduces the evolution of the stellar mass density of massive galaxies over the entire redshift range  $0.0 < z < 4.0$ . However, the model of Monaco et al. (2007) still under-predicts significantly the stellar mass density of massive galaxies at  $3.0 < z < 4.0$ , while the model of Somerville et al. (2008) now over-predicts the stellar mass density of massive galaxies at  $1.3 < z < 2.0$ . The moderate success (after convolution) at the high-mass end is however counter-balanced by the failure in predicting the evolution of

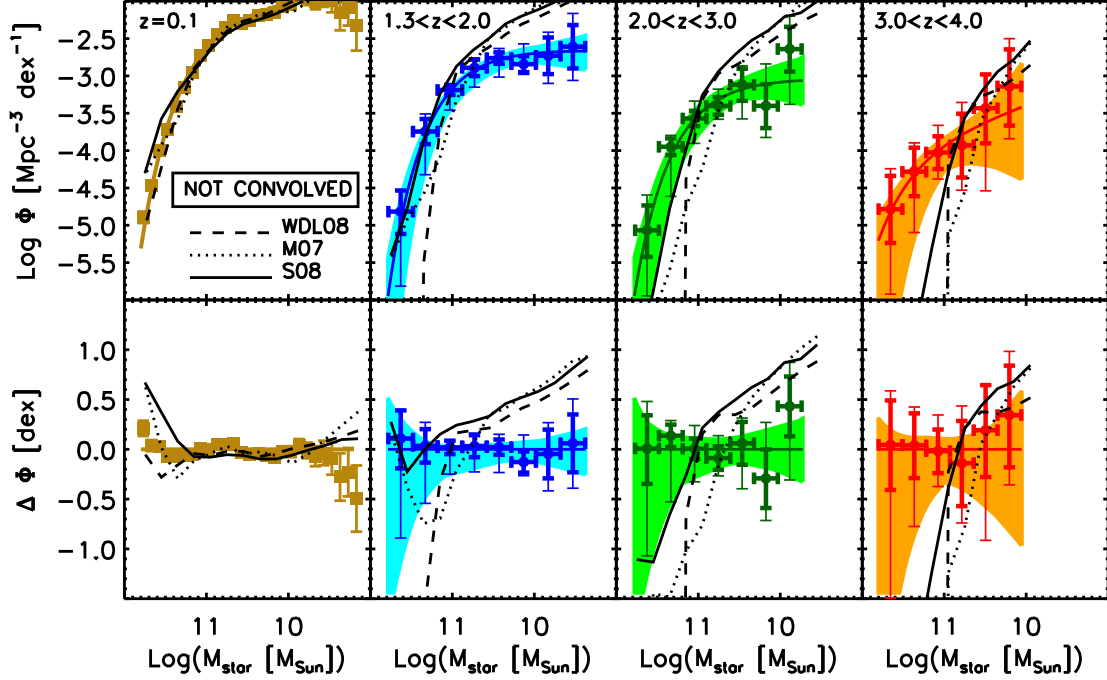


FIG. 13.— Comparison between the observed SMFs and the semi-analytic model predicted SMFs not convolved with a normal distribution of standard deviation 0.25 dex. The predicted SMFs are represented by black curves: solid for the Somerville et al. (2008) model, dotted for the Monaco et al. (2007) model, and dashed for the Wang et al. (2008) model. Red, green, and blue filled circles represent the SMFs measured from the  $1=\nu_{\text{max}}$  method; the thick error bars include Poisson errors, cosmic variance, and the uncertainties from photometric redshift random errors; the thin error bars include the systematic uncertainties, with the exclusion of the effect due to the use of the bottom-light IMFs for consistency with the theoretical models. Red, green, and blue solid curves represent the SMFs measured from the maximum-likelihood analysis. The shaded regions represent the total  $1-\sigma$  errors, including the systematic uncertainties. The top panels show the comparisons between the observed and the model-predicted SMFs. The bottom panels show the differences between the model-predicted SMFs and those derived in this work,  $\Delta\phi = \log \phi_{\text{models}} - \log \phi_{\text{ours}}$ , plotted as function of stellar mass. The SMFs predicted from the models are in general too steep, significantly over-predicting the number densities of galaxies below the characteristic stellar mass at all redshifts, and severely under-predicting the number density of the massive galaxies at  $z > 2.0$ . The good agreement at  $z = 0.1$  is the direct result of the optimization of the free parameters in the models to match the  $z = 0$  universe.

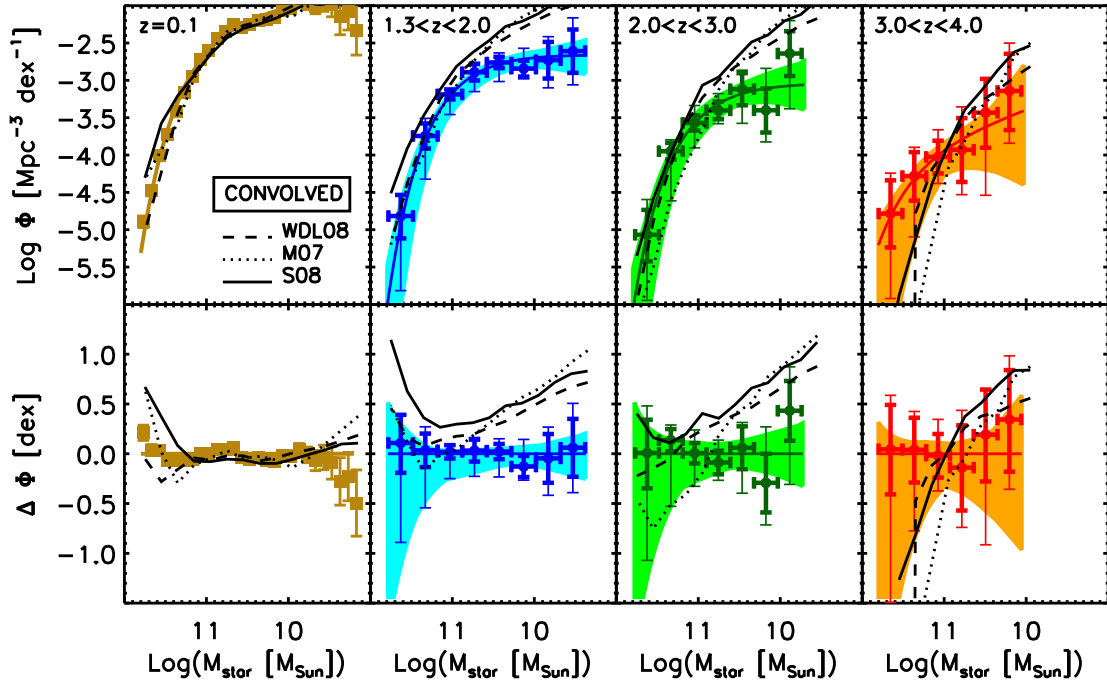


FIG. 14.— Same as in Fig. 13, except here the SMFs predicted by the semi-analytic models have been convolved with a normal distribution of standard deviation 0.25 dex; no convolution has been applied to the model-predict SMF at  $z = 0.1$ . While the discrepancies at the low-mass end are still present, the discrepancies at the high-mass end are significantly reduced.

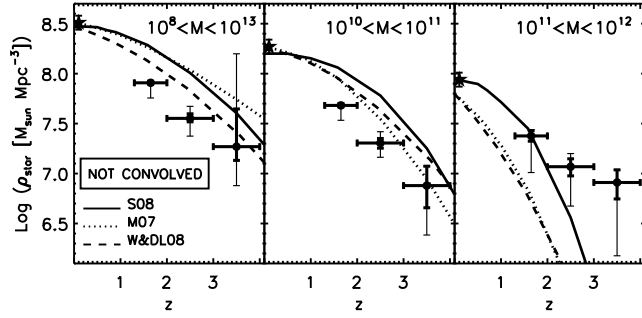


FIG. 15.— Comparison of the observed stellar mass densities with those predicted by the semi-analytic models as function of redshift, with no convolution with a normal distribution of standard deviation 0.25 dex applied to the model-predicted SMFs. Filled circles represent the observed stellar mass densities, while the curves are those predicted by the models. The left, middle, and right panels show the comparison between observations and model predictions for  $8 < M < 13$ ,  $10 < M < 11$ , and  $11 < M < 12$ , respectively. The thick error bars include Poisson errors, cosmic variance, and the uncertainties from photometric random errors; the thin error bars include the systematic uncertainties, with the exclusion of the effect due to the use of the bottom-light IMFs. The models fail in reproducing the observed evolution of the stellar mass density of low-mass galaxies ( $10^{10} < M_{\text{star}} = M < 10^{11}$ ), and severely under-predict the stellar mass density of massive galaxies ( $10^{11} < M_{\text{star}} = M < 10^{12}$ ).

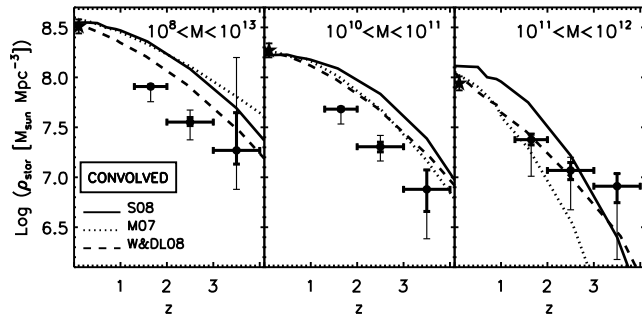


FIG. 16.— Same as Fig. 15, except here the predictions of the semi-analytic models are convolved with a normal distribution of standard deviation 0.25 dex. While all models fail in reproducing the observed evolution of the stellar mass density of low-mass galaxies ( $10^{10} < M_{\text{star}} = M < 10^{11}$ ), the disagreements between the observed and predicted stellar mass densities of massive galaxies are significantly reduced.

the stellar mass density of galaxies below the characteristic stellar mass ( $10^{10} < M_{\text{star}} = M < 10^{11}$ ). Over the entire redshift interval  $1.3 < z < 4.0$ , all models over-predict the observed stellar mass density of low-mass galaxies by a factor of a few, with the predictions from the Somerville et al. (2008) model showing the largest disagreements with the observations.

We conclude that the models succeed for some redshift and stellar mass ranges and fail for others, although this may partly be due to systematic errors in the observed SMFs and stellar mass densities (see § 5 and § 6). In general, the model-predicted SMFs are too steep compared to the observed SMFs, resulting in a significant over-prediction of the number densities of low-mass galaxies. Models also fail in predicting the observed number density of massive galaxies observed at  $3.0 < z < 4.0$ .

## 8. SUMMARY AND CONCLUSIONS

In this paper we have measured the stellar mass functions of galaxies at redshifts  $1.3 < z < 4.0$  from a composite  $K$ -selected sample constructed with the deep NIR MUSYC, the ultra-deep FIRES, and the GOODS-CDFS surveys, all having very high-quality optical-to-MIR data. This sample is unique

in that it combines data from surveys with a large range of depths and areas in a self-consistent way.

The total effective surveyed area of  $511 \text{ arcmin}^2$  over several independent field of views allowed us to minimize the uncertainties due to cosmic variance, and empirically quantify its contribution to the total error budget. Moreover, we were able to probe the high-mass end of the SMFs with unprecedented good statistics. The three adopted surveys allowed us to empirically derive the redshift-dependent completeness limits of the  $K$ -selected samples by exploiting their different depths. This is a significant improvement with respect to previous studies, since it does not rely on stellar population synthesis models to assess the completeness in stellar mass of the sample. Finally, the ultra-deep FIRES survey allowed us to probe the low-mass end of the SMF down to stellar masses as small as  $0.05$  times the characteristic stellar mass.

We provide, for the first time, a comprehensive analysis of all random and systematic uncertainties affecting the derived SMFs. We have quantified the uncertainties on the SMF due to photometric redshift random errors by repeating the full analysis on a set of 100 mock  $K$ -selected catalogs created by perturbing the observed photometry of each object according to its formal errors. Systematic uncertainties due to different sets of SED-modeling assumptions and different input parameters in the estimate of the photometric redshifts have also been quantified by changing IMF, metallicity, stellar population synthesis model, extinction curve in the SED-modeling, and template set and template error function in EAZY, the code used to estimate photometric redshifts.

We found that the stellar mass density evolves by a factor of  $17^{+7}_{-10}$  from  $z = 4.0$ , and a factor of  $4 \pm 0.2$  since  $z = 1.3$ . The observed evolution appears to be mostly driven by a change in the normalization  $^?$  of the SMF, rather than a change in the slope or the characteristic stellar mass  $M_{\text{star}}^?$ , especially since redshift  $z = 3.0$ . This is by itself a very interesting result, since it implies that the physical processes responsible in the building up of the stellar content of galaxies since  $z = 3.0$  do not change significantly the shape of the SMF (defined by  $^?$  and  $M_{\text{star}}^?$ ). The shape of the SMF is instead quite different at  $z \gtrsim 3.5$ , with a much steeper low-mass end slope. We note however that the SMF at  $3.0 < z < 4.0$  is quite uncertain. We also find evidence for mass-dependent evolution of the SMF of galaxies with redshift. Specifically, galaxies below the characteristic stellar mass show stronger evolution with cosmic time with respect to the galaxies at the high-mass end, with the most massive galaxies ( $M_{\text{star}} > 10^{11.5} M_{\odot}$ ) showing a remarkable lack of evolution.

If both random and systematic errors affecting the observed SMFs are taken into account, the previous results are no longer robust, and significant progress is required to better constrain the high-redshift SMFs. The observed absolute number of the most massive galaxies is very small, only a handful in each of the targeted redshift interval. Surveys with much larger area are needed in order to significantly improve the statistics on these rare objects. Cosmic variance, i.e., field-to-field variations, remains a significant source of uncertainty, especially at the high-mass end and at  $z < 2$ . Therefore, large surveys over multiple spatially disjoint fields are required to make significant progress in this respect. Last, but not least, most of the redshift information comes from photometric redshift estimates. At the very high-mass end, photometric redshift errors are a non-negligible source of errors, since the uncertainties will tend to scatter galaxies from the well-populated region around  $M_{\text{star}}^?$  toward the sparsely popu-

lated high-mass end. Redshift errors are a significant source of uncertainties also at the highest considered redshift intervals.

Obtaining large numbers of spectroscopic redshifts for  $K$ -selected high- $z$  sources has proven difficult and extremely time consuming, even for very bright galaxies (Kriek et al. 2008). Note also that the galaxies belonging to the high-mass end ( $M_{\text{star}} > 10^{11} M_{\odot}$ ) are generally very faint in the observed optical ( $R < 26$ ; van Dokkum et al. 2006), hence making optical spectroscopy completely unfeasible. Although the situation will be improved in the near future by the advent of multi-object NIR spectrographs, which will allow to construct large sample of high- $z$   $K$ -selected galaxies with spectroscopic redshift measurements, these projects will only probe the brightest population, leaving the high-mass end of the SMF still prone to photometric redshift uncertainties affecting the rest of the galaxy population.

The on-going NEWFIRM Medium-Band Survey (van Dokkum et al. 2009) will be able, upon completion, to improve on all of the above aspects. This deep and wide-field NAO/Jale survey uses the newly commissioned NEWFIRM instrument (mounted on the 4 m Mayall telescope) with custom-made medium band-width filters over the wavelength range 1–1.8  $\mu\text{m}$  to obtain well-sampled SEDs and high quality photometric redshifts for  $K_S^{\text{tot}} < 23.4$  galaxies. The full survey will provide accurate redshift measurements ( $z = (1+z) \pm 0.02$ ) for  $\sim 8000$  galaxies at  $1.5 < z < 3.5$  over a total area of  $\sim 0.5$  square degree in the COSMOS and AEGIS fields, allowing to drastically reduce the impact of random uncertainties and cosmic variance in the measurements of the high-redshift SMFs.

We also note that we cannot constrain the low-mass end of the SMFs very well at  $z > 2$ . If the SMF is much steeper at the low-mass end than indicated by our maximum-likelihood analysis, we could be missing a significant fraction of the integrated stellar mass (see Reddy & Steidel 2009). Reddy & Steidel (2009) suggest that up to  $\sim 50\%$  of the total stellar mass at  $1.9 < z < 3.4$  is in faint-UV galaxies with masses smaller than  $10^{10} M_{\odot}$  (compared to  $\sim 10\%$ – $20\%$  from an extrapolation of our Schechter fits). However, Reddy & Steidel (2009) do not measure stellar masses directly, but convert UV luminosity to stellar mass. Ultra-deep near-IR imaging can directly determine whether there is a large population of very low-mass galaxies at high redshift which contribute significantly to the total stellar mass density. Deep surveys with WFC3 on HST, as well as deep ground-based surveys such as the UKIDSS Ultra-Deep Survey (Lawrence et al. 2007) and the Ultra-VISTA survey<sup>18</sup>, will allow us to much better constrain the low-mass end of the SMFs.

Progress in observations have to be supported by significant progress in the theoretical arena. Systematic uncertainties due to different SED-modeling assumptions are a significant, if not dominant, contribution to the total error budget. Convergence on the stellar population synthesis models is of paramount importance not only to significantly decrease the systematic uncertainties on the derived SMF, but also to have a correct understanding of the properties of galaxies, such as age, star formation rate, etc. Understanding the IMF and its evolution as function of cosmic time is also extremely important, especially for studies at high-redshift. Significant work is however required theoretically to better understand what

physical parameter is most responsible in shaping the IMF and its evolution with cosmic time.

The observed SMFs have been compared with the SMFs predicted from the semi-analytic models of Monaco et al. (2007), Wang et al. (2008), and Somerville et al. (2008). The model-predicted SMFs are generally too steep with respect to the observed SMFs, resulting in significant over-prediction of the number densities of galaxies at the low mass end. While relatively good agreement is observed at the high-mass end at  $z \sim 2.5$ , some models tend to under-predict the observed number densities of massive galaxies at  $2.5 < z < 4.0$ . The discrepancy at the high-mass end is susceptible to uncertainties in the models and the data, but the discrepancy at the low-mass end may be more difficult to explain. These results are robust, even when all random and systematic uncertainties are included, suggesting that current models do not yet provide a complete description of galaxy formation and evolution since  $z = 4.0$ .

We are grateful to C. Maraston, for providing stellar population synthesis models with bottom-light IMFs; S. Charlot, for providing the unpublished CB08 stellar population synthesis models; R. Somerville and F. Fontanot for providing the predictions of the semi-analytic models used in this work and for helpful clarifications. We also thank G. Brammer for constant support with EAZY. We thank the anonymous referee for his/her detailed and insightful comments, which helped improve the paper. We thank all the members of the MUSYC collaboration for their contribution to this research. MUSYC has greatly benefited from the support of Fundación Andes and the Yale Astronomy Department. DM is supported by NASA LTSA NNG04GE12G. The authors acknowledge support from NSF CARRER AST-0449678.

<sup>18</sup> <http://www.eso.org/sci/observing/policies/PublicSurveys/sciencePublicSurveys.html>



TABLE A1  
CHARACTERISTICS OF THE IRAC OBSERVATIONS

Filter ( $\mu\text{m}$ )	Exposure Time (hr)	FWHM (arcsec)	Total Limiting Magnitude <sup>a</sup> (3 $\sigma$ , AB mag)	Positional Accuracy <sup>b</sup> (arcsec)	Galactic Extinction (mag)
SDSS-1030:					
3.6	1.0	1.4	24.53	0.07	0.005
4.5	1.0	1.4	24.14	0.08	0.004
5.8	1.0	1.7	22.35	0.07	0.004
8.0	1.0	2.0	22.16	0.08	0.003
CW-1255:					
3.6	1.0	1.5	24.74	0.05	0.003
4.5	1.0	1.4	24.37	0.07	0.003
5.8	1.0	1.8	22.52	0.05	0.002
8.0	1.0	2.1	22.45	0.07	0.002
HDFS-2:					
3.6	0.5	1.4	24.49	0.08	0.005
4.5	0.5	1.4	24.00	0.09	0.005
5.8	0.5	1.8	22.21	0.08	0.004
8.0	0.5	2.2	22.08	0.09	0.004
HDFS-1:					
3.6	0.3–4.2	1.7	24.41–25.06 <sup>c</sup>	0.06	0.005
4.5	0.3–4.2	1.7	24.12–24.83 <sup>c</sup>	0.07	0.005
5.8	0.3–4.2	2.2	22.39–23.36 <sup>c</sup>	0.06	0.004
8.0	0.3–4.2	2.1	22.35–23.24 <sup>c</sup>	0.07	0.004

<sup>a</sup>The total limiting magnitudes were estimated using the empty aperture method, corrected for the flux missed outside the  $3''$  aperture used for photometry. This correction is  $-0.18$  mag.

<sup>b</sup>The rms difference between bright star positions in IRAC and  $K$ -band image, after pointing refinement.

<sup>c</sup>The first number corresponds to the shallower area, while the second depth corresponds to the deeper area overlapping with the HDF-S Proper field.

## APPENDIX

### DATA REDUCTION AND PHOTOMETRY OF THE *SPITZER*-IRAC DATA IN MUSYC:

Here we describe the data taken with the Infrared Array Camera (IRAC; Fazio et al. 2004) on board *Spitzer* over the deep NIR MUSYC fields, their reduction, and the creation of  $K$ -selected catalogs with IRAC photometry. The  $K$ -selected catalogs with IRAC photometry included is publicly available at <http://www.astro.yale.edu/musyc>.

#### *Spitzer*-IRAC data

The IRAC data over the deep NIR MUSYC fields come from two different sources. Specifically, the IRAC data over the HDFS-2, the SDSS-1030, and the CW-1255 fields come from the Spitzer Space Telescope Cycle-3 program GO-30873 (P.I.: Labbé), while the IRAC data over the HDFS-1 field are part of the GTO-214 program (P.I.: Fazio). Table A1 summarizes the characteristics of the IRAC data over the deep MUSYC fields, such as the total exposure time, full-width half maximum (FWHM), limiting depth, positional accuracy, and Galactic extinction in each of the four IRAC bands. The total exposure times vary from 30 min for the HDFS-2 field, to 1 hr in the SDSS-1030 and CW-1255 fields across the entire  $10''-10''$  field. The exposure time across the HDFS-1 is instead not homogeneous, being  $\sim 4.2$  hrs in the small area overlapping with the HDF-S Proper field, and 20 min everywhere else. All fields were covered in all four IRAC channel, namely the 3.6, 4.5, 5.8, and 8.0  $\mu\text{m}$  bands.

#### Data reduction

The reduction started with the basic calibrated data (BCD) as provided by the Spitzer Science Center pipeline. We applied a series of procedures to reject cosmic rays and remove artifacts such as column pulldown, muxbleed, maxstripe, and the “first-frame effect” (Hora et al. 2004). Then, the single background-subtracted frames were combined into a mosaic image large enough to hold all input frames (using WCS astrometry to align the images). In this step, bad pixels were also masked, and distortion corrections applied in WCS. This image, in combination with the  $K$ -band reference image, was then used to refine the pointing of the individual mosaics (6 mosaics, in a  $2 \times 3$  grid). After pointing refinement, positional accuracy is  $0.05-0.09$  arcsec. We note that the source-fitting algorithm developed by I. Labbé et al. (in preparation) that we have used to derive the IRAC photometry takes care of residual shifts. Finally, the individual pointing-refined frames were registered to and projected on the public  $K$ -band images ( $0.27''$  pixel scale) of the four MUSYC fields (Quadri et al. 2007),<sup>19</sup> and average-combined. Flux conservation has been forced throughout the reduction.

#### Seeing, zero-points, and limiting depths

FWHM of the IRAC images were derived by taking the median of the FWHM for a set of  $\sim 15-30$  bright, isolated stars in the fields. The FWHM of each field and each IRAC band are listed in Table A1, and amount to  $1.4-1.7''$ ,  $1.4-1.7''$ ,  $1.7-2.2''$ , and  $2.0-2.2''$  for the 3.6, 4.5, 5.8, and 8.0  $\mu\text{m}$  bands, respectively.

<sup>19</sup> All optical and NIR data and the  $K$ -selected catalogs from the deep NIR MUSYC survey are publicly available from <http://www.astro.yale.edu/musyc>.

Following Quadri et al. (2007), the IRAC photometry in the  $K$ -selected catalogs are presented in units of flux, normalized so that the zero-points is 25 on the AB system. The use of flux, rather than magnitudes, avoids the problem of converting the measured flux uncertainties into magnitude uncertainties, the problem of asymmetric magnitude uncertainties for low S/N objects, and the loss of information for objects that have negative measured fluxes. Vega to AB magnitude conversions are 2.78, 3.26, 3.75, and 4.38 for the 3.6, 4.5, 5.8, and 8.0  $\mu$ m bands, respectively. We adopted the following transformation from Jy to Vega magnitudes:

$$m_{\text{Vega}} = -2.5 \log(\text{flux}[Jy]) + B; \quad (\text{A1})$$

with  $B = 6.12, 5.64, 5.15$ , and  $4.52$  for the 3.6, 4.5, 5.8, and 8.0  $\mu$ m bands, respectively. The IRAC zero-point uncertainties are of the order of 2% (Reach et al. 2005), which was included in the flux error budget.

The IRAC photometry has been corrected for Galactic extinction, using the extinctions listed in Table A1. These values, taken from the Galactic Dust Extinction Service (<http://irsa.ipac.caltech.edu/applications/DUST>), were derived using the data and technique of Schlegel et al. (1998).

The properties of the IRAC images were analyzed following the same approach as for the deep NIR MUSYC data (Quadri et al. 2007). Briefly, the technique uses aperture photometry distributed randomly over empty regions of the image to quantify the rms of background pixels within the considered aperture size. For a given aperture size, the distribution of empty aperture fluxes is well fitted by a Gaussian. The total limiting AB magnitudes ( $3\sigma$  for point sources, i.e., corrected for the flux missed outside the aperture used for photometry) are listed in Table A1.

### Photometry

A source-fitting algorithm developed by I. Labbé et al. (2008, in preparation), especially suited for heavily confused images for which a higher resolution prior (in this case the  $K$ -band image) is available, was used to extract the photometry from the IRAC images. A short description with illustration was also presented by Wuyts et al. (2007). Since this program does not take into account large-scale background variations, these were removed a priori from the IRAC images. Briefly, the information on position and extent of sources bases on the higher resolution  $K$ -band segmentation map was used to model the lower resolution IRAC  $3.6\text{--}8.0\ \mu\text{m}$  images. Each source was extracted separately from the  $K$ -band image and, under the assumption of negligible morphological  $k$ -corrections, convolved to the IRAC resolution using the local kernel coefficients. Convolution kernels were constructed using bright, isolated, unsaturated sources in the  $K$  and the IRAC bands (derived by fitting a series of Gaussian-weighted Hermite functions to the Fourier transform of the sources, rejecting outlying or poorly-fitting kernels), and a smoothed 2D map of the kernel coefficients was stored. A fit to the IRAC image was then made for all sources simultaneously, where the fluxes of the objects were left as free parameters. Next, we subtracted the modeled light of neighboring objects and measured the flux on the cleaned IRAC map within a fixed  $3''$  diameter aperture. Through a visual inspection of the IRAC residual image with all sources subtracted, we conclude that this method effectively removes contaminating sources (for an illustration of this technique, see also Figure 1 in Wuyts et al. 2007). In order to compute a consistent  $K$ –IRAC color, we measured the source’s flux  $f_{\text{conv},K}$  on a cleaned  $K$ -band image convolved to the IRAC resolution within the same aperture. We then scaled the photometry to the same color apertures that were used for the NIR photometry, allowing a straightforward computation of colors over  $U$ –to– $8\ \mu\text{m}$  wavelength baseline. For the IRAC photometry, this means that the catalog flux was computed as follows:

$$f_{\text{IRAC},\text{col}} = f_{\text{IRAC},\beta^{00}} \frac{f_{K,\text{col}}}{f_{\text{conv},K,\beta^{00}}}; \quad (\text{A2})$$

Note that the used source-fitting algorithm developed by I. Labbé et al. (in prep.) takes into account the spatial extent of the sources on the reference  $K$ -band image, and it does not adopt the best-fit flux from the source fitting as final photometry, but rather measures the flux within an aperture on the cleaned image (followed by an aperture correction). This allows more robust photometry in cases where the object profile varies from the reference to the low-resolution image. Uncertainties in the measured fluxes in the IRAC bands were derived as described in Wuyts et al. (2008), accounting for the background rms and residual contamination of the subtracted neighbors (I. Labbé et al. 2008, in prep.).

### ILLUSTRATION OF COMPLETENESS ESTIMATION: THE SDSS-1030 SAMPLE

We have used a different approach (described in § 4.1) to estimate the redshift-dependent completeness limit in stellar mass of our  $K$ -selected sample to be used to derive the SMFs of galaxies. In the following, we illustrate the estimation of the redshift-dependent completeness limit in stellar mass for the SDSS-1030 sample.

First, we selected galaxies belonging to the available deeper samples, namely the HDFS, the MS-1054, and the CDFS samples. Second, we scale their fluxes and stellar masses to match the SDSS-1030  $K$ -band 90% completeness limit. This is illustrated in Figure B1. In this figure, the colored filled symbols represent objects from the deeper samples (HDFS in blue, MS-1054 in red, and CDFS in orange) scaled up in flux to the SDSS-1030  $K$ -band 90% completeness limit. These objects represent objects immediately at our detection limit. The upper envelope of these points in the  $(M_{\text{star,scaled}} - z)$  space represents the most massive galaxies that might escape detection/selection in our analysis. Therefore, this upper envelope, encompassing 95% of the points, provides a redshift-dependent stellar mass completeness limit for the SDSS-1030 sample.

This suggests that at  $z \gtrsim 2.3$ , the SDSS-1030 sample is approximately complete for stellar masses  $M_{\text{star}} > 10^{11} M_{\odot}$ . In the same panel, we also compare the empirically-derived completeness limit (solid curve) with the completeness derived assuming an SSP with no dust formed at  $z = 10$  and scaled to match the SDSS-1030  $K$ -band 90% completeness limit (dashed curve). It is obvious from this comparison that, for SDSS-1030, the SSP-derived completeness is similar to the empirically-derived completeness only for  $z \gtrsim 2$ , while at  $z \lesssim 2$  the SSP-derived completeness implies a higher completeness in stellar mass than empirically derived. The difference between the empirically- and the SSP-derived completeness is a function of redshift, with the differences increasing

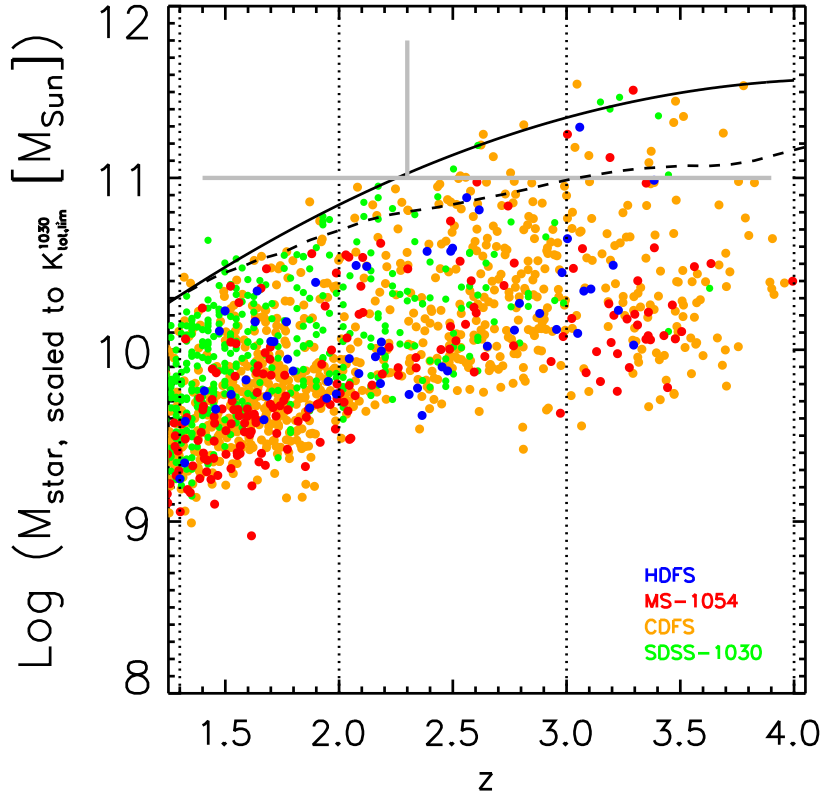


FIG. B1.— Empirically-determined completeness in stellar mass as a function of redshift; black filled circles represent the stellar masses for the SDSS-1030 galaxies scaled down in flux to match the SDSS-1030  $K$ -band 90% completeness limit, and plotted as a function of redshift. The other circles show the stellar masses for the CDFS (orange), the MS-1054 (red), and the HDFS (blue) galaxies scaled in flux to match the SDSS-1030  $K$ -band 90% completeness limit. The solid curve represents the upper envelope of these points (encompassing 95% of the points), and effectively defines, as a function of redshift, the limiting stellar mass corresponding to the observed flux limit of the SDSS-1030 sample. At  $z \approx 2.3$ , the SDSS-1030 sample is approximately complete for stellar masses  $M_{\text{star}} > 10^{11}$ . We emphasize that the stellar masses plotted here are not the actual stellar masses, but the stellar masses scaled to the  $K$ -band limit of the SDSS-1030 field.

going to higher redshift. This could be due, i.e., to the fact that dust extinction becomes progressively more important for galaxies in the high-mass end with increasing redshift.

#### COMPARISON WITH PREVIOUSLY PUBLISHED GALAXY STELLAR MASS FUNCTIONS:

Here we compare our results to previous studies on the SMFs of galaxies at  $z > 1$ . These works include the work of Drory et al. (2005), Fontana et al. (2006), Pozzetti et al. (2007), Elsner et al. (2008), and Pérez-González et al. (2008). None of these works have included a comprehensive analysis of the uncertainties (random and systematic) on the derived SMFs. As already pointed out, our work represents the first analysis of the SMFs at high-redshift with a comprehensive analysis of the errors. The statistically significant disagreements among the different works mostly stem from the lack of a complete analysis of the errors of the SMFs from the literature. Once a complete analysis of the errors is performed, as done for the first time in our work, the disagreements between the different measurements of the SMFs are no longer statistically significant.

Our  $K$ -selected composite sample is unique in that it combines very high-quality multi-waveband data from surveys with a large range of depths and areas in a self-consistent way. The available large number of single large area fields allows for the empirically estimate of the contribution of cosmic variance to the error budget, which is the dominant source of random errors in the lowest targeted redshift range and at the high-mass end. The combination of deep and ultra-deep samples allows us to empirically derive the completeness in stellar mass of the  $K$ -selected sample, without relying on stellar models, such as a passively evolving single stellar population formed at very high redshift ( $z \approx 10$ ) without any dust extinction (SSP-derived completeness), as done in most of the studies in the literature.

We therefore conclude that, with respect to the works in the literature, our SMFs are a significant improvement due to 1) the comprehensive analysis of the errors of the SMFs, both random and systematic (completely missing in the literature); 2) the large range in stellar masses probed by the composite  $K$ -selected sample, which allowed for better sampling of both the high- and the low-mass end; 3) the large surveyed area and the large number of independent fields, allowing for a decrease of the uncertainty due to cosmic variance (with respect to previous works) and to empirically quantify its contribution; 4) the availability of samples with different depths, allowing us to empirically derive, for the first time, the redshift-dependent completeness limits in stellar mass.

#### *Drory et al. (2005):*

Drory et al. (2005) derived the SMFs of galaxies from  $z = 0.25$  to  $z = 5$  from two different samples: an  $I$ -selected sample over 40 arcmin<sup>2</sup> of the FORS Deep Field (FDF; Heidt et al. 2003) with  $UBgRIzJK$  coverage, consisting of 5557 galaxies down to

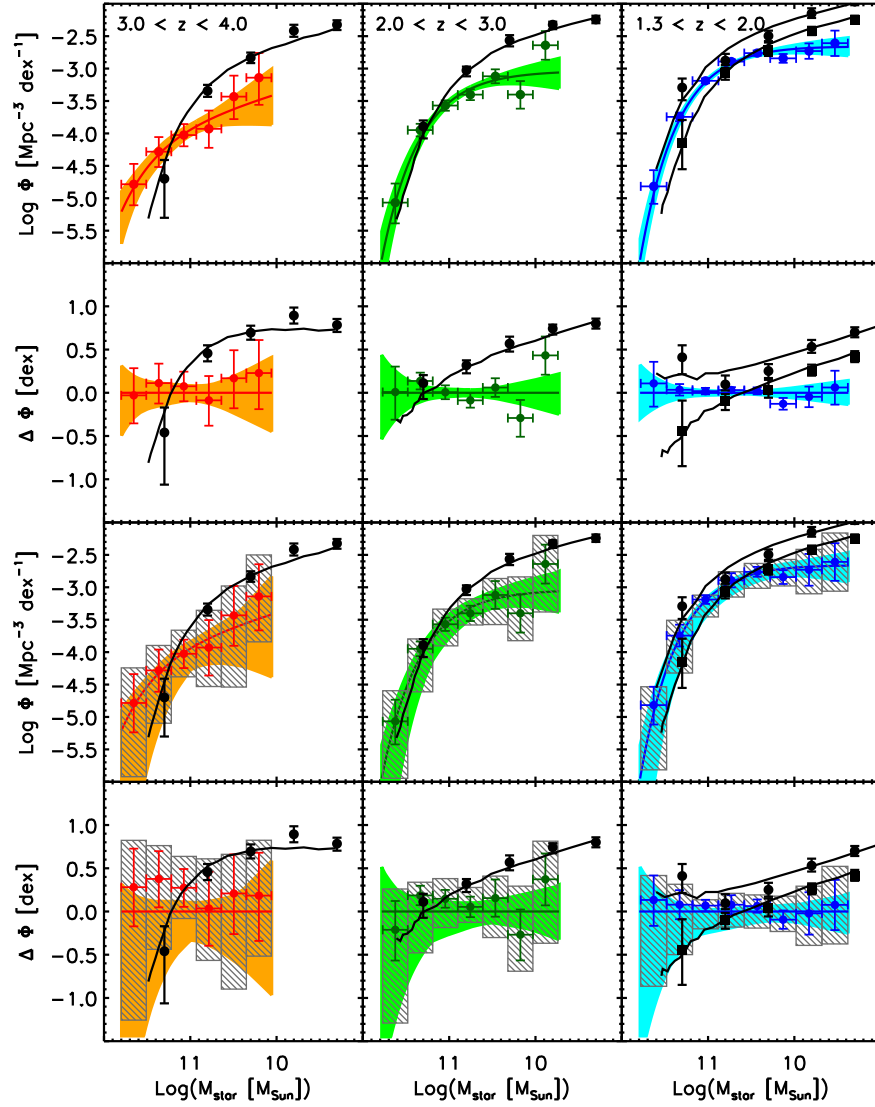


FIG. C1.— Comparison between the SMFs from Drory et al. (2005) and from this work at  $3.0 < z < 4.0$  (left),  $2.0 < z < 3.0$  (middle), and  $1.3 < z < 2.0$  (right). Symbols as in Fig. 11, except black filled symbols and black curves representing the SMFs derived in Drory et al. (2005). The SMFs of Drory et al. (2005) have been scaled by -0.2 dex along the x-axis to take into account difference in the adopted IMF. Note that the SMFs from Drory et al. (2005) are actually derived in the following redshift intervals:  $3.00 < z < 4.00$  (left panels),  $2.25 < z < 3.00$  (middle panels),  $1.25 < z < 1.75$  and  $1.75 < z < 2.25$  (right panels; filled black circles and squares, respectively).

$I = 26.8$  (50% completeness); and a  $K$ -selected sample over  $50 \text{ arcmin}^2$  in the GOODS-CDFS field with UBVRIJHK coverage. No mid-IR IRAC photometry was used. The quoted photometric redshift accuracy in  $z = (1 + z_{\text{spec}})$  is  $0.03$ . The stellar masses were derived by fitting the observed SEDs with a model grid of BC03 models. The star-formation history (SFH) was parameterized by a two-component model, with a main component with a smooth SFH modulated by a burst of star formation. The main component is parameterized by an exponentially declining SFH with an e-folding timescale  $\tau = [0.1; 1] \text{ Gyr}$ , and a metallicity of  $-0.6 < [Fe/H] < 0.3$ . The age was allowed to vary between 0.5 Gyr and the age of the universe at the object's redshift. This component was linearly combined with a burst modeled as a 100 Myr old CSF rate episode of solar metallicity, restricting the burst fraction  $0 < f < 0.15$  in mass. A Salpeter (1955) IMF truncated at 0.1 and 100  $M_{\odot}$  was adopted for both components. Finally, both components are allowed to exhibit a different and variable amount of extinction by dust. SMFs were derived with the  $1=V_{\text{max}}$  method, although it is unclear how the completeness is stellar mass as a function of redshift was derived. The Schechter function parameters were derived by fitting the  $1=V_{\text{max}}$  points with a Schechter function.

Their surveyed area is  $\sim 6.5$  times smaller than the surveyed area of our work, making their derived SMFs very much affected by cosmic variance. A direct comparison between the SMFs of Drory et al. (2005) and the SMFs measured in our work is shown in Figure C1. Note that the redshifts bins used in Drory et al. (2005) are not exactly the same as used in the present work.

The top panels of Figure C1 show the SMFs derived in our work without the inclusion of cosmic variance and systematic uncertainties in the plotted error bars; error bars include Poisson errors and photometric redshift random errors. The errors of the Drory et al. (2005) SMFs only include random uncertainties. From the top panels of Figure C1, the SMFs from Drory et al. (2005) are consistent with those derived in our work only at the high-mass end, while their number densities are significantly higher at the low-mass end. The slopes of the SMFs at the low-mass end are steeper than those derived in our work, especially at  $z = 1.6$ . In the highest redshift range, where Poisson statistics dominates the error budget, the two SMFs are consistent within

2 in the overlapping stellar mass regime.

The SMFs of Drory et al. (2005) become fully consistent with ours at the high-mass end once all sources of errors are included in the error budget (bottom panels of Figure C1). However, the discrepancy at the low-mass end is still present and significant. The much higher densities derived by Drory et al. (2005) at the low-mass end (hence, the steeper slope) are very likely caused by the use of the  $1=V_{\max}$  method in combination with an inappropriate redshift-dependent completeness in stellar mass. While it is unclear how the completeness in stellar mass has been derived in Drory et al. (2005), we notice that, if an SSP-derived completeness were to be adopted in place of the empirically-derived completeness, steeper densities at the low-mass end would be derived, due to the more conservative completeness of the former with respect to the latter. We therefore believe that the SMFs of Drory et al. (2005) at the low-mass end are systematically too large, perhaps due to the use of incorrect redshift-dependent completeness limits in stellar mass.

*Fontana et al. (2006):*

Fontana et al. (2006) derived the SMFs of galaxies at  $0.4 < z < 4.0$  from the GOODS-MUSIC sample (Grazian et al. 2006). Their final  $K$ -selected sample consists of 2931 galaxies (1762 with  $H$ -band coverage) complete down to  $K_s = 23.5$ , over an area of  $143.2 \text{ arcmin}^2$  with  $UB_{435}V_{606}i_{775}z_{850}JHK$  and IRAC bands coverage. Note that this dataset make use of the same public data of the FIREWORKS-CDFS dataset (Wuyts et al. 2008) that we have used in our work, but without the inclusion of the WFI  $BVRI$  band data. Consequently, the SEDs of sources in the FIREWORKS-CDFS catalog are better sampled. We also note that (Wuyts et al. 2008) pointed out a systematic offset in the IRAC fluxes of the GOODS-MUSIC catalog with respect to the IRAC fluxes of the FIREWORKS-CDFS catalog, with the former averagely fainter than the latter by  $\sim 30\%$ . The observed offset in the IRAC photometry was largely attributed to the use of an early version of the IRAC PSF by Grazian et al. (2006) and a bug in the normalization of the smoothing kernel for the IRAC data by Grazian et al. (2006) (see Wuyts et al. 2008 for details).

Stellar masses were derived by fitting the observed SEDs with a set of templates computed with the BC03 spectral synthesis models. A Salpeter (1955) IMF was adopted with various metallicities (from  $Z = 0.02 Z_\odot$  to  $Z = 2.5 Z_\odot$ ), dust extinction ( $0 < E(B-V) < 1.1$ ) with a Calzetti et al. (2000) extinction curve, and e-folding timescales ( $\sim 2 [0.1; 15]$  Gyr) in an exponentially declining SFH.

SMFs were derived with the standard  $1=V_{\max}$  formalism and the maximum-likelihood analysis assuming a Schechter function with Schechter parameters  $\phi$ ,  $M_{\text{star}}^*$ , and  $\alpha$  evolving with redshift (for a total of seven free parameters, three of which constrained by the local SMFs derived in Cole et al. 2001). A treatment has been included to correct for the incompleteness in mass at the faintest levels (see Fontana et al. 2004 for details). Briefly, they start from the threshold computed from a passively evolving system (SSP-derived completeness limit), below which only a fraction of objects of given mass will be observed. Then, at any redshift, the observed distribution of  $M=L$  was obtained for objects close to the magnitude limit of the sample. Using this distribution, the fraction of lost galaxies as function of redshift and mass was computed. The correction is finally applied to the volume element  $V_{\max}$  of any galaxy in the  $1=V_{\max}$  binned SMFs as well as in the number of detected galaxies entering the maximum-likelihood analysis. We note that this method assumes that the sample is complete for objects with stellar masses larger than the SSP-derived limit. This assumption is not necessarily valid at all redshifts, and depends on the specific depth of the sample (see the right panel of Figure 3). Moreover, their correction for incompleteness also assumes that the distribution of  $M=L$  ratio is independent of  $L$ . As shown in the left panel of Figure 3, this assumption might not be valid at all redshift, depending on the specific depth of the sample. In fact, at faint luminosities, the distribution of  $M=L$  is visibly different from that at the bright end. While it is hard to predict the differences on the low-mass end of the SMFs derived with their method with respect to the method used in our work (empirically-derived completeness limit), we notice that their correction has been applied only for sources for which the correction factor is smaller than 0.5 (usually affecting only the last  $1=V_{\max}$  point). Moreover, as shown in the right panel of Figure 3, the SSP-derived completeness limit of the CDFS sample is quite similar to the empirically-derived completeness limit. Therefore, we do not expect large differences in the derived SMFs at the low-mass end, except for the lowest stellar mass bins.

A direct comparison between the SMFs of Fontana et al. (2006) and the SMFs measured in this work is shown in Figure C2. Again, top panels do not show the contribution of cosmic variance and systematic uncertainties in our SMFs, while they are included in the bottom panels of Figure C2. Error bars in the SMFs of Fontana et al. (2006) include Poisson errors and photometric redshift uncertainties, but no cosmic variance nor systematic uncertainties due to different SED-modeling assumptions. Note that the area surveyed in the GOODS-MUSIC sample is a factor of  $\sim 4$  smaller than the surveyed area in our work, and it consists of a single pointing, making their SMFs significantly affected by cosmic variance.

First of, as shown in the top panels of Fig. C2, the SMFs estimated from the  $1=V_{\max}$  method are broadly consistent within the errors. There appears to be a systematic offset, such that the SMFs of Fontana et al. (2006) are systematically shifted to lower masses. Although it is not simple to fully understand the origin of this difference, it could partly be due to the found systematic offset in the IRAC photometry. The SMFs derived using the maximum-likelihood analysis show a larger degree of disagreement, especially in the high-mass end at  $z \sim 3.5$ . We stress once again that cosmic variance is a dominant source of uncertainty in the SMFs of Fontana et al. (2006) since they are derived from a single, relatively small field. The found differences at the bright end can well be accounted for by field-to-field variations.

From the bottom panels of Figure C2, it is obvious that the SMFs of Fontana et al. (2006) are fully consistent with ours once all the source of uncertainties are taken into account, including the systematic effects due to different SED-modeling assumptions.

*Pozzetti et al. (2007):*

Pozzetti et al. (2007) derived the SMFs of galaxies from  $z = 0.05$  to  $z = 2.5$  from the  $K$ -selected sample of the VIMOS-VLT Deep Survey (VVDS; Le Fèvre et al. 2005) 02h field. Their  $K$ -selected sample consists of a shallow and a deeper component.



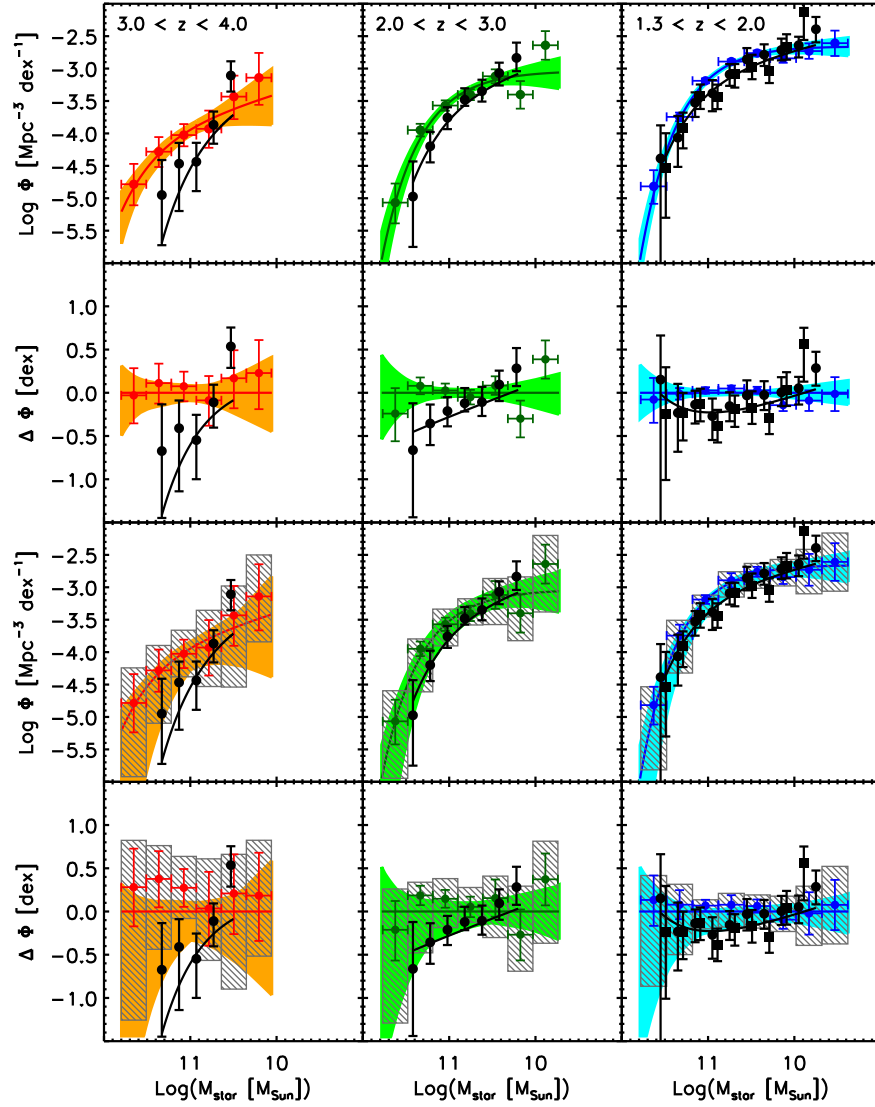


FIG. C2.— Comparison between the SMFs from Fontana et al. (2006) and from this work at  $3.0 < z < 4.0$  (left),  $2.0 < z < 3.0$  (middle), and  $1.3 < z < 2.0$  (right). Symbols as in Fig. C1. The SMFs of Fontana et al. (2006) have been scaled by  $-0.2$  dex along the  $x$ -axis to take into account difference in the adopted IMF. Note that the SMFs from Fontana et al. (2006) are actually derived in the following redshift intervals:  $3.0 < z < 4.0$  (left panels),  $2.0 < z < 3.0$  (middle panels),  $1.3 < z < 1.6$  and  $1.6 < z < 2.0$  (right panels; filled black circles and squares, respectively).

The shallow component consists of 6720 galaxies at  $0 < z < 2.5$  down to  $K = 22.34$  (90% complete) over  $442 \text{ arcmin}^2$ , while the deeper component is made of 3440 galaxies down to  $K = 22.84$  (90% complete) over  $172 \text{ arcmin}^2$ . About 15% of the galaxies have secure spectroscopic identification. The waveband coverage consists of  $UBVRiugrizJK$ , but no IRAC coverage (note that only  $170 \text{ arcmin}^2$  have deep  $J$  and  $K$  coverage; Iovino et al. 2005). Therefore, their surveyed area is  $\sim 3$  times smaller than the area surveyed in our work down to the same  $K$ -band limit of  $K = 22.8$ .

The stellar masses were derived by fitting the observed SEDs with a model grid of BC03 models. The star-formation history (SFH) was parameterized with an exponentially declining SFH with an e-folding timescale  $\sim 2 [0.1; 1] \text{ Gyr}$ , and solar metallicity. The age was allowed to vary between 0.1 Gyr and the age of the universe at the object's redshift. A Chabrier (2003) IMF was adopted, and extinction modeled using the Calzetti et al. (2000) curve with  $A_V \sim 2 [0.2; 4]$ .

SMFs were derived with the standard  $1=V_{\text{max}}$  formalism and the maximum-likelihood analysis assuming a Schechter (1976) function. While Pozzetti et al. (2007) stress the importance of using only galaxies with stellar masses above the stellar mass limit where all the SEDs are potentially observable (very restrictive limit), they ended up using as a lower limit of the mass range the minimum mass above which late-type SEDs are potentially observable. Therefore, we caution about potential biases in the estimate of the low-mass end of their SMFs.

A direct comparison between the SMFs of Pozzetti et al. (2007) and the SMFs measured in our work is shown in Figure C3. Note that the redshift bins used in Pozzetti et al. (2007) are not exactly the same as used in the present work. The SMFs derived in our work are shown in the left panel without the contribution of cosmic variance and the systematic uncertainties, and in the right panel with all errors included.

As shown in the left panel of Figure C3, the SMF from Pozzetti et al. (2007) at  $1.6 < z < 2.5$  is perfectly consistent with ours. On the contrary, their SMF at  $1.2 < z < 1.6$  is significantly different at the high-mass end. If the two SMFs at  $1.2 < z < 1.6$  and  $1.6 < z < 2.5$  are averaged, the obtained SMF is in very good agreement with the SMF derived in our work, except at the very

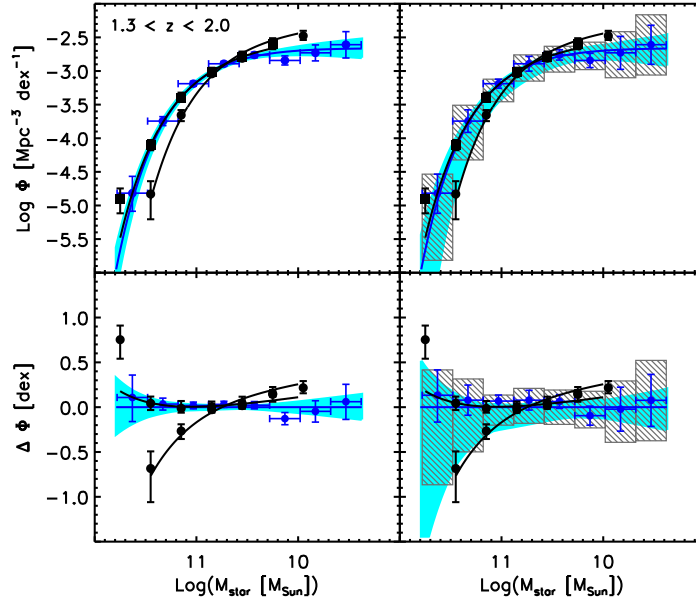


FIG. C3.— Comparison between the SMFs from Pozzetti et al. (2007) and from this work at  $1.3 < z < 2.0$ . Symbols as in Fig. C1. Note that the SMFs from Pozzetti et al. (2007) are actually derived at  $1.2 < z < 1.6$  (filled black squares) and  $1.6 < z < 2.5$  (filled black circles).

low-mass end. We note that the low-mass end becomes consistent within the errors when the systematic uncertainties are taken into account in the total error budget, highlighting once again the importance of a comprehensive analysis of the errors. Overall, the agreement between the SMF of Pozzetti et al. (2007) and ours is very good.

#### *Elsner et al. (2008):*

Elsner et al. (2008) have derived SMFs of galaxies from  $z = 5.0$  to  $z = 0.25$  from the GOODS-MUSIC  $z + K$ -selected catalog of Grazian et al. (2006), the same used in Fontana et al. (2006). The catalog used in Elsner et al. (2008) is to first order  $z_{850}$ -band selected sample, with the addition of the remaining  $K$ -band sources that are undetected in the  $z_{850}$ -band, making it less trivial to understand the completeness of the sample, especially in stellar mass. This sample comprises 14800 galaxies down to  $z_{\text{lim}} = 26.0$  (90% completeness level) over a total area of 143.2 arcmin<sup>2</sup>.

The stellar masses were derived by fitting the observed SEDs with a model grid of BC03 models. The star-formation history (SFH) was parameterized with an exponentially declining SFH with an e-folding timescale  $\tau = [0.5; 20]$  Gyr, and solar metallicity. The age was allowed to vary between 0.2 Gyr and the age of the universe at the object's redshift. A Salpeter (1955) IMF truncated at 0.1 and 100  $M_{\odot}$  was adopted. Dust extinction was modeled using the Calzetti et al. (2000) curve with  $A_V = [0; 1.5]$ . In addition to this main component, a starburst was superimposed which was allowed to contributed at most 20% to the  $z$ -band luminosity in the rest-frame. This component was modeled as a 50 Myr old episode of constant star formation with an independent extinction up to  $A_V = 2.0$  mag.

SMFs were derived with the  $1=V_{\text{max}}$  method after correcting the data points for incompleteness due to the flux-limited sample. The completeness limit in stellar mass was estimated by scaling the  $z$ -band completeness limit by the calculated 95% quantile in  $M=L_z$  as a function of redshift, e.g. the limit below which 95% of the  $M=L_z$  ratios of the sample are located. The Schechter function parameters were then derived by fitting the  $1=V_{\text{max}}$  points with a Schechter function after fixing the low-mass end slope at its error-weighted mean value.

A direct comparison between the SMFs of Elsner et al. (2008) and the SMFs measured in our work is shown in Figure C4. Note that the redshifts bins used in Elsner et al. (2008) are not exactly the same as used in the present work.

The SMFs estimated from Elsner et al. (2008) are in general good agreement with the SMFs measured in our work, especially at  $z = 3.5$  and  $z = 2.5$ . At the lower targeted redshift interval ( $1.3 < z < 2.0$ ), the SMF of Elsner et al. (2008) shows a higher number density for the most massive galaxies with respect to our measurements. We note however that the sample of Elsner et al. (2008) is constructed from the single, relatively small GOODS field ( $\sim 4$  times smaller than the area surveyed in our work). Therefore, the SMFs derived by Elsner et al. (2008) are significantly affected by field-to-field variations, especially at low redshift and at the high-mass end. Note that the error bars in the SMFs of Elsner et al. (2008) do not include the error due to cosmic variance, which we have shown being the dominant contribution to the total random error budget at  $z \gtrsim 2$ . We therefore conclude that the SMFs of Elsner et al. (2008) are fully consistent with our measurements, and that the disagreements at the high-mass end can be fully accounted by field-to-field variations.

We finally note the large significant discrepancies between the SMFs derived from Elsner et al. (2008) and from Fontana et al. (2006). The used catalog is exactly the same, i.e., the GOODS-MUSIC catalog. The differences are in the way the stellar mass completeness limits are estimated (affecting the low-mass end of the SMF) and in the assumptions of the SED-modeling. Specifically, the metallicity in Elsner et al. (2008) is fixed to solar, while it is left as a free parameter in Fontana et al. (2006). Also, larger  $A_V$  are allowed in Fontana et al. (2006), as well as no secondary starburst component added, contrary to what done in Elsner et al. (2008). The SMFs from Fontana et al. (2006) are systematically lower at similar stellar mass, particularly at  $z = 3.5$  and at the high-mass end. While the differences are statistically significant, as already pointed out by Elsner et al. (2008), they

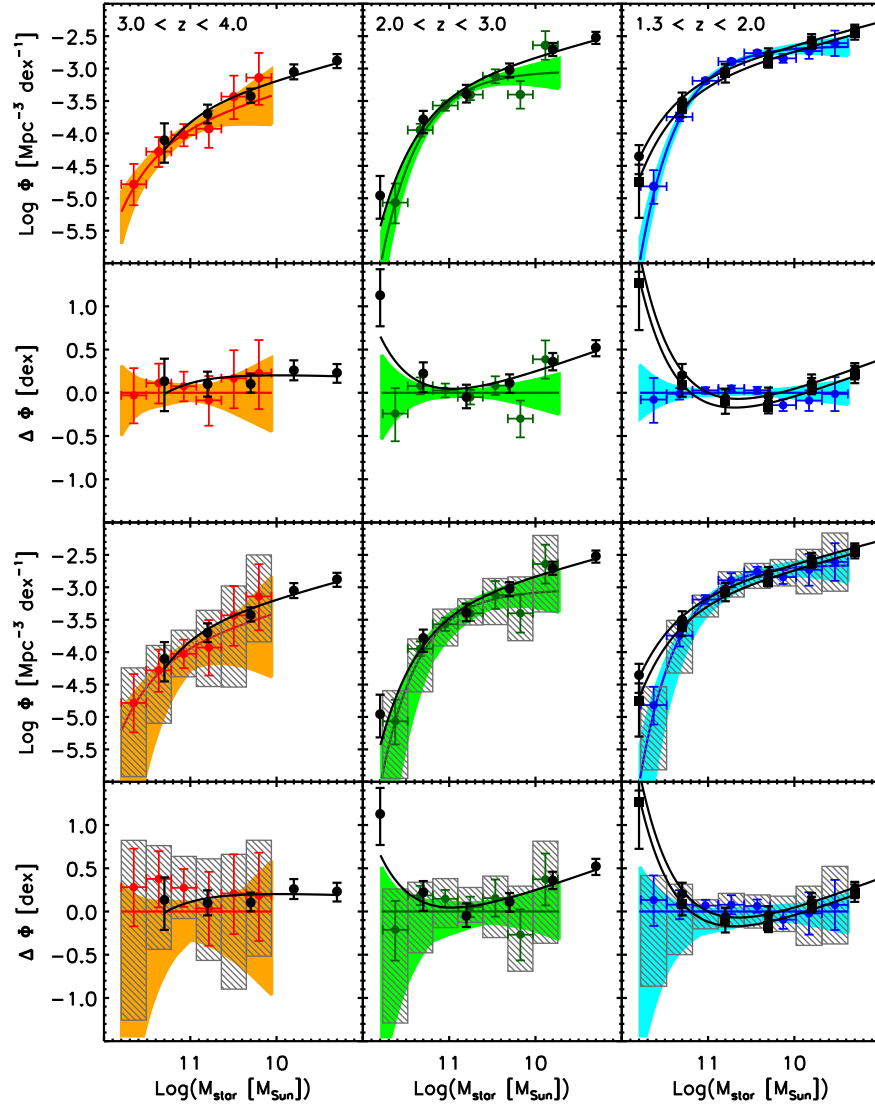


FIG. C4.— Comparison between the SMFs from Elsner et al. (2008) and from this work at  $3.0 < z < 4.0$  (left),  $2.0 < z < 3.0$  (middle), and  $1.3 < z < 2.0$  (right). Symbols as in Fig. C1. The SMFs of Elsner et al. (2008) have been scaled by -0.2 dex along the x-axis to take into account difference in the adopted IMF. Note that the SMFs from Elsner et al. (2008) are actually derived at  $3.01 < z < 4.01$  (left panels),  $2.25 < z < 3.01$  (middle panels),  $1.25 < z < 1.75$  and  $1.75 < z < 2.25$  (right panels; filled black circles and squares, respectively).

can be due to the different choices of SED-modeling assumptions, stressing the importance of a comprehensive analysis of the errors, both random and systematics.

*Pérez-González et al. (2008):*

Pérez-González et al. (2008) derived the SMFs of galaxies from  $z=0$  to  $z=4$  from a  $3.6\ \mu\text{m}$  and  $4.5\ \mu\text{m}$  *Spitzer*-IRAC selected sample. Their sample consists of 19400 sources down to the 75% completeness limit ( $\sim 23.3$  mag at  $3.6\ \mu\text{m}$ ) over three fields, namely the HDF-N, the CDF-S, and the Lockman Hole fields, for a total surveyed area of  $664\ \text{arcmin}^2$ , a factor of 1.14 larger than the total area surveyed by the sample used in the present work ( $\sim 583\ \text{arcmin}^2$ ). Their 90% completeness levels are in the range 22.0-22.4 mag at  $3.6\ \mu\text{m}$  and  $4.5\ \mu\text{m}$ , about a magnitude shallower than the 75% completeness levels.

The stellar masses were derived by fitting the observed SEDs with a grid of models created with the PEGASE code (Fioc & Rocca-Volmerange 1997). The star-formation history (SFH) was parameterized with an exponentially declining SFH with an e-folding timescale  $\sim 2\ [0.001; 100]$  Gyr, with allowed ages from 1 Myr to the age of the universe at the object's redshift. Seven discrete values of the metallicity were used, from  $Z = 0.005\ Z_\odot$  to  $Z = 5.0\ Z_\odot$ . A Salpeter (1955) IMF truncated at 0.1 and 100  $M_\odot$  was adopted. Dust extinction was modeled using the Calzetti et al. (2000) curve with  $A_V \sim 2\ [0; 5]$ . While other SED-modeling assumptions were used to test how the stellar masses changed by changing IMF, extinction curve, stellar population synthesis model, and star formation history, the systematic effects of these changes on the derived SMFs were not explicitly quantified nor discussed in Pérez-González et al. (2008).

SMFs were derived by integrating the bivariate luminosity-stellar mass function (the estimation of which was performed with a stepwise maximum likelihood technique) over all luminosities. The resulting SMFs were then fitted with a Schechter (1976) function. The low-mass end of the SMF at  $z > 1.6$  was constrained by combining their results with other estimates of the SMFs from the literature. The redshift-dependent completeness limit were derived assuming to be complete for stellar masses larger

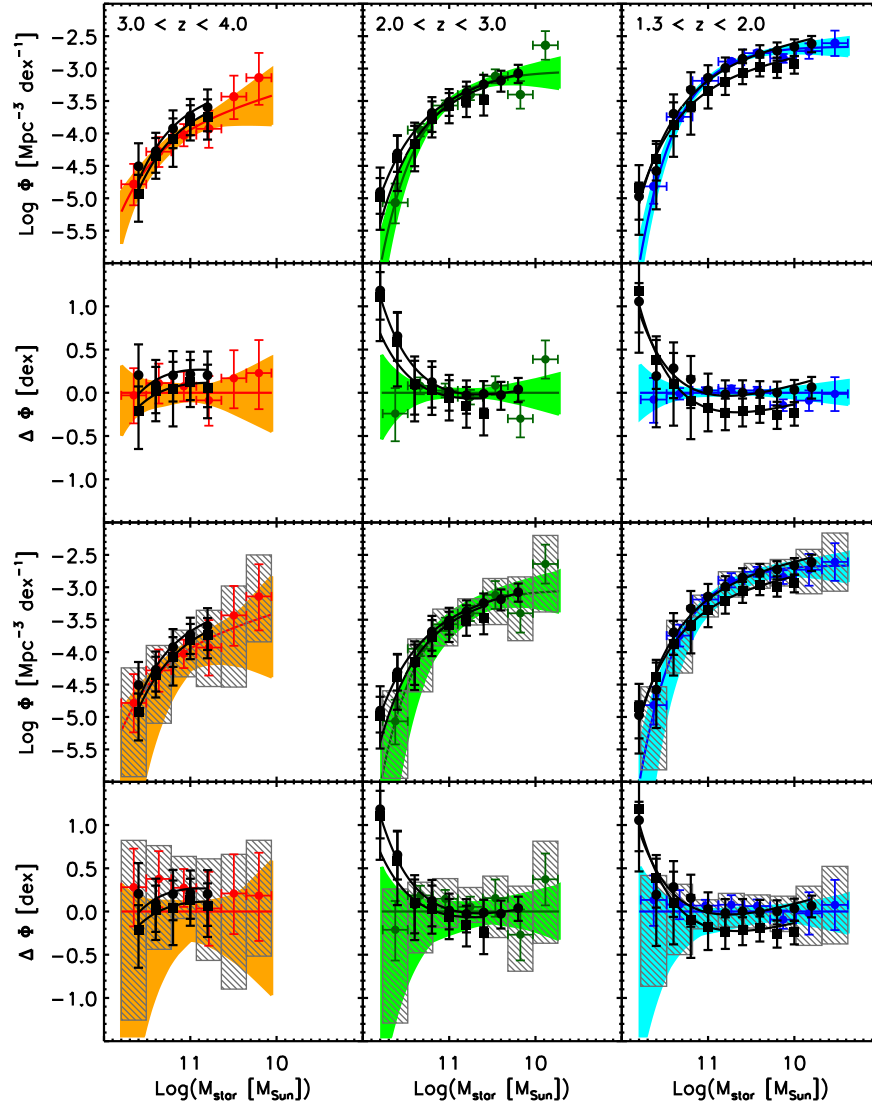


FIG. C5.— Comparison between the SMFs from Pérez-González et al. (2008) and from this work at  $3.0 < z < 4.0$  (left panels),  $2.0 < z < 3.0$  (middle panels), and  $1.3 < z < 2.0$  (right panels). Symbols as in Fig. C1. The SMFs of Pérez-González et al. (2008) have been scaled by -0.2 dex along the x-axis to take into account difference in the adopted IMF. Note that the SMFs from Pérez-González et al. (2008) are actually derived at  $3.0 < z < 3.5$  and  $3.5 < z < 4.0$  (left panels; filled black circles and squares, respectively);  $2.0 < z < 2.5$  and  $2.5 < z < 3.0$  (middle panels; filled black circles and squares, respectively);  $1.3 < z < 1.5$  and  $1.5 < z < 2.0$  (right panels; filled black circles and squares, respectively).

than the stellar mass corresponding to a passively evolving stellar population formed at  $z = 1$  with no extinction and having a 3.6  $\mu$ m flux equal to the 75% completeness level of the IRAC sample. Only galaxies with stellar masses larger than this completeness level were used in their analysis, and no completeness correction was carried out to recover the SMF at smaller masses.

A direct comparison between the SMFs of Pérez-González et al. (2008) and the SMFs measured in our work is shown in Fig. C5. Note that the redshifts bins used in Pérez-González et al. (2008) are smaller than the redshift intervals used in our work, i.e., our redshift intervals are further split in two in Pérez-González et al. (2008).

As shown in Fig. C5, the SMFs from Pérez-González et al. (2008) are generally in good agreement with the SMFs derived in our work, at all redshifts, especially at the low-mass end. Only at the very high-mass end in the redshift ranges  $2.0 < z < 3.0$  and  $1.3 < z < 2.0$ , the number densities derived from Pérez-González et al. (2008) look slightly larger than those derived in our work. These differences are only barely significant, and are definitely not statistically significant at all once cosmic variance and systematic uncertainties are included in the total error budget. We therefore conclude that the SMFs derived from Pérez-González et al. (2008) are in good agreement with the SMFs derived in our work, with the latter better sampling the low-mass end of the SMFs by 0.3–0.6 dex in stellar mass.

#### REFERENCES

- Allen, C. W. 1976, *Astrophysical Quantities*. University of London, The Athlone Press, 264
- Arnouts, S., Cristiani, S., Moscardini, L., Matarrese, S., Lucchin, F., Fontana, A., Giallongo, E. 1999, *MNRAS*, 310, 540
- Avni, Y., & Bahcall, J. N. 1980, *ApJ*, 235, 694
- Baugh, C. M., 2006, *RPPh*, 69, 3101
- Bell, E. F., McIntosh, D. H., Katz, N., & Weinberg, M. D. 2003, *ApJS*, 133149, 289

- Benitez, N. 2000, *ApJ*, 536, 571
- Blain, A. W., Jameson, A., Smail, I., Longair, M. S., Kneib, J.-P., & Ivison, R. J. 1999, *MNRAS*, 309, 715
- Blain, A. W., Jameson, A., Smail, I., Longair, M. S., Kneib, J.-P., & Ivison, R. J. 1999, *MNRAS*, 309, 715
- Blain, A. W., Smail, I., Ivison, R. J., & Kneib, J.-P. 1999, *MNRAS*, 302, 632
- Blanton, M. R., & Roweis, S. 2007, *AJ*, 133, 734
- Bolzonella, M., Miralles, J.-M., Pelló, R. 2000, *A&A*, 363, 476
- Borch, A., et al. 2006, *A&A*, 453, 869
- Bouchet, P., Lequeux, J., Maurice, E., Prévot-Burnichon, M. L. 1985, *A&A*, 149, 330
- Brammer, G. B., van Dokkum, P. G., & Coppi, P. 2008, *ApJ*, 686, 1503
- Bruzual, G., & Charlot, S. 2003, *MNRAS*, 344, 1000
- Bruzual, G. 2007, in Vazdekis A., Peletier R. F., eds, *IAU Symp. Vol. 241, On TP-AGB Stars and the Mass of Galaxies*. Cambridge Univ. Press, Cambridge, p. 125
- Bundy, K., et al. 2006, *ApJ*, 651, 120
- Cassisi, S., Castellani, M., & Castellani, V. 1997, *A&A*, 317, 108
- Chabrier, G. 2003, *PASP*, 115, 763
- Charlot, S., & Bruzual, G. 2008, in preparation
- Calzetti, D., Armus, L., Bohlin, R. C., Kinney, A. L., Koornneef, J., & Storchi-Bergmann, T. 2000, *ApJ*, 533, 682
- Cole, S., et al. 2001, *MNRAS*, 326, 255
- Coleman, G. D., Wu, C.-C., Weedman, D. W. 1980, *ApJS*, 43, 393
- Conselice, C. J., Blackburne, J. A., & Papovich, C. 2005, *ApJ*, 620, 564
- Daddi, E., et al. 2007, *ApJ*, 670, 173
- Davé, R. 2008, *MNRAS*, 385, 147
- De Lucia, G., Kauffmann, G., & White, S. D. M. 2004, *MNRAS*, 349, 1101
- De Lucia, G., & Blaizot, J. 2007, *MNRAS*, 375, 2
- Dickinson, M., Papovich, C., Ferguson, H. C., & Budavári, T. 2003, *ApJ*, 587, 25
- Drory, N., Bender, R., Feulner, G., Hopp, U., Maraston, C., Snigula, J., & Hill, G. J. 2004, *ApJ*, 608, 742
- Drory, N., Salvato, M., Gabasch, A., Bender, R., Hopp, U., Feulner, G., & Pannella, M. 2005, *ApJ*, 619, L111
- Efstathiou, G., Ellis R. S., & Peterson, B. A. 1988, *MNRAS*, 232, 431
- Elsner, F., Feulner, G., & Hopp, U. 2008, *A&A*, 477, 503
- Fagotto, F., Bressan, A., Bertelli, G., & Chiosi, C. 1994, *A&AS*, 104, 365
- Fazio, G. G., et al. 2004, *ApJS*, 154, 10
- Fioc, M., & Rocca-Volmerange, B. 1997, *A&A*, 326, 950
- Fontana, A., et al. 2003, *A&A*, 594, L9
- Fontana, A., et al. 2004, *A&A*, 424, 23
- Fontana, A., et al. 2006, *A&A*, 459, 745
- Fontanot, F., De Lucia, G., Monaco, P., Somerville, R. S., Santini, P. 2009, *MNRAS* accepted [arXiv:0901.1130]
- Förster Schreiber, N. M., et al. 2006, *AJ*, 131, 1891
- Franx, M., et al. 2003, *ApJ*, 587, L79
- Franx, M., van Dokkum, P. G., Förster Schreiber, N. M., Wuyts, S., Labbé, I., Toft, S. 2008, *ApJ*, 688, 770
- Gawiser, E., et al. 2006, *ApJS*, 162, 1
- Gehrels, N. 1986, *ApJ*, 303, 336
- Giallongo, E., Salimbeni, S., Menci, N., Zamorani, G., Fontana, A., Dickinson, M., Cristiani, S., Pozzetti, L. 2005, *ApJ*, 622, 116
- Giavalisco, M., et al. 2004, *ApJ*, 600, L93
- Glazebrook, K., et al. 2004, *Nature*, 430, 181
- Grazian, A., et al. 2006, *A&A*, 449, 951
- Hauschildt, P. H., Allard, F., & Baron, E. 1999, *ApJ*, 512, 377
- Heidt, J., et al. 2003, *A&A*, 398, 49
- Hora, J. L., et al. 2004, *Proc. SPIE*, 5487, 77
- Ilbert, O., et al. 2006, *A&A*, 457, 841
- Iovino, A., et al. 2005, *A&A*, 442, 423
- Kauffmann, G., & Heahnel, M. 200, *MNRAS*, 311, 576
- Kendall, M. G., & Stuart, A. 1961, *The Advanced Theory of Statistics*, Vol. 2, Griffin & Griffin, London
- Kinney, A. L., Calzetti, D., Bohlin, R. C., McQuade, K., Storchi-Bergmann, T., & Schmitt, H. R. 1996, *ApJ*, 467, 38
- Kriek, M., et al. 2007, *ApJ*, 669, 776
- Kriek, M., et al. 2008, *ApJ*, 677, 219
- Kroupa, P. 2001, *MNRAS*, 322, 231
- Labbé, I., et al. 2003, *AJ*, 125, 1107
- Larson, R. B. 2005, *MNRAS*, 359, 211
- Lawrence, A., et al. 2007, *MNRAS*, 379, 1599
- Le Fèvre, O., et al. 2005, *A&A*, 439, 845
- Maraston, C. 2005, *MNRAS*, 362, 799
- Maraston, C., Daddi, E., Renzini, A., Cimatti, A., Dickinson, M., Papovich, C., Pasquali, A., & Pirzkal, N. 2006, *ApJ*, 652, 85 (Erratum: 2007, *ApJ*, 656, 1241)
- Marchesini, D., et al. 2007, *ApJ*, 656, 42
- Marchesini, D., & van Dokkum, P. 2007, *ApJ*, 663, L89
- Marigo, P., & Girardi, L. 2007, *A&A*, 469, 239
- Monaco, P., Fontanot, F., & Taffoni, G. 2007, *MNRAS*, 375, 1189
- Muzzin, A., et al. 2009, *ApJ*, submitted
- Papovich, C., Dickinson, M., Ferguson, H. C. 2001, *ApJ*, 559, 620
- Papovich, C., et al. 2006, *ApJ*, 640, 92
- Pérez-González, P. G., et al. 2008, *ApJ*, 675, 261
- Pozzetti, L., et al. 2007, *A&A*, 474, 443
- Prévot, M. L., Lequeux, J., Prévot, L., Maurice, E., Rocca-Volmerange, B. 1984, *A&A*, 132, 389
- Quadri, R., et al., 2007, *AJ*, 134, 1103
- Reach, W. T., et al. 2005, *PASP*, 117, 978
- Reddy, N. A., & Steidel, C. C. 2009, *ApJ*, 692, 778
- Rudnick, G., et al. 2003, *ApJ*, 599, 847
- Rudnick, G., et al. 2006, *ApJ*, 650, 624
- Salpeter, E. E. 1955, *ApJ*, 121, 161
- Sandage, A., Tammann, G. A., & Yahil, A. 1979, *ApJ*, 232, 352
- Scarlata, C., et al. 2007, *ApJS*, 172, 494
- Schechter, P. 1976, *ApJ*, 203, 297
- Schlegel, D. J., Finkbeiner, D. P., & Davis, M. 1998, *ApJ*, 500, 525
- Schmidt, M. 1968, *ApJ*, 151, 393
- Somerville, R. S., Hopkins, P. F., Cox, T. J., Robertson, B. E., Hernquist, L. 2008, *MNRAS*, 391, 481
- Somerville, R. S., & Primack, J. R. 1999, *MNRAS*, 310, 1087
- Somerville, R. S., Primack, J. R., & Faber, S. M. 2001, *MNRAS*, 320, 504
- Spergel, D. N., et al. 2007, *ApJS*, 170, 377
- Springel, V., White, S. D. M., Tormen, G., & Kauffmann, G. 2001, *MNRAS*, 328, 726
- Springel, V., et al. 2005, *Nature*, 435, 629
- Taylor, E. N., et al. 2008, *ApJ*, submitted
- Toft, S., et al. 2007, *ApJ*, 671, 285
- van Dokkum, P. G., et al. 2006, *ApJ*, 638, 59
- van Dokkum, P. G. 2008, *ApJ*, 674, 29
- van Dokkum, P. G., et al. 2009, *PASP*, 121, 2
- Vergani, D., et al. 2008, *A&A*, 487, 89
- Wang, J., De Lucia, G., Kitzbichler, M. G., White, S. D. M. 2008, *MNRAS*, 384, 1301
- Wilkins, S. M., Hopkins, A. M., Trentham, N., Tojeiro, R. 2008, *MNRAS*, in press
- Wuyts, S., et al. 2007, *ApJ*, 655, 51
- Wuyts, S., Labbé, I., Förster Schreiber, N. M., Franx, M., Rudnick, G., Brammer, G. B., & van Dokkum, P. G. 2008, *ApJ*, 682, 985
- Zucca, E., et al. 2006, *A&A*, 455, 879